Slurry Formulation for Gel-cast Titanium

by
Jacques Piek

Thesis presented in partial fulfilment of the requirements for the degree of Master of Engineering (Mechanical) in the Faculty of Engineering at Stellenbosch University

Supervisor: Prof. Deborah Blaine
Co-supervisor: Prof. Iakovos Sigalas

March 2020

The support of the DSI-NRF Centre of Excellence in Strong Materials (DSI-NRF CoE-SM) towards this research is hereby acknowledged. Opinions expressed and conclusions arrived at, are those of the author and are not necessarily to be attributed to the CoE-SM.

Declaration

By submitting this thesis electronically, I declare that the entirety of the work contained therein is my own, original work, that I am the sole author thereof (save to the extent explicitly otherwise stated), that reproduction and publication thereof by Stellenbosch University will not infringe any third party rights and that I have not previously in its entirety or in part submitted it for obtaining any qualification.

Date: March 2020

Abstract

In this study, commercially pure titanium (CPTi) parts were gel-cast. Gel-casting is a ceramic forming technology developed in the early 1990's. Titanium is popular in the aerospace and biomedical industries for its excellent corrosion resistance, high mechanical strength, high strength-to-weight ratio and excellent biocompatibility.

A novel process for titanium slurry gel-casting was developed, studying the sedimentation behaviour of a methacrylamide (MAM)/methylene bisacrylamide (MBAM) and an Isobam® polymer binder system, respectively. Factors influencing the sedimentation behaviour of titanium particles in a binder are the monomer content, monomer:cross-linker ratio, dispersant content, slurry mixing time and solid loading of the slurry. An optimum slurry was developed with 20 wt% monomers, at a 6:1 MAM:MBAM ratio, with dispersant content of 0.8 wt% ammonium hydroxide (NH_4OH). CPTi powder with a particles size distribution of 15-45 μm was used at a solid loading of 55 vol%. Stokes Law was used to successfully suspend the powder particles in the cast slurry to obtain an evenly dense microstructure.

The slurry was cast into a resin 3D printed rectangular bar-shape mould, polymerized at 60 ˚C for 2 hours and dried in air at room temperature for 12 hours. Thermal gravimetric analysis (TGA) was conducted on the dried samples to determine the temperatures where the various binder constituents debind. Binder burnout was achieved by heating the dried parts to 400 ˚C at 1 ˚C/min and holding for 30 min, before presintering the parts at 650 ˚C for 30 min to obtain handling strength. The parts were vacuum sintered at 1200 ˚C for 2 hours at a heating rate of 10 ˚C/min. The shrinkage measured from cast to sinter, was 10.4 % and 9.03 % in the length and width of the rectangular bars, respectively.

Optical microscopy was used to study the sintered microstructure of the gel-cast parts, finding an evenly dense microstructure. Scanning electron microscopy (SEM) was used to study the fracture surfaces of the tensile test specimens, confirming that only intermediate sintering has taken place. Energy dispersive spectroscopy (EDS) was used to determine the elemental composition of the sintered microstructure, observing that carbon and oxygen contamination has taken place. Finally, the mechanical properties were evaluated: a yield- and ultimate tensile strength of 323 MPa and 378 MPa, respectively, and a hardness value of 60 HRBW, which is 86 % of wrought.

Uittreksel

In hierdie studie is kommersiële suiwer titaan parte geproduseer deur jelgieting. Jelgieting is ‘n produseringstegniek vir keramiek wat in die vroeë 1990’s ontwikkel was. Titaan is gewild in die lugvaart- en biomedese bedryf vir die sy uitstekende weerstand teen korrosie, hoë meganiese sterkte, hoë sterkte-tot-gewig verhouding en uitmuntende verenigbaarheid met menslike been as biomateriaal.

‘n Nuwe proses vir titaanmengsel jelgieting was ontwikke deur die sedimentasie gedrag van ‘n meta-akrielamied (MAM)/metileen-bisakrielamied (MBAM) en ‘n Isobam® polimeer bindmiddel te bestudeer. Faktore wat die sedimentasie gedrag van die titaanpartikels in the bindmiddel beïnvloed is die monomeer inhoud, monomeer:kruis-verbinder verhouding, dispergeermiddel inhoud, die titaanmengsel mengtyd en die soliede belading van die mengsel. ‘n Optimum mengsel was ontwikkel met 20 wt% monomere, teen ‘n 6:1 MAM:MBAM verhouding, met dispergeermiddel inhoud van 0.8 wt% ammoniumhidroksied (NH_4OH). Titaan poeier met ‘n deeltjiegrootteverspreiding van 15-45 µm was gebruik teen ‘n soliede belading van 55 vol%. Stoke se Wet was gebruik om die poeier partikels suksesvol in suspensie te hou in die gegiete mengsel om ‘n mikrostruktuur met eweredige digtheid te verkry.

Die mengsel was gegiet in ‘n reghoekige staafvormige gietvorm wat drie-dimensioneel gedruk is van harsmateriaal, gepolimeriseerd teen 60 ˚C vir 2 ure en gedroog in lug teen kamertemperatuur vir 12 ure. Termiese gravimetriese analise (TGA) was uitgevoer op die gedroogde jelgegiete monsters om die temperature waarteen die verskillende komponente van die bindmiddel uitbrand, te bepaal. Die uitbranding van die bindingsmiddel was bereik deur die gedroogte stafies te verhit tot 400 ˚C teen 1 ˚C/min en dit daar te hou vir 30 min. Die stafies was dan verder verhit tot 650 ˚C vir 30 min om hanteringskrag te verkry deur oorspronklike sintering. Die stafies was gesinter in ‘n vakuum teen 1200 ˚C vir 2 ure teen ‘n verhittingstempo van 10 ˚C/min. Van giet tot sinter was ‘n inkrimping van 10.4 % en 9.03 % in die lengte en breedte van die stafies, onderskeidelik, gemeet.

Optiese ligmikroskopie was gebruik om die gesinterde mikrostruktuur van die jelgegiete stafies te bestudeer. ‘n Eweredige digtheid in die mikrostruktuur was waargeneem. Skanderings-elektron-mikroskopie (SEM) was gebruik om die fraktuur oppervlaktes van die trektoets spesimens te bestudeer, bevestigend dat slegs intermediêre sintering plaasgevind het. Energie-verstrooings-spektroskopie (EVS) was gebruik om die elementele komposisie van die gesintreerde mikrostruktuur te bepaal. Hierdeur was waargeneem dat koolstof en suurstof kontaminasie plaasgevind het. Ten slotte was die meganiese eienskappe geevalueer: ‘n swig- en trekkrag van 323 MPa en 378 MPa, onderskeidelik, en ‘n hardheidswaarde van 60 HRBW, wat 86 % van gesmede eienskappe is.

Acknowledgements

The completion of this project was not without tremendous support and I would like to acknowledge the following people for their contribution:

My supervisor, Prof. D.C. Blaine, for her support and most valuable guidance.

My co-supervisor, Prof. I. Sigalas, for his initiative with the project and help with funding.

My parents, for their sacrifices for me to have had this opportunity and for their love, support and encouragement.

My sweetheart, Leandré, for her tremendous support and love, and for being patient with me through this project.

The DSI-NRF Centre of Excellence in Strong Materials for funding this project.

All honour to my Lord and Saviour, Jesus Christ. "*In him we live and move and have our being"* (Acts 17:28)

Soli Deo Gloria

Table of contents

List of figures

Page

List of tables

Page

List of abbreviations

AC	Activated carbon
AM	Additive manufacturing
APS	Ammonium persulfate
ASTM	American Society for Testing and Materials
BE	Blended elemental
BJT	Binder jetting
CAD	Computer Aided Design
CAF	Central Analytical Facility
CPTi	Commercially pure titanium
CSIR	Centre for Scientific and Industrial Research
DC	Dimensional change
DLMS	Direct laser metal sintering
EBM	Electron beam melting
EDS	Energy dispersive spectroscopy
EIGA	Electrode inert gas atomization
HDH	Hydrogenation dehydrogenation
HIP	Hot isostatic pressing
ITA	International Titanium Association
LPBF	Laser powder bed fusion
MIM	Metal injection moulding
PIM	Powder injection moulding
PM	Powder metallurgy
PSD	Particle size distribution
RPD	Rapid plasma deposition
RI	Refractive Index
SANS	South African National Standard
SEM	Scanning electron microscopy
SLM	Selective laser melting
TGA	Thermal gravimetric analysis

UTS	Ultimate tensile strength
VAR	Vacuum arc re-melting
YS	Yield strength
YSZ	Yttria stabilized zirconia

List of Symbols

ρ	Density, g/cm^3
m	Mass, g
V	Volume, cm^3
W	Weight fraction, -
φ	Solid loading, vol%
Y	Isotropic shrinkage, %
ΔL	Change in length, mm
L_0	Original length, mm
D_s	Sintered density, g/cm^3
S	Sedimentation rate, S
μ	Viscosity, Pa.s
g	Gravitational constant, m/s^2
ψ	Densification, -

1 Introduction

The subject of this study is the development of the gel-casting procedure for commercially pure titanium. In this section, the background and motivation for this study is presented, followed by the research objectives, limitation and scope of the study and the chapter outline for this dissertation.

1.1 Background and Motivation

The need for complex near-net-shape titanium parts is becoming more prevalent, especially in the biomedical industry where individually customized implants and bone replacements are required. This need requires the development of near-net-shape manufacturing methods. Powder metallurgy (PM) has been successfully used to produce near-net-shape titanium parts and has the advantage of controlling material porosity which contributes to implant fixation by bone ingrowth into the porous structure (Bottino et al., 2009; Li et al., 2008). PM processes that produce near-net-shape metal parts include press-and-sinter, hot isostatic pressing, powder injection moulding (PIM) and additive manufacturing (AM) technologies (Froes, 2012; Froes et al., 2004; Qian and Sam Froes, 2015). While the number of presentations on AM, mostly by Laser Powder Bed Fusion (LPBF), at the fifth biennial conference on the Powder Metallurgy and Additive Manufacturing of Titanium (PMTi2019) was high, indicating a large interest in this field, more mature technologies, such as metal injection moulding (MIM), remain more competitive at present (Ebel, 2019). The opportunity for novel PM technology research is seen in the 'MIM-like' AM technology, Binder Jetting (BJT), that is being developed into a production technology with complete production systems, including an AM machine, debinding unit and sintering furnace (Ebel, 2019).

At the PMTi2019, Praxis Technology, USA, presented on the ongoing development of a black titanium alloy suitable for MIM processing. A strong motivation for the use of black titanium is its significantly higher wear resistance, compared to Ti-6Al-4V, thus ideally suitable as biomaterial in knee- and hip replacement applications. The current limitations of black titanium are high costs, low strength and the potential for poor properties when PM processed, heat treated, then blackened (Ebel, 2019).

AM technologies, such as selective laser melting (SLM), are currently widely researched for their ability to produce customized complex porous implants (Taniguchi et al., 2016). Other benefits of AM include optimization of material use, which reduces weight while maintaining structural stability and thus allows a high degree of design freedom. Unfortunately, AM is limited by the build envelope (the size of the required part) and high production cost due to costly equipment.

Other challenges of AM currently identified in this research field include reproducibility, distortion, porosity and process control (Ebel, 2019).

Considering these limitations, there is need to consider alternative manufacturing processes, that still incorporate the net-shape and material utilization benefits of AM. To this purpose, in this study, gel-casting of titanium powder was evaluated as an alternative net-shape, powder-base manufacturing process. Gel-casting of ceramics is a well-defined near-net-shape powder-base manufacturing process, developed by the Oak Ridge National Laboratory in the early 1990's (Omatete et al., 1997). It involves mixing ceramic powder with a water-based gel binder to form a slurry that can be cast. The slurry forms a green part once the binder goes through a gelation reaction. The green part can then be sintered to form a coherent ceramic part. However, to date, gel-casting has only been commercially employed for ceramics and gel-casting using metal powders is an active research field. Preceding research undertaken by the author investigated the feasibility of gel-casting titanium as an undergraduate research project (Piek, 2017). The outcome of that study was that the slurry formulation and gel-casting process used for ceramic powders does not work well for titanium powder and additional development of the process is required. Erasmus (2018) and Riekert (2019) also contributed to this research by investigating whether vibration of the slurry during casting improved the quality of the final material.

Metal powder gel-casting is a novel approach and still in the research phase, where this dissertation forms part of that research. Nevertheless, gel-casting holds the potential for creating cost-effective complex near-net-shape titanium parts such as may be employed for biomedical implants.

1.2 Research Objectives

The aim of this research is to design a mould for gel-casting a titanium powder slurry that will render a net-shape sintered product with dimensional accuracy of 0.3 mm and mechanical properties at least 90 % of wrought. These parameters are similar to design criteria for metal injection moulding (Black and Kohser, 2008).

Therefore, the objectives of this research are:

i. Evaluating and developing the slurry formulation and mixing process to achieve the highest solids loading with a low enough viscosity, suitable for casting.
ii. Evaluating the microstructure and mechanical properties of the final sintered titanium part produced from the improved slurry formulation and gel-casting process.
iii. Reverse engineer the design procedure by shrinkage characterization of simple shapes, considering dimensional changes during the gel-casting process.

1.3 Scope and Limitations

This research project, which Mr J Piek conducted as part of his masters studies in the Mechanical and Mechatronic Engineering Department at the University of Stellenbosch, originates from a proposal by Prof DC Blaine and forms part of a bigger study regarding the mechanical behaviour of gel-cast products in collaboration with NRF Centre of Excellence for Strong Materials at the University of the Witwatersrand. The project is funded by the NRF Centre of Excellence for Strong Materials.

The specific aspect of the project that is undertaken by the University of Stellenbosch involves developing the slurry formulation and gel-casting process for commercially pure titanium powder only. Reverse engineering the design procedure through shrinkage characterization as well as evaluating the mechanical properties of the final sintered gel-cast part is limited to the gel-casting slurry and process developed for titanium in this project.

1.4 Thesis Outline

Chapter 2 presents the literature study conducted in titanium processing, titanium powder production, the gel-casting process and material characterization techniques.

Chapter 3 presents the design of experiments and procedures followed in order to achieve the objectives of this study.

Chapter 4 presents the results of the experiments as described in chapter 3, and a discussion of the findings from these results.

Chapter 6 presents the conclusions drawn from this study and recommendations for future work.

2 Literature Review

The literature study conducted for this research project is presented in this section. Firstly, motivation for this study, as supported by published literature, is presented in the overview. Thereafter, a review of literature relating to general titanium manufacturing processes, powder slurries, the gel-casting process, and material characterization techniques follows.

2.1 Overview

Complex near-net-shape parts are becoming more prevalent, especially in the biomedical industry where customised shapes are required for implants and bone replacement. The total number of hip replacement surgeries are expected to increase by 137 % (from 208 600 to 572 000) and knee replacement surgeries by 607 % (from 450 000 to 3.48 million) between 2005 and 2030 in the United States of America (Kurtz et al., 2007).

Ti-6Al-4V, a titanium alloy originally used in the aerospace industry, has been used as biomaterial since the 1950's (Semlitsch et al., 1992). Titanium alloys have been preferred over other standard orthopaedic materials, including stainless steels and cobalt-based alloys, because of their lower elastic modulus (Long and Rack, 1998). Titanium alloys are also preferred to the other metallic biomaterials, because of their excellent corrosion resistance, high mechanical strength, high strength to weight ratio, fatigue strength, formability, machinability and excellent biocompatibility due to the passive oxide surface layer that forms spontaneously (Cui et al., 2011; Long and Rack, 1998). In the early 1990's, new titanium alloy compositions were developed specifically for biomedical applications as a response to concerns about the cytotoxicity of vanadium (Long and Rack, 1998), such as Ti-6Al-7Nb (Semlitsch et al., 1992). Since then, the biocompatibility of titanium alloys has improved, focussing on lower elastic modulus alloys closer to the modulus of human bone (10-30 GPa). Ti-27Nb-13Zr produced by powder metallurgy is an example of such an alloy with elastic modulus in the range of 60-70 GPa (Mendes et al., 2016).

One of the most common applications for titanium and its alloys in the biomedical industry is artificial hip joints that consist of an articulating bearing (femoral head and cup) and stem as shown in Figure 1 (Cui et al., 2011). Costly additive manufacturing (AM) techniques, such as direct laser metal sintering (DLMS), use titanium powders to directly produce complex net-shape implants of customised shapes. AM can be used to create parts that are porous, with a structure close to that of human bone (Taniguchi et al., 2016; Traini et al., 2008).

With a yield strength for pure titanium of about 210 MPa, that can be significantly increased by alloying and heat treatment, and good mechanical property retention up to temperatures of 535 ˚C, titanium is often used as a high-temperature

engineering material (Black and Kohser, 2008). These qualities make titanium a popular material in various other industries, including the aerospace and military environment.

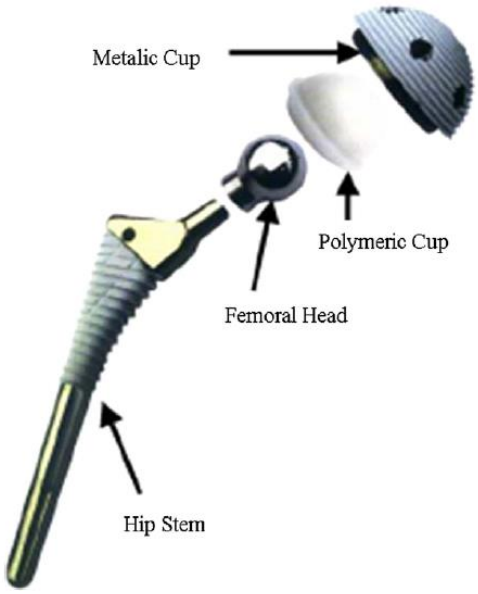

Figure 1: Schematic diagram of artificial hip joint (Cui et al., 2011)**.**

In the aerospace industry titanium alloys are employed in airframes and gas turbine engine components of aircraft to produce parts such as fan- and compressor blades, fan- and compressor disks, the fuselage, fasteners and landing gear by various manufacturing processes including AM (Cui et al., 2011). Boeing released their commercial market outlook in June 2019, forecasting the market for commercial aircraft over the next 20 years ("Boeing Company - Boeing Forecasts $8.7 Trillion Aerospace and Defense Market through 2028," n.d.). According to the report, growing passenger volumes and increasing airplane retirements will drive the need for over 44 000 new jets, valued at $6.8 trillion through 2038. Forecasters plan that just over 40 % would go to replacing aging airplanes while the rest will accommodate traffic growth. Taking the planes that will remain in service into account, the projected global fleet reaches 50 000 for the first time.

The advantages of AM manufacturing, relevant to the biomedical and aerospace industries, include creating highly complex structures, minimal material waste and a high degree of design freedom. However, the process is expensive due to costly equipment and costly powder production processes. Gel-casting, as an alternative manufacturing process to AM, holds the potential to produce titanium parts with similar advantages as AM, but more cost-efficiently. This potential is demonstrated in a study by Yang et al., presenting gel-casting as a technique for preparing porous titanium alloy implants (Yang et al., 2011). Considering that gel-casting has only been commercially employed for ceramics, gel-casting of metal powders is still a novel approach, and in the research and development phase.

2.2 Manufacturing Processes for Titanium Parts

Due to titanium's high melting point and high chemical reactivity, mainstream casting process, such as die- or permanent mould casting, are not suitable for this metal or its alloys (Black and Kohser, 2008). Complex-shaped products of high melting point metals are generally fabricated by more costly processes, such as forming processes, machining, investment casting and powder metallurgy (Black and Kohser, 2008).

These processes involve material removal from the starting metal stock so that what remains is the final desired part. The three principal machining processes are drilling, milling and turning wherein a sharp cutting tool is used to mechanically cut material away to form the part (Groover, 2013). A finished aerospace wing spar may contain as little as 4 % of the original billet with 96 % being lost as material waste in the forging and subsequent machining operations (Black and Kohser, 2008).

In investment casting, the desired shape is formed from wax and then coated by the investment material to form a mould. The mould is then heated to remove the wax from the mould and molten metal poured into the mould to produce the desired product. Investment casting has been used in ancient China and Egypt, but recently it has been used in the dental and jewellery industries (Black and Kohser, 2008). In a study of Atwood et al. (2007), the modelling of a titanium crown is investigated for dental investment casting. Investment casting greatly reduces or even eliminate the need for machining, but it is rather expensive compared to other casting methods.

PM processes offer great methods for producing complex near-net-shape metal parts. Common powder metallurgy (PM) processes for titanium parts include press-and-sinter of blended elemental (BE) powders, hot isostatic pressing (HIP) of prealloyed (PA) powders, powder injection moulding (PIM) and AM technologies (Froes, 2012; Froes et al., 2004; Qian and Sam Froes, 2015). In conventional press-and-sinter, BE powders are compacted under high pressure into the desired shape and then sintered to increase strength and hardness (Groover, 2013). Using hydrogenated titanium powder rather than normal fines has led to a significant improvement in BE material, resulting in an increase in the as-sintered density (Froes et al., 2004). Figure 2 shows complex parts that has been produced via BE press-and-sinter.

HIP for titanium parts, using a metal can, was developed in the 1970's by companies such as Crucible Research in the USA or Tecphy in France, which had produced parts for jet and rocket engines (Qian and Sam Froes, 2015). The process has been further developed between 1992 and 2000 by the Laboratory of New Technologies (LNT) on the basis of computer modelling of the HIP process for complex near-net-shapes. This enhanced process has been used by Synertech PM to produce a variety of titanium parts for gas compressors, rocket engines and airframes

("Synertech - Powder metal parts manufacturer," n.d.). The benefits of the HIP process is that it can produce larger complex near-net-shape parts with HIP furnaces of larger sizes than other PM technologies, while saving cost, using relatively low cost materials, avoids costly melt processes and results in relatively low material loss during processing (Froes, 2013).

Figure 2: Ti-6Al-4V parts produced via BE press-and-sinter and titanium hydride: (1) connecting rod, (2) saddles of inlet and exhaust valves, (3) plate of valve spring, (4) driving pulley of distributing shaft, (5) roller of strap tension gear, (6) screw nut, (7) embedding filter, fuel pump, and (8) embedding filter (Froes et al., 2004)**.**

PIM is another PM process developed to produce small, complex net-shape parts from high melting point metals. It is a process that combines the shape-forming capability of plastics, the precision of die casting and the materials flexibility of PM (Black and Kohser, 2008). The PIM process is similar to that of gel-casting in that the fine spherical-shaped metal powder is mixed with a flowable medium, the feedstock binder, which is then used to create a near-net shape part from the powder-binder mixture. In the case of PIM, the powder is typically mixed with a molten thermoplastic polymer-wax binder in order to form the powder feedstock. The powder-binder feedstock is produced in the form of pallets or granules, which is fed via a hopper into a heated injection moulding machine, similar to the plastic injection moulding process. PIM is a popular method for producing biomedical implants. One of the leading companies in PIM, Praxis Technology, has developed the only biomedical qualified Ti PIM process in the world, manufacturing over 250 000 implants up to date ("Praxis Technology Inc," n.d.). Recent advances in PIM include the use of Niobium (Nb), as β-stabilizing biocompatible material, alloyed with Ti to produce material with lower elastic modulus, closer to that of human bone (Zhao et al., 2013). Figure 3 shows an example of a PIM produced orthopaedic implant with porous ingrowth features.

Figure 3: Ti-6Al-4V orthopaedic implant with porous ingrowth features (Piemme, 2018)**.**

Finally, the current most popular manufacturing process for producing complex near-net-shape metal parts is AM, where parts are being built up layer-by-layer. Direct laser metal sintering (DLMS) and electron beam melting (EBM) is widely researched for creating porous titanium alloys with enhanced biocompatibility (Harrysson et al., 2008; Ivanov et al., 2018; Taniguchi et al., 2016; Traini et al., 2008). The big advantage of AM is its ability to produce customized complex parts, but it is still an expensive fabrication method due to costly equipment and processes, often requiring additional machining, and slow process times. At the 34th ITA (International Titanium Association) General Meeting held in October 2018, Norsk Titanium received the 2018 Titanium Application Development Award. This Norwegian company started delivering structural AM aerospace parts to Boeing in 2017. Figure 4 shows an example of a final commercial aerostructure titanium part manufactured by Norsk Titanium. They use a wire-fed process, Rapid Plasma Deposition (RPD), that produces parts weighing over 45 kg, 50 to100 times faster than powder-based AM and that uses 25 to 50 percent less material than forging ("Titanium USA 2018," 2018). It was also reported at the 2018 ITA General Meeting that the aerospace industry would account for 30 percent of the metal AM market over the next decade, focussing on the production of complex parts.

Figure 4: Completed commercial aerostructure titanium part next to its near-net RPD™ form ("Norsk Titanium | Media," n.d.)**.**

2.2.1 Titanium Powder Production

The characteristics of the powder used in PM has a great influence on the properties of the final PM produced part. Different powder production processes result in powders with different characteristics, such as size and shape (spherical or irregular) (German, 2005). The following fabrication processes are two of the most common used to produce commercially pure titanium (CPTi) powder: hydrogenation-dehydrogenation (HDH) and gas atomization. A unique titanium powder production process is plasma atomization. As the powder used in this study was sourced from the patent holders for this process, AP&C, a description of this process is also included. HDH titanium sponge fines and plasma atomized powders are readily available commercially at companies like Reading Alloys® and AP&C® respectively. HDH titanium sponge powder costs $44 - $66 per kg while plasma atomized titanium powder costs $215 per kg ("GE Additive Powders | GE Additive," n.d., "Titanium Powders | CP Ti and Ti 6A/4V | Reading Alloys," n.d.). While HDH sponge fines are typically less expensive than plasma atomized powders, plasma atomized powder is more suitable for gel-casting due to its sphericity.

The cost of titanium powder is directly related to the cost of titanium metal production and the energy and labour intensity of post-processing. The development of electrochemical and *in-situ* electrolysis, currently researched, may be promising as more cost-efficient production processes than commercialised thermo-chemical processes such as Kroll and Hunter (Mutombo, 2018). The Kroll process, invented in the 1940's, reduces titanium tetrachloride with magnesium to produce titanium sponge. Its post-processing steps including multiple re-melting and product fabrications make it a labour and energy intensive process. Upgrading ilmenite (40-65 % of $FeO.TiO_2$) to synthetic rutile is becoming important in the production of titanium metal due to the depletion of rutile (95 % of TiO_2). According to Mutombo (2018), electrochemical processes such as direct hydrometallurgical lixiviation is advantageous in processing abundant ilmenite ores, since low energy consumption is expected, and sufficiently high quality of synthetic rutile is produced. The Department of Science and Technology through the Titanium Centre of Competence (TiCoC), are currently underway to develop complementary technologies to help South Africa add value to its titanium ores (Machio et al., n.d.). South Africa has the world's fourth largest deposits of ilmenite and rutile after Australia, China and India.

2.2.1.1 Hydrogenation-dehydrogenation (HDH) Process

The hydrogenation-dehydrogenation (HDH) process starts with titanium in the form of metal scrap or titanium sponge. The titanium is subjected to a hydrogenation process where hydrogen atoms diffuse into interstitial sites in the titanium crystal structure, at elevated temperatures between 350 ˚C and 700 ˚C (Neikov et al., 2009). The hydrogen reacts with the titanium to form titanium hydride (TiH_2) which promotes the embrittlement of the metal for the next process step: mechanical grinding. Mechanical grinding, such as ball milling, jet milling and wet milling, is

typically used to produce milled powders with a large variation in particle size, depending on the technique used. The brittle TiH_2 easily fractures during milling, creating TiH_2 powder. Thereafter, the TiH_2 powder is dehydrogenised (interstitial hydrogen is removed from the TiH_2) by heating it under a vacuum to 700-800 ˚C for 1-2 hours, finally producing a fine titanium powder (Neikov et al., 2009). An overview of the process is shown in Figure 5. Some advantages of the HDH process is that it is low-cost, good control of oxygen content in sintered samples and the hydrogen emitted from the hydrogenated powders might become a protective atmosphere during sintering (Mendes et al., 2016).

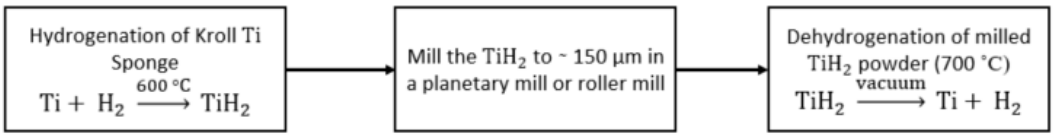

Figure 5: Flow diagram of HDH process for titanium powder production from sponge (adapted from Goso and Kale, 2010)

2.2.1.2 Plasma Atomization Process

Plasma atomization technology enables the production of fine spherical titanium powder from titanium wire. In this process, the metal wire feedstock is melted by the plasma torches. Atomization of the particles takes place in the cooling stage, in argon atmosphere, that rapidly solidifies the melt into highly spherical particles. A high purity product is ensured, and contamination is prevented by keeping the melting wire from coming into contact with any solid surface. Spherical titanium powder and Ti-6AL-4V alloy powder with particle size from 5 to 250 µm and oxygen content between 0.1 and 0.3 wt% are commercially produced by this process (Neikov et al., 2009). Plasma atomized powder has exceptional flowability and packing properties, which is critical in gel-casting and which make it popular for AM.

Current methods of producing AM Ti-based feedstock spherical powder originate with Ti-based feedstock bars/billets or wires, made by the ingot metallurgy technique of vacuum arc re-melting (VAR), adding significant cost to the powders. A study by the Council for Scientific and Industrial Research (CSIR) investigated the production of spherical Ti-based powders from PM produced bars/billets, which is cheaper than wrought bars/billets(Machio et al., n.d.). This study showed that the electrode inert gas atomization (EIGA) of PM bars/billets produced powder with similar characteristics to those from commercial bars/billets. In March 2019, a world leader in the design, development, manufacture and commercialization of advanced plasma processes and products, PyroGenesis Canada Inc., announced that they have developed a NexGen™ plasma atomization system that produces metal powder at over 25 kg/h (“Titanium Powder Produced with the NexGen™ Plasma Atomization System; Significant CAPEX and OPEX Reductions TSX Venture

Exchange:PYR," n.d.). This system results in large cost savings, opening the door to the use of plasma atomized powder for a wide range of applications.

2.3 Powder Slurries

Slurry casting is well-established and a primary manufacturing technique for ceramics, but not metals (Omatete et al., 1997). A chemical polymer gel consists of a covalently cross-linked network of polymers and is used in gel-casting to form powder slurries. A polymer gel is well defined by Rogovina as:

> *An elastic solid composed of at least two components, one of which (polymer) forms a physically or chemically bonded three-dimensional network that occurs in a medium of another component, a liquid, wherein the amount of the liquid is sufficient for ensuring the elastic properties of the gel (although it may be ten times or hundreds of times above that of the polymeric component)* (Rogovina et al., 2008).

The primary constituent of a gel-based binder is the monomer that connects the powder particles together, giving the green part structural strength. Additional binder constituents include the solvent, dispersant, defoamer, initiator and catalyst. It is important that the powder used to create the slurry remains dispersed within the gel-binder during casting in order to produce a green part with an even distribution of powder particles. The premix solution of the slurry is formed when the monomers, cross-linker and dispersant are dissolved in the solvent.

The zeta potential of a slurry, relates to the surface charge of the particles, and gives an indication whether a slurry has sufficient electrostatic repulsion to maintain dispersed (Particle Sciences, 2012). Zeta-potential measures the potential of a particle in an ionic solution at the boundary between the Stern layer and diffuse layer, as seen in Figure 6 (Cai et al., 2006). Larger positive values of zeta-potential at a fixed pH indicate a positively charged surface that attracts anions while lower values of zeta-potential at a fixed pH indicate a negatively charged surface that will attract cations.

Electrostatic repulsion of powder particles in a slurry is achieved by the particles absorbing the dissolved dispersant until it reaches a point of saturation. Up to the point of saturation, the powder particles in the slurry form a repulsive force, decreasing the viscosity. After saturation, the concentration of free ions would increase, leading to an increase in the viscosity (Duan et al., 2014).

It is important to consider the differences between metal- and ceramic powder surfaces for developing a well dispersed metal powder slurry. Metal surfaces have high values of density, reactivity, surface tension, polarizability, absorptivity and electrical conductivity (Nelson, 1988). High polarizability causes metal particles to attract one another to form strong agglomerates, but also to attract dispersants strongly. In metal slurries, density often plays a more significant role in the

dispersion of the particles than the surface charge of the particles (Ohkawa et al., 2004).

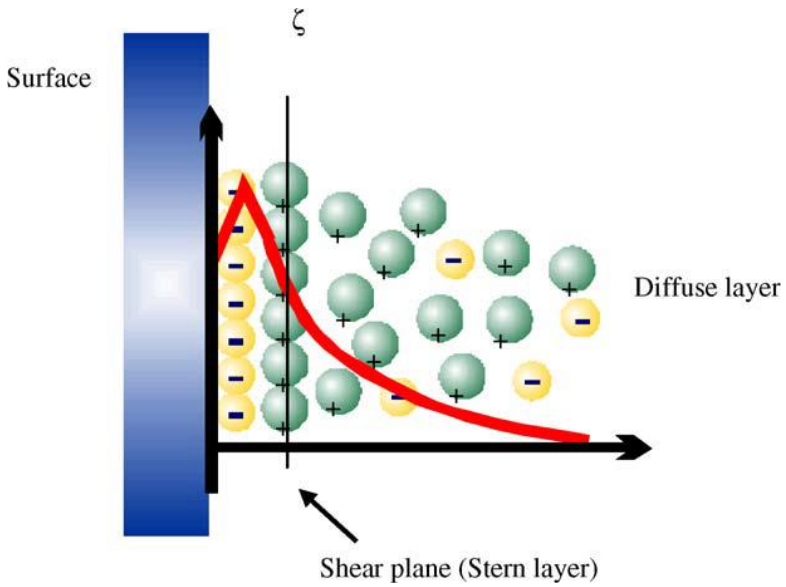

Figure 6: Schematic diagram of the electric double layer in zeta-potential measurement (Cai et al., 2006)

Studies have reported that the suitable viscosity of slurries for gel-casting is below 1 Pa s at a shear rate of 20 s-1 to ensure better filling of the mould without the use of outside force (Li et al., 2008; Yang et al., 2011). These viscosity characteristics are reported by the very few published studies on metallic gel-casting and were taken as design criteria for this study. There are a few factors that influences the viscosity of the slurry, including the solid loading, monomer content and dispersant content.

Li et al. (2008) reported that the viscosity of a 37 vol% Ti slurry decreases with the increase of ball milling time which was attributed to the disjoining of powder agglomerate by ball milling. In this study of gel-cast titanium implants, the effect of two different dispersants were investigated: ammonium citrate and NH_4OH (Li et al., 2008), where acrylamide was used as monomer. Li found that the viscosity of the titanium slurry was below 1 Pa s (between 0.9 and 0.85) for dispersant contents of 0.4, 0.6 and 0.8 wt% (based on the premixed solution) using NH_4OH as dispersant. The viscosity of the slurry stays greater than 1 Pa s using ammonium citrate as dispersant, at the same content amounts. It was concluded that NH_4OH favours the dispersion of Ti particles and ammonium citrate the dispersion of ceramic particles in an acrylamide-based monomer system.

Increasing the monomer content and a higher monomer:cross-linker ratio, increases the green strength of a part (Li et al., 2008; Pollinger et al., 2016). Furthermore, higher monomer content also improve the fluidity of a slurry, because of better

dispersion of the powder particles in a higher concentrated solution (Yang et al., 2011). An increase in solid loading on the other hand causes an increase in the viscosity as well as an increase in the final sintered density of the part (Duan et al., 2014).

2.4 Gel-casting

Gel-casting to date has only been successfully employed in a commercial environment for ceramics. Metal powder gel-casting is a novel approach and still in the research phase.

Gel-casting is a near net-shape process developed for ceramic fabrication in the early 1990's by Janney and Omatate of the Oak Ridge National laboratory based on the free-radical polymerization of acrylamide (Omatete et al., 1997). The original gel-casting system had capabilities for short forming time, high green strength, uniform powder packing densities and easy binder burnout (also called pyrolysis).

The gel-casting process is illustrated in Figure 7. Powder of the material required for the final product is mixed with a liquid binder system to form a slurry. The binder system contains various chemicals that allow even dispersion of the powder in the slurry, flowability of the slurry during the casting process and eventually forms a gel in which the powder particles are evenly suspended in the cast part and undergoes *in situ* polymerization (Omatete et al., 1997). After most of the solvent is removed by drying, the polymers in the gel remain, gluing the powder particles together in the gel-cast part, now called a green part. Thereafter the part is fired, during which the remaining binder polymers burn off and the powder particles sinter together into a solid part.

The advantage of gel-casting is the ability to produce complex near-net-shape parts, such as turbine wheels, with a high green strength using inexpensive moulds from metals, wax, glass and plastic (Omatete et al., 1997). The complexity of the gel-cast product is only limited by the ability to create the mould. Because of the high green strength of gel-cast parts, green machining is possible to create even more complex features.

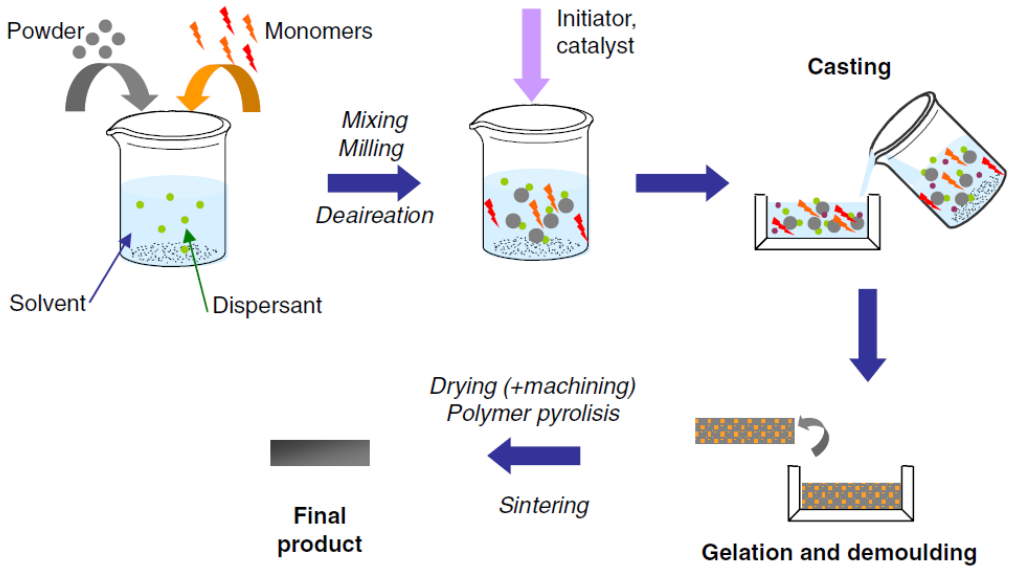

Figure 7: Steps involved in the gel-casting process (Tallon and Franks, 2011)

2.4.1 Suitability of PIM Binder Systems for Gel-casting

Powder injection moulding (PIM), like gel-casting, makes use of a binder system to create a polymeric structure for the powder particles to be dispersed in (German, 2003; Sidambe et al., 2012). This is called the feedstock that is then injection moulded under pressure. Because the slurry is injected with pressure, a more viscous slurry than for gel-casting is suitable (Sidambe et al., 2012).

In a study by Barreiros (2008), investigating the preparation of PIM feedstocks for bio-applications, an agar-based binder is used. The reported benefits of this aqueous-based binder system are environmental friendliness, low injection pressure needed, high green strength and good performance with a low binder content of 14 wt% and solids loading of 60 vol% (Barreiros et al., 2008). Wang (2009) and his colleagues used an agar-based binder in the casting of 316L stainless steel as an alternative to the toxic conventional polymers used in gel-casting, such as acrylamide. This agar-based binder system polymerizes during cooling, requires heating during the mixing process and is injection moulded under low pressure.

The problem with PIM binder systems applied to gel-casting, is that it requires heating to ensure suitable fluidity for moulding of the slurry and also make use of heat transfer for polymerization of the slurry. For the agar-based binder system mentioned, the feedstock is produced by mixing the mixture in a sigma blender and then shredding the mixture into pellets. The feedstock is then injection moulded around 85 ˚C, where the feedstock is relatively fluid, and an injection pressure in the range of 10 to 55 bar into a net-shape part (Barreiros et al., 2008; Labropoulos et al., 2002). The heating and pressure filling requirement for this system poses a problem for the gel-casting process, where casting of the mixture takes place

without it passing through a screw or nozzle that can heat the mixture to obtain suitable fluidity for casting.

2.4.2 Gel-casting Binder Systems

Titanium powder is very reactive. Thus, selection of gel systems is important in order to avoid contamination of the microstructure, which in turn degrades the mechanical properties.

The originally developed binder system for ceramics fabrication consisted of acrylamide (AM), a monofunctional monomer, methylene bisacrylamide (MBAM), a difunctional monomer cross-linker, and the free radical initiator, ammonium persulfate (APS) (Omatete et al., 1997). To break down the APS and speed up the cross-linking, tetramethylethylenediamine (TEMED) was typically used as catalyst.

Two factors limited the industrial use of AM as monomer in the gel-casting system: AM is a neurotoxin and it forms carbon-nitrogen bonds during polymerization which are difficult to break, requiring pyrolysis in air above 600 ˚C (Pollinger et al., 2016). The development of low-toxicity organic monomers was pursued investigating monomers such as methacrylamide (MAM) and 2-Hydoxyethyl methacrylate (HEMA) (Janney et al., 1998). In this study by Janney, MAM was shown to be an effective replacement of AM, also using MBAM as cross-linker, APS as initiator and TEMED as catalyst (1998). MAM has a polymeric structure of a single double bond and MBAM at least two double bonds. When polymerized together in a certain ratio, the initial linear polymer is strengthened. A silicon nitride turbine rotor (Figure 8) of around 18 cm in diameter has been successfully produced with the low-toxicity MAM binder system (Janney et al., 1998).

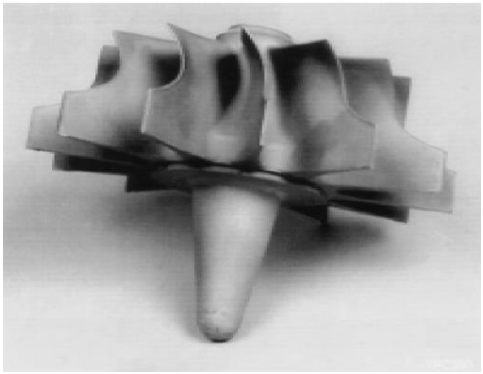

Figure 8: Silicon nitride turbine rotor manufactured using gel-casting with the MAM/MBAM system (Janney et al., 1998)

Recently, a non-toxic water-soluble copolymer of isobutylene and maleic anhydride (Isobam®) binder system was developed acting as both dispersant and gelling agent (Yang et al., 2013). The benefits of this binder system are its favourable rheological

properties, environmental friendliness and complete burnout at low temperatures (Jee et al., 2006).

2.4.3 Mould Design and Casting Process

The mould material and fabrication method are critical to manufacturing complex near-net-shape titanium gel-cast parts. The complexity of the gel-cast part is controlled by the ability to create a mould for the part. Moulds for gel-casting has been made from metals, glass, wax and plastics (Omatete et al., 1997).

Multiple-use moulds are usually used in die-casting and made from metals that can withstand wear (Black and Kohser, 2008). These moulds are often expensive to fabricate due to machining or other methods needed to create the complex geometries desired. Single-use moulds, from sand or wax, are usually used for higher-melting-temperature materials in processes such as sand casting or injection moulding (Black and Kohser, 2008). Single-use moulds are generally heated and burnt off to remove the cast part. Using wax moulds for gel-casting could cause warping and cracking of the cast part during mould burn off as it will influence the drying of the part.

Stereolithography (SLA), an AM technology, is the selective polymerization of an oligomer to fabricate controlled 3D structures layer-by-layer. SLA has the potential to fabricate cost-efficient complex near-net-shape moulds for gel-casting as compared to expensive metal moulds employed in die-casting. SLA moulds have proven some success by successfully manufacturing, using gel-casting, porous glass-ceramic tissue scaffolds with controlled internal architecture and dimensions (Chopra et al., 2012). In another study SLA has been used to fabricate complex moulds for gel-casting zirconia-based all-ceramic teeth (Liu et al., 2018). SLA is becoming popular in the gel-casting process for mould production because of its ability to create complex structures with a short manufacturing cycle at low cost. Other advantages of SLA include dimensional accuracy within 0.1 % of the 3D printed part, good surface finish and quick modification to the design of the part through 3D modelling software, resulting in more cost savings (Liu et al., 2018).

2.4.4 Binder Burnout and Pre-sintering

The binder's major role is in moulding; to keep the particles together. Binder burnout is an important step before sintering. Most of the binder, discussed in section 2.4.2, is removed before sintering to prevent distortion, cracking and contamination of the component.

The burn-off stage involves the combustion of any trapped air in the part and the removal of lubricant or binder. Polymer burnout occurs when the part undergoes heating through the temperature range where the polymer decomposes and evaporates. A low heating rate is required for this stage to prevent fracture of the part. A rapid heating rate will cause high internal pressure from air or binder entrapped in closed pores. Oxygen accelerates the burnout of polymers, but a

neutral atmosphere, like argon, requires that all decomposition products form from the polymer, which can cause sooting or carbon contamination (German, 2005). Thermal debinding of a binder under inert gas atmosphere is called pyrolysis. According to a study by German and Bose (1997), the key to rapid binder burnout is to use a multiple component binder system where a backbone polymer remains after initial component burnout to hold shape and provide strength. The backbone polymer is decomposed during pre-sintering. Parts containing an appreciable amount of binder, causes additional porosity in the shape upon removal. This feature is an advantage to gel-casting to prepare porous biomedical implants, contributing to the biocompatibility of the part (Li et al., 2008).

Saturation is described as the relative degree of pore space filled by a fluid from fully saturated pores (unity) to empty pores (zero). Partially saturated pores exhibit a pendular structure with a saturation below 0.2 (German and Bose, 1997). As binder is removed through the surface connected pores, a ring of binder exists at the point of contacts between particles and form pendular bonds. Figure 9 illustrates the states of the pores, from saturation to pendular, as binder is removed. The capillary attractive forces of these bonds provide part strength. Burnout or evaporation is the only way to remove binder in the pendular state.

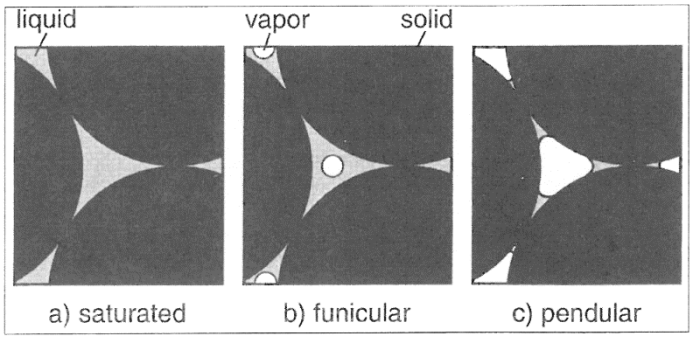

Figure 9: Structures for differing levels of pore saturation showing liquid (binder) and vapor location in pores between particles: a) saturated state, funicular state, and c) pendular state (German and Bose, 1997)**.**

In a study investigating the thermal decomposition behaviour of the Isobam® system, mentioned in section 2.4.2, complete mass loss was achieved at 400 ˚C (Jee et al., 2006). Complete pyrolysis for the MAM/MBAM system happens at temperatures above 600 ˚C, due to strong carbon-nitrogen bonds (Pollinger et al., 2016). Complete pyrolysis of silicon nitride parts prepared with the MAM/MBAM binder system were reported below 550 ˚C, while complete pyrolysis of the neat MAM/MBAM system in air is only reached at 620 ˚C (Janney et al., 1998). Figure 10 shows the Thermal Gravimetric Analysis (TGA) curves for silicon nitride samples in nitrogen and air, showing the mass loss as binder burns of at different events. Binder burnout in an inert atmosphere results in carbon contamination, because there is no oxygen for combustion of the decomposing polymer (Janney et al., 1998).

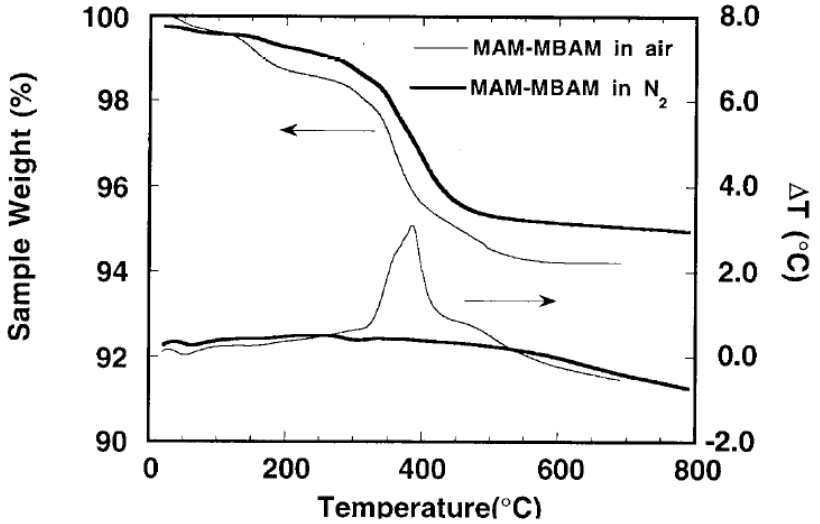

Figure 10: Pyrolysis of gelled MAM/MBAM silicon nitride samples in air and nitrogen (Janney et al., 1998)**.**

2.4.5 Sintering of Titanium Powder

Sintering is a conventional process that goes hand-in-hand with pressing. After powder has been compacted into a green part, the part lacks strength and hardness (Groover, 2013). Sintering is a heat treatment performed on the compacted green body, or in the case of gel-casting on the cast green body, to bond its metallic particles and thereby increasing its strength and hardness. Sintering causes a change in the mechanical properties of the part, as well as the microstructure. Black and Kohser (2008) explain that metallurgical bonds form between powder particles as a result of solid-state atomic diffusion, and strength, ductility, toughness, and electrical and thermal conductivities increase. Atomic diffusion usually takes place between 0.7 and 0.9 of the metal's melting point temperature, and therefore the term *solid-state sintering* is normally used to refer to this conventional process (Groover, 2013).

Before diffusion can take place, the green body needs to be preheated in order to burn of any lubricants of binders. This process is called debinding, or binder burnout, and will be covered in section 2.4.4. Diffusion is the mechanism by which mass transfer occurs to form necks between particles and transform them into grain boundaries. The driving force behind sintering is the reduction of surface energy.

Figure 11 illustrates the sintering stages on a microscopic level. The green part consists of many distinct particles. Each particle has several neighbouring particles, providing for multiple grain boundaries to form, with irregular and angular shaped pores between the particles. With prolonged time at a temperature close to, but below, the melting temperature of the material, grain growth takes place. Grain growth accelerates as full density is approached since there is less of a pore

hindrance to grain boundary motion (German, 2005). Shrinkage occurs during sintering as a result of pore size reduction due to grain growth.

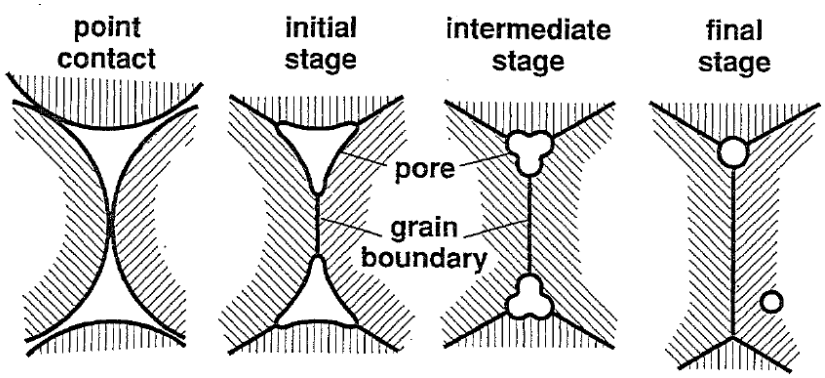

Figure 11: Schematic diagrams of the pore structure changes during sintering, starting with particles in point contact. The pore volume decreases, and the pores become smoother. As pore spheroidization occurs, the pores are replaced by grain boundaries (German, 1996)**.**

After keeping the part for a prolonged time at the sintering temperature, the part is cooled to room temperature again. It is critical for the sintering process to be conducted in a vacuum or inert gas atmosphere to prevent oxidation, which will significantly affect the mechanical properties and quality of the part. Vacuum sintering is frequently used for stainless steel, titanium and the refractory metals (Black and Kohser, 2008).

2.5 Material Characterization Techniques

2.5.1 Particle Size Distribution (PSD)

Particle size distribution (PSD) is determined by light scattering and can be tested according to the ASTM B822-10 or ISO 13320-1 standards (ASTM International, 2010). The ISO 13320-1 describes the general principles of laser diffraction methods for particle size analysis. A prepared sample of powder dispersed in water, or a suitable organic liquid, is circulated through the path of a light beam. The light beam is scattered by the particles, collected by photodetector arrays and converted to electrical signals that are then processed and analysed (Figure 12). The PSD information of supplied powder is also found on the information sheet of the supplied powder.

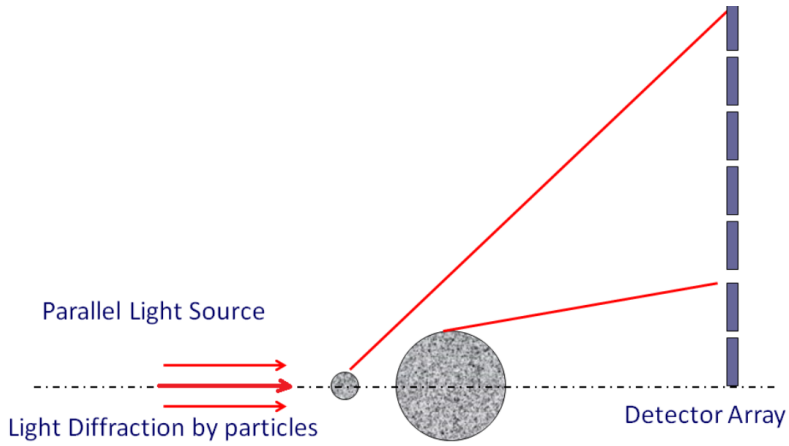

Figure 12: Light scattering principle used in PSD analysis (Delft, n.d.)

2.5.2 Optical microscopy

Optical microscopy is the primary material characterization technique to study the morphology (size, shape and structure) of a microstructure by forming an image of the surface of a specimen (Brandon and Kaplan, 2008). It is also useful to study the macrostructure of a sample. Depending on the nature of the sample, there are two forms of optical microscopy: reflected-light microscopy or transmitted-light microscopy. Reflected-light microscopy is used to study the microstructure of opaque samples, while transmission microscopy is used on transparent samples. Since titanium is a metal, and metallographic samples are opaque, reflection microscopy is relevant for this study.

The reflected-light microscope consists out of three main systems: the illumination system, the specimen stage and imaging system. Figure 13 illustrate the working principles of reflected-light microscopy. The condenser lens focusses a beam of light waves from the light source onto a small area of the specimen, condensing the area of interference on the objective lens, causing a higher resolution. Visible light (350 -700 nm) will determine the resolution limits (Fahlman, 2010). Incident parallel light waves is refracted through the objective lens to a focal point, forming a magnified image of the object.

Sample preparation include cutting, mounting, grinding and polishing, and chemical etching (Taylor and Weidmann, 2016). Grinding flattens the surface of the specimen and mechanical polishing removes the damage of the prior preparation stages. Etching selectively removes material from the surface to reveal certain surface features of the microstructure such as grain boundaries.

Optical microscopy it not widely used in the research field of gel-casting. Most research studies use scanning electron microscopy (SEM) for morphological analysis. However, it was found that optical microscopy is useful for studying pores in the microstructure of sintered specimens (Chang and Zhao, 2013).

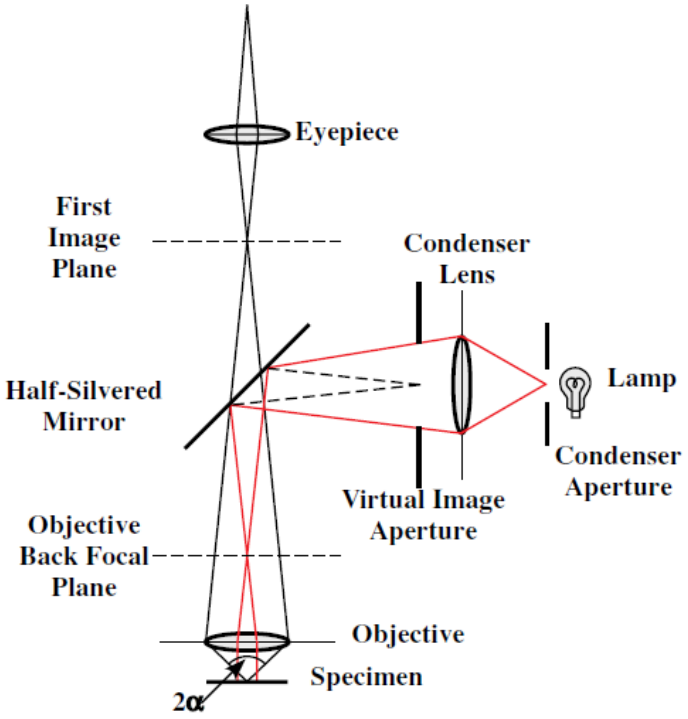

Figure 13: The principle components of a reflected-light microscope (Brandon and Kaplan, 2008)**.**

In the development of the gel-casting process of titanium alloys, optical microscopy will be useful to study external casting defects, internal porosity at different stages in the gel-casting process, morphology and microstructural analysis.

2.5.3 Scanning Electron Microscopy (SEM)

SEM makes use of an electron beam to scan the surface of a specimen and characterize its microstructure through different signals being generated from it, as seen in Figure 14. The information gathered from generated signals depend on the interaction of the incident beam with the sample. Topographical and atomic number information are obtained from backscattered electrons. Information on surface topography and surface films are obtained from secondary electrons. Microanalysis and distribution of elements are obtained through X-rays emitted by the sample, by a method called energy dispersive spectroscopy (EDS). (Smithells et al., 2004)

As seen in Figure 15, the main components of the scanning electron microscope consist of the electron gun system, lens system and detector. Electrons are generated and accelerated by the electron gun system. The lens system consists of electromagnets that are used as lenses to focus the electron beam on the sample and scan it. The detector collects the backscattered electron, secondary electron and X-ray signals generated from the incident beam on the specimen.

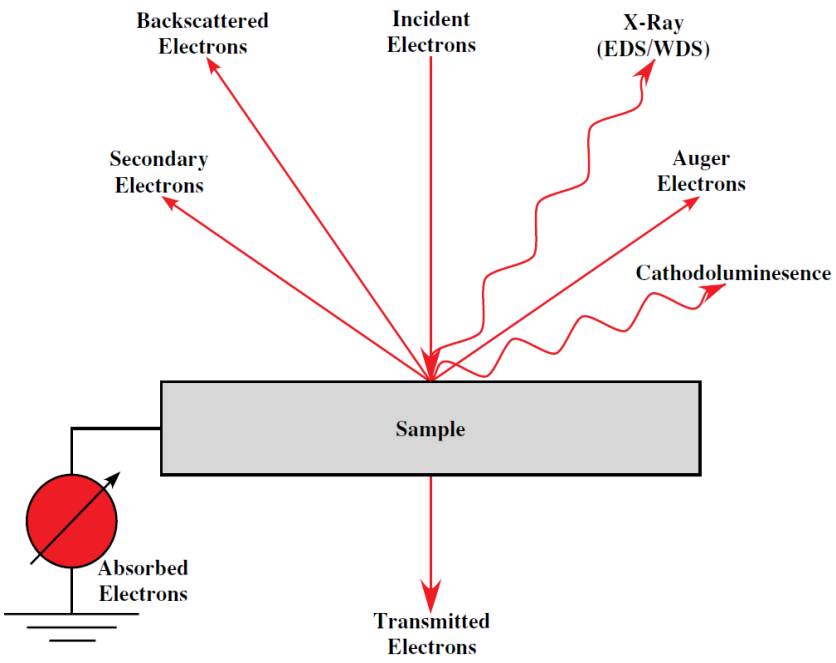

Figure 14: Signals generated from the incident scanning electron beam (Brandon and Kaplan, 2008)**.**

There are three types of electron guns as illustrated in Figure 15 (B). Beams of electrons are produced with energies typically in the range of less than 1 keV to more than 30 keV (Smithells et al., 2004). The thermionic emission (TE) gun generates electrons with energies in the range of eV by heating either a tungsten filament or a single crystal of lanthanum hexaboride (LaB6). A large emission current can be generated from the Schottky emission gun, using a single tungsten crystal coated with zirconium oxide (ZrO) as the cathode. The field emission gun produces a high electric field by using a single tungsten crystal, sharpened to a tip radius of about 100 nm. (Inagaki and Kang, 2016)

The three types of objective lenses, shown in Figure 15 (C), have a significant effect on the aberration and thus on the resolution of a SEM. The out-lens objective lens is a fixed distance from the specimen with high aberration and relatively low resolution in comparison to the snorkel objective lens. Because the magnetic field is generated below the snorkel objective lens, aberration is reduced, and resolution is improved. With the in-lens objective lens, the specimen is set in the lens, reducing the aberration, but limiting the specimen size to about 5 mm in diameter. (Inagaki and Kang, 2016)

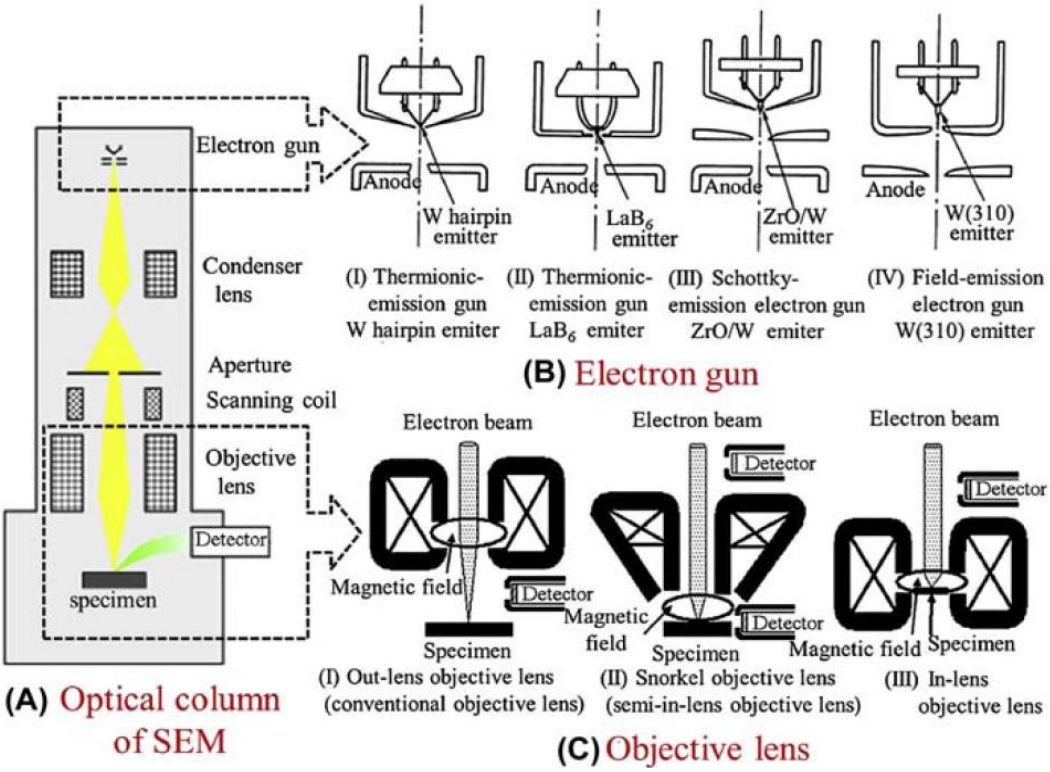

Figure 15: The principle components of SEM instrumentation (A) and types of electron guns (B) and objective lenses (C) (Inagaki and Kang, 2016)

During sample preparation for SEM, it is highly important to avoid electrostatic charging of the surface of the specimen. Electrostatic charging of the surface effects the resolution and image stability due to unstable secondary emission (Brandon and Kaplan, 2008). Non-conducting specimens should be coated with a thin layer of electrically conducting film.

Emitted X-rays comes from a volume element, defined by the envelope of electron energy that exceed the energy required to excite characteristic radiation of a chemical constituent (Brandon and Kaplan, 2008). L, M and K radiation (characteristic X-ray radiation) is excited when the energy of the incident electron beam exceeds that of the threshold energy for the characteristic radiation. The innermost shell (K shell) require a higher energy excitation to release characteristic X-rays. With an X-ray line-scan, the X-ray signal is recorded in the form of energy dispersive spectroscopy (EDS) spectrum at each point along the line of a selected region. The peaks at a point in the line scan are characteristics of a specific chemical constituent.

In a study where TiAl-based composites were prepared by gel-casting, SEM was used to study the morphology of the powders (Lu et al., 2015). SEM was also used to study the morphology of the samples at different stages through the gel-casting

process. EDS analysis, **Error! Reference source not found.**, shows residual carbon in the sample after decomposition of the monomer.

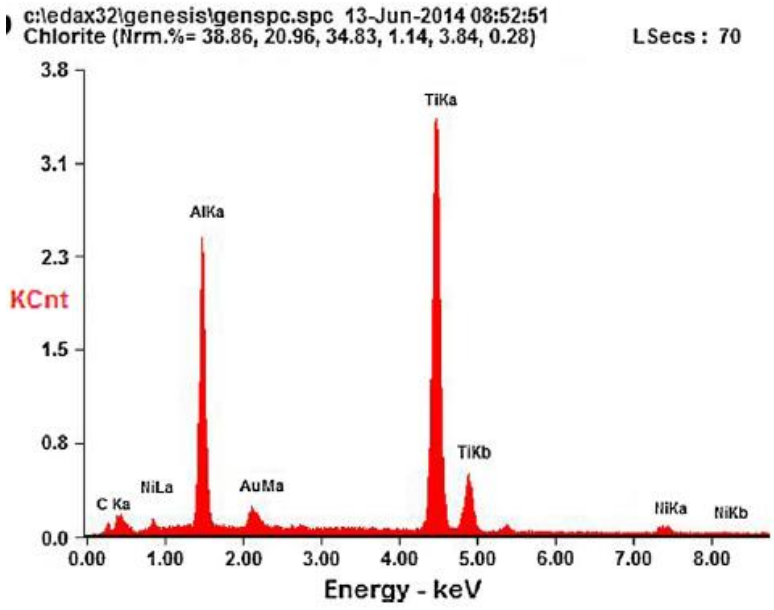

Figure 16: Energy dispersive spectrum analysis of debinded samples showing presence of carbon (Lu et al., 2015)**.**

SEM will be useful to study the morphology and microstructure of the Ti-alloy specimens through the gel-casting process. It is also beneficial for powder characterization. EDS can be used to determine chemical constituents in the samples after binder burnout and sintering to determine whether contamination of the part has taken place.

2.5.4 Mechanical testing

Various testing standards are useful for obtaining mechanical properties of a specimen. The SANS 6892-1:2010 standard is for tensile testing of metallic materials at room temperature. The test involves straining the test specimen by tensile force to fracture, for the determination of one or more of the mechanical properties mentioned in clause 3 of the standard. Mechanical properties such as tensile strength, proof strength, yield strength and modulus of elasticity can be obtained from this test. It is preferred that test pieces have a relationship between the original gauge length (L_0) and the original cross-sectional area (S_0) of the specimen governed by the equation:

$$L_0 = k\sqrt{S_0}\,, \qquad (2.5.1)$$

where k is a coefficient of proportionality with an internationally adopted value of 5.65. The gauge length is not to be less than 15 mm. Test pieces can also be

fabricated according to an equivalent standard for metallic tensile testing, like the ASTM E8M. Table 1 shows the tensile property requirements for grade 1 CPTi according to the standard specification for powder metallurgy (PM) titanium and titanium alloy structural components, ASTM B988.

Table 1: Tensile requirements for Grade 1 CPTi according to ASTM B988

Classification	Yield Strength (0.2 % offset), MPa	Tensile Strength, MPa	Elongation in 25 mm, %	Reduction in Area, %
Grade 1 PM100 [1]	138	240	24	30
Grade 1 PM90	124	216	22	27

The SANS 6508-1:2009 standard describes the test methods for obtaining the Rockwell Hardness (HR) of metallic materials. The Rockwell hardness is a measure of the depth (h) of an indentation made by an indenter of specific size, material and shape. Grade 1 commercially pure titanium powder is tested on the Rockwell B scale, with a hard metal ball indenter, and has a reported hardness of 70 HRBW ("ASM Material Data Sheet," n.d.).

2.5.5 Density and solid loading (powders, slurry, green, sintered)

In the gel-casting process it is important to take the following densities into account: apparent density of the powder, slurry density, green density and the sintered density.

The apparent density of a powder is an important property as it directly relates to the maximum solid loading of a slurry. Solid loading refers to the fraction of powder, by volume percent, of the total slurry. Apparent density is measured by permitting a volume of powder to flow into a container with definite volume under controlled conditions. The mass of the powder per unit volume is determined and reported as apparent density according to the ASTM B212-12 specification.

According to German and Bose, the slurry mixture density (ρ_{slurry}) is determined by a law of mixtures as (German and Bose, 1997):

$$\rho_{slurry} = \varphi\rho_P + (1-\varphi)\rho_B \,, \qquad (2.5.2)$$

[1] PM100 denotes equivalence to Specification ASTM B348 tensile properties, and PM90 90 % of B348 tensile properties.

where ρ_P is the theoretical density of the powder, ρ_B is the density of the binder and φ is the solid loading. The green density, calculated as the density of the slurry mixture, is the primary characteristic of the part prior to sintering and plays a major role in the shrinkage required of the part to reach full sintered density. The green density could be explained as the ratio of metal powder volume to the external volume of the cast.

The sintered density of powder metallurgy products can be determined using Archimedes Principle according to the standard test method ASTM B962 or by pycnometry. The sintered density gives an indication of the final gel-cast part porosity.

3 Experimental Procedure

This chapter presents the experimental procedures followed in this study. The purpose of the experimental study is to develop the gel-casting process for pure titanium and then to evaluate the mechanical properties of the sintered gel-cast part. An overview of the experimental plans is shown in Figure 17.

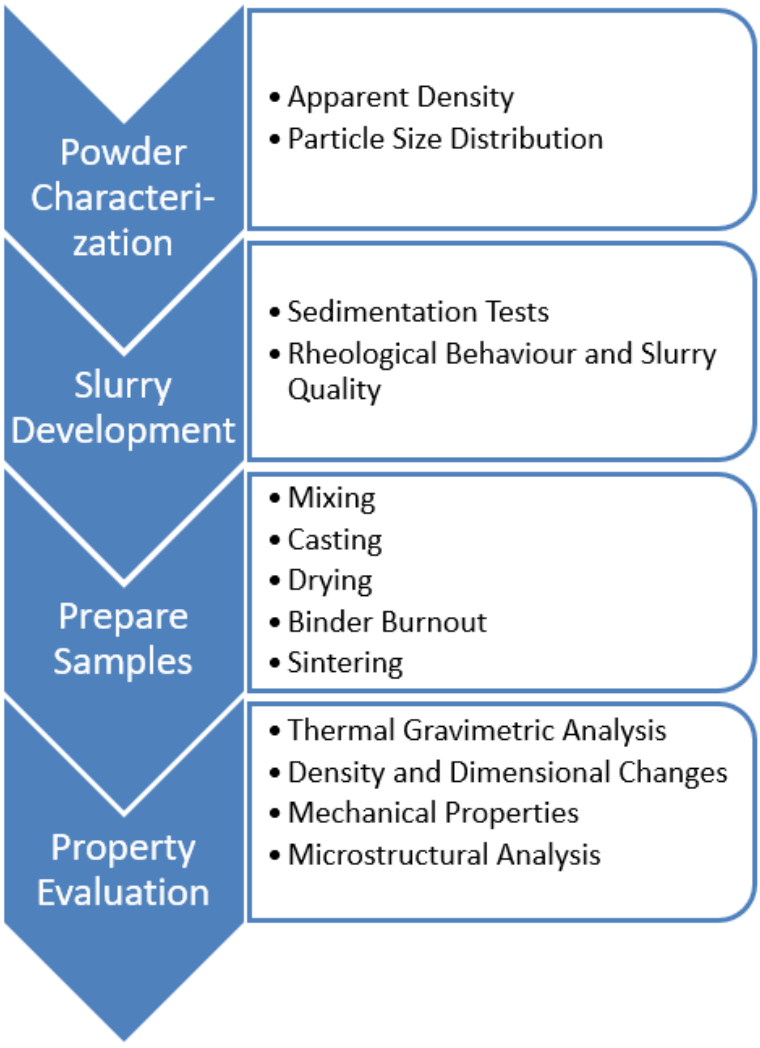

Figure 17: Experimental plan overview

3.1 Raw Materials

The raw materials selected for the production of the gel-cast titanium parts in this study are discussed here. The raw materials and their functions are listed in Table 2.

Table 2: Raw materials for titanium gel-slurry preparation

Item	Function	Material Name	Formula
1	Powder	Commercially Pure Titanium (CPTi)	-
2	Monomer	Methacrylamide (MAM)	C_4H_7NO
3	Cross-linker	N,N'-Methylenebisacrylamide (MBAM)	$C_7H_{10}N_2O_2$
4	Solvent	Deionized Water	H_2O
5	Dispersant	Ammonium hydroxide	NH_4OH
6	Initiator	Ammonium Persulfate (APS)	$H_8N_2O_8S_2$
7	Catalyst	N, N, N', N'-Tetramethylethylenediamine (TEMED)	$C_6H_{16}N_2$
8	Monomer	Isobam®	$(C_4H_2O_3.C_4H_8)x$

3.1.1 Commercially Pure Titanium Powder (CPTi)

The powder that was used in this study is spherical commercially pure titanium powder (CPTi), produced by Advanced Powders and Coatings® (AP&C®) according to the plasma atomization process. The powder complies with the ASTM B348 grade 1 standard, as reported on the material specification certificate, with a reported particle size of 15-45 µm. The material specification certificate is given in Appendix A.1.

3.1.2 Binder Material

The binder components are discussed in section 3.3.1. The binder materials were supplied by Sigma Aldrich®, except for the solvent, deionized water, that was supplied by Kimix Chemicals & Lab Supplies cc. The slurry composition and contribution of each binder material are given in section 3.3.2, where the slurry preparation procedure is discussed.

3.2 Powder Characterization

This section describes the characterization of the CPTi grade 1 powder, chosen for this study, in terms of apparent density, particle size distribution (PSD) and morphology.

3.2.1 Apparent Density

The apparent density of the CPTi powder was determined according to the ASTM B212 or the ISO 3923-1:2008 standard using a Hall flowmeter funnel. This test method gives a measurement of the loose powder density, determined by weighing the mass of free-flowing powder that fills a known volume using the following equation:

$$\rho_A = \frac{m_{powder}}{V_{cylinder}} \ , \qquad (3.2.1)$$

where ρ_A is the apparent density, m_{powder} is the mass of the powder and $V_{cylinder}$ is the known volume of the Hall flowmeter cylinder.

3.2.2 Particle Size Distribution (PSD) and Morphology

The reported particle size distribution (PSD) of the as-supplied CPTi grade 1 powder is 15-45 µm, as indicated on the material certificate found in Appendix A.1. The PSD of the powder was evaluated using a Saturn DigiSizer 5200 Particle Size Analyzer, Micrometrics Instrument Company, to verify the reported data. The facility at the Process Engineering Department of Stellenbosch University was used for this test. A prepared sample of the CPTi powder was dispersed in isopropanol and circulated through the path of a light beam. The light beam was scattered by the particles, collected by photodetector arrays and converted to electrical signals that were then processed and analysed.

Scanning electron microscopy (SEM) was used to analyse the morphology of the powder and to verify the particle size range of the CPTi powder. A Phenom Desktop SEM microscope, produced by Thermo Fisher Scientific®, was used.

3.3 Gel-casting Process

Each process step for gel-casting of titanium powder was studied and developed to create a final titanium gel-cast part with favourable mechanical properties. In this section, the numerous factors that were considered to develop a successful gel-casting process for CPTi are presented. The gel-casting process is illustrated in Figure 7, section 2.4.

3.3.1 Binder System

Titanium powder is very reactive, so selection of gel systems is important in order to avoid contamination of the microstructure, which in turn degrades the mechanical properties. Previous research has investigated the 2-Hydoxyethyl methacrylate (HEMA)/ MBAM gel system for gel-casting of titanium, however the slurry could not disperse the powder successfully, resulting in uneven settling (Piek, 2017). The primary constituent of a gel-based binder is the monomer that connects the powder particles together, giving the green part structural strength. Additional binder constituents include the solvent, dispersant, defoamer, initiator and catalyst.

Two binder systems were chosen for evaluation, based on their primary monomer: Binder 1 uses methacrylamide (MAM), chosen for its low-toxicity (Janney et al., 1998), and Binder 2 uses Isobam®, chosen for its favourable rheological properties and complete decomposition at low temperatures (Jee et al., 2006; Pollinger et al., 2016). Isobam® act both as gelling agent and dispersant (Yang et al., 2013). The

constituents of Binder 1 are listed as items 2 to 7 in Table 2 in section 3.1 and Binder 2 consists only of item 8, Isobam®.

The relative performance of the two binder systems was determined by evaluating:

i. the gel slurry formulation and mixing process,
ii. the quality and ease of the gel-casting process, and
iii. the microstructure and properties the final gel-cast material.

3.3.2 Slurry Evaluation

Recommended gel-slurry design criteria are to achieve the highest solids loading with a viscosity below 1 Pa.s at a shear rate of 20 s^{-1} (Li et al., 2008). Factors that influence the viscosity of the slurry are monomer content, monomer:cross-linker ratio, dispersant content, solid loading and mixing time. It is important that the CPTi powder remains dispersed within the gel-binder during casting in order to produce a green part with an even distribution of powder particles. The slurry was developed in two stages: first, sedimentation tests were used to determine the dispersive quality of the binder systems varying the parameters of the premix solution and secondly, the rheological behaviour and quality of the slurry was studied with varying solid loadings, powder morphology and slurry mixing times.

3.3.2.1 Sedimentation Tests

Sedimentation tests were designed to investigate the settling time of CPTi powder in a prepared premix solution, varying premix content parameters, to evaluate the dispersive quality of the system. Different premix solutions were prepared, varying the monomer content, monomer:cross-linker ratio and dispersant content. The different parameters used to evaluate the MAM/MBAM binder system are given in Table 3.

Table 3: Varied parameters of the MAM/MBAM binder system

Monomer content [wt%]	20, 30
Monomer:cross-linker ratio	6:1, 90:1
Dispersant content [wt%]	0, 0.4, 0.8

Rheology tests are only possible for a well-dispersed suspension of particles. Kennedy and Lin (2011) used sedimentation tests to evaluate the degree of dispersion of 316L stainless steel particles in a polymer binder for gel-casting. A similar approach was followed to determine the suitability of the binder systems, chosen for this study, for CPTi powder.

20 ml of various premix solutions were prepared with a DLab OS40-Pro overhead stirrer. The premix solutions for the MAM/MBAM system were prepared by first dissolving the monomer and cross-linker in the solvent for 2 hours at room temperature at a speed of 450 rpm. The dispersant was then added, and the solution

mixed for another hour at the same speed as before. For the Isobam® binder system, 0.3 wt% (based on powder weight) of Isobam® was dissolved in the solvent for 1 hour at room temperature to form a premix solution, using the same equipment and mixing speed as for the other system.

For each sedimentation test, 1 g of CPTi powder was added into approximately 20 ml of premix solution. The sedimentation behaviour of the powder slurry was studied by logging the position of the interface between the sediment and the liquid above, in a transparent measuring cylinder. The time was measured for the interface boundary to move 10 ml down as the powder particles settle due to the gravitational force.

3.3.2.2 Higher Solid Loading Slurry Quality

The premix solutions with the best determined dispersive quality were further used to develop the optimal slurry. Table 4 summarizes the different solid loadings and slurry mixing times investigated.

Table 4: Varied parameters for higher solid loading tests

Solid loading [vol%]	45, 55
Slurry mixing time [hrs]	4, 8, 12

The suitable solid loading values for making a usable slurry are defined by the apparent and tap densities of a powder (Kennedy and Lin, 2011). It is unlikely that a closer packing of the solid particles in the slurry will be achieved than the apparent density of the powder. The reported apparent density of the CPTi powder used in this study is 2.6 g/cm^3, which is 57 % of the theoretical density (4.51 g/cm^3) of the powder. This means that a maximum theoretical solid loading of 57 % is possible, setting the upper limit for this study at 55 vol%. The values chosen are also in line with literature. The typical solid loading value for PIM feedstock is between 55 and 60 vol% (Barreiros et al., 2008; German, 2003). Various studies on the gel-casting of metal powders have found the optimal solid loading of a metal powder slurry to be in the range of 40 to 60 vol% (Duan et al., 2014; Pollinger et al., 2016; Wang et al., 2009).

Most slurries for gel-casting have been prepared using the traditional ball-milling process, mixing for extended periods of time (up to 24 hours), which provide effective mixing of the powders by breaking up the agglomerates to achieve stable slurry dispersions (Guo et al., n.d.; Pollinger et al., 2016; Yang et al., 2011). The mixing times of 4, 8 and 12 hours were chosen for this study to investigate whether the mixing time, using an overhead mixer, has a similar effect on the quality of the slurry than using a ball-milling machine.

The slurries were prepared by first preparing the premix solution as described in section 3.3.2.1. The powder was then added at the various solid loadings and mixed

at the various mixing times listed in Table 4. The spherical powder that was used, is the CPTi powder mentioned in section 3.1.1.

The slurry quality was observed by how well the slurry kept the powder particles dispersed when mixing was stopped, and the slurry was cast. The ease of casting the slurry by drawing the slurry into a 60 ml syringe and injecting the slurry into the mould was another indicator of the quality of the slurry. A successful slurry keeps the powder suspended while casting and ensures a suitable fluidity for the slurry to flow into all the empty spaces of the mould.

3.3.3 Slurry Preparation

A well dispersed slurry with optimal solid loading, monomer- and dispersant content and monomer:cross-linker ratio is required to achieve a suitable sintered density with minimum shrinkage. These factors were studied in the previous section, 3.3.2, to obtain the optimum parameters for slurry preparation, discussed in this section.

Formulas for preparing powder injection moulding (PIM) feedstock were used to determine the powder-binder ratios in this study (German and Bose, 1997). The preparation of a PIM feedstock is similar to gel-casting slurry preparation in that it involves the preparation of a homogeneous powder-binder mixture that is capable of flowing. However, for PIM the solid loading and viscosity of the mixture are much higher than for gel-casting and requires pressure to inject the heated feedstock. Nevertheless, the same mathematical relationships apply for gel-casting slurries as do for PIM feedstock.

The solid loading (φ) of the slurry is the ratio of the volume of powder (V_{powder}) to the total volume of the slurry (V_{Total}) and can be expressed as:

$$\varphi = \frac{V_{powder}}{V_{Total}}. \tag{3.3.1}$$

The total volume of the slurry consists of the volume of the powder and the volume of the binder. The relationship between volume (V), mass (m) and density (ρ) is:

$$V = \frac{m}{\rho}, \tag{3.3.2}$$

and the weight fraction of a single component in the slurry was calculated as:

$$W_{component} = \frac{m_{component}}{m_{total}}. \tag{3.3.3}$$

Substituting equations 3.3.2 and 3.3.3 into equation 3.3.1, the equation for solid loading becomes:

$$\varphi = \frac{W_P/\rho_P}{W_P/\rho_P + W_B/\rho_B}, \tag{3.3.4}$$

where W_P and W_B are the weight fractions of the powder and binder, respectively, and ρ_P and ρ_B are the theoretical full densities of the powder and binder, respectively. Furthermore, the density of the slurry (ρ_{slurry}) was found by a law of mixtures as:

$$\rho_{slurry} = \varphi\rho_P + (1-\varphi)\rho_B \ . \qquad (3.3.5)$$

Formulation on a weight basis was used to mix the slurry. The weight fraction of the powder was derived from equation 3.3.4 by linking the relation between volume and weight by substituting equation 3.3.5 into equation 3.3.4. The weight fraction of the powder (W_P) was then calculated as:

$$W_P = \frac{\varphi\rho_P}{\varphi\rho_P+(1-\varphi)\rho_b} \ . \qquad (3.3.6)$$

Figure 18 and Figure 20 use flow diagrams to illustrate the slurry preparation of the MAM/MBAM and Isobam® systems, respectively. An OS40-Pro overhead stirrer (supplier: United Scientific) was used for preparing the slurry.

3.3.3.1 MAM/MBAM System (Binder 1)

The amounts of additives were calculated as a weight percent (wt%) of either the premix solution or the monomers, as indicated in Figure 18. The powder was calculated as a volume percent (vol%) of the total slurry volume. 20 wt% monomer, at a 6:1 ratio, was dissolved in deionized water for 1 hour at a mixing speed of 450 rpm and room temperature to form the premix solution. The dispersant content, 0.8 wt% of the premix content, were added to the premix solution and mixed for 30 minutes at 450 rpm. After the dispersant had mixed through the premix solution, 55 vol% CPTi powder was added, and the mixture was mixed for 90 minutes at 650 rpm. After adding the initiator and catalyst, the slurry was mixed at 350 rpm for 6.5 minutes, allowing the polymerization reaction to start, and then cast with sufficient flowability. The additives were added through a port in the lid of the glass mixing vessel. The slurry mixing setup is shown in Figure 19.

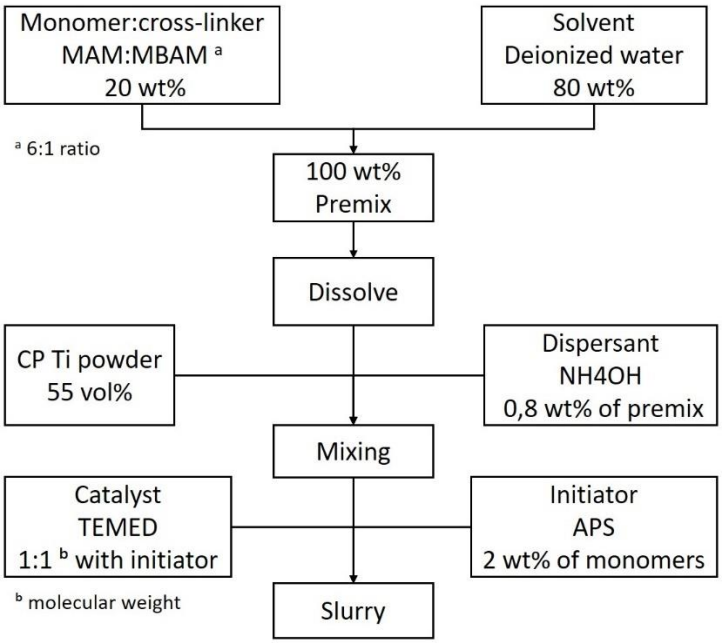

Figure 18: Slurry preparation using MAM/MBAM system

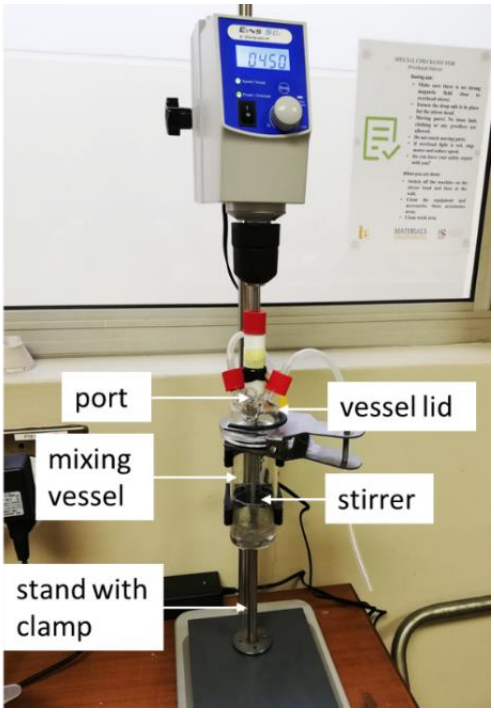

Figure 19: Slurry mixing setup with overhead stirrer

3.3.3.2 Isobam® System (Binder 2)

The calculated amount of Isobam® as a weight percent (wt%) of the CPTi powder, was dissolved in deionized water for 1 hour at 450 rpm and room temperature. After dissolving, 55 vol% of CPTi powder was added to the mixture and mixed for 90 minutes at 650 rpm before casting. The same slurry mixing setup as for the MAM/MBAM system was used.

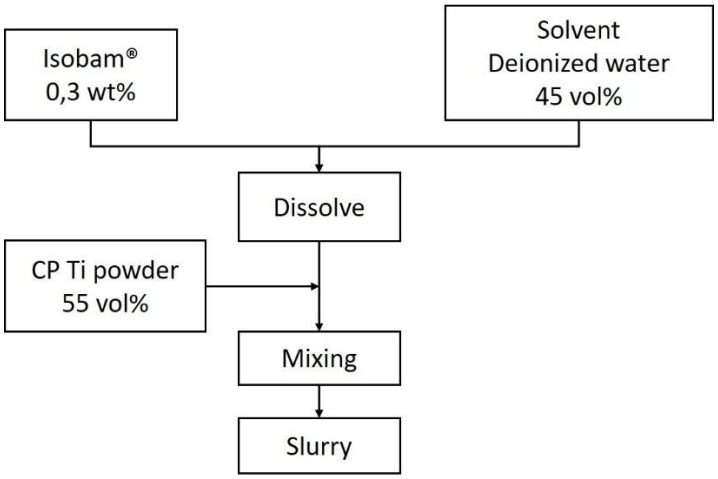

Figure 20: Slurry preparation using Isobam® system

3.3.4 Mould Design

A rectangular bar mould was manufactured using a FormLabs Form 2 3D printer based on stereolithography (Figure 21). A stereolithography (SLA) 3D printer uses a laser to cure solid isotropic parts, layer-by-layer, from a liquid photopolymer resin. This technology creates products with high resolution, leading to a very smooth surface finish. It is thus ideal for creating moulds, relatively inexpensive, that render near-net-shape gel-cast parts with a good surface finish, minimizing the need for post-processing such as machining. The dimensional changes that the gel-cast part experiences throughout the process of drying, binder burnout and sintering, must be accounted for in the design of moulds. Noting that titanium powder mass is conserved through all the process steps, the solids loading can be used to predict the isotropic shrinkage of a gel-cast part by assuming that it will be sintered to 90 % of the theoretical density of titanium in the last process step. This value of shrinkage is used to reverse engineer the casting mould in order to achieve a sintered rectangular bar of 75.3 x 14.9 x 13.6 mm. By monitoring the dimensional changes during processing, the assumption of isotropic shrinkage can be evaluated.

The following equation can be used to predict the isotropic shrinkage, *Y*, of a gel-cast part:

$$\frac{\rho_0}{\rho_f} = (1 - Y)^3, \quad where\ Y = \frac{\Delta L}{L_0}. \tag{3.3.7}$$

Y refers to the isotropic shrinkage that a part experiences as it densifies from the original green density (ρ_0) to the final sintered density (ρ_f). The mould was 3D printed from resin using a FormLabs Form 2 3D printer. The settings used for the printer is shown in Table 5. AutoCAD® drawings of the mould, from which the .stl files are created for the print, are found in Appendix D.1. The mould cavity was designed with dimensions of 88.7 x 17.6 x 16 mm, using the equation above to account for isotropic shrinkage of a 55 vol% φ slurry and assuming a final sintered density of 90 %. The bottom part of the mould is designed to detach from the mould for easy demoulding of the rectangular bars, as shown by the blown up view of the mould in Figure 21. The 8 mm diameter hole in the bottom part of the mould is to allow for injection of the slurry from the bottom, using a syringe, ensuring that the slurry displaces the air in the mould as it is cast and minimising trapped air in the casting.

Table 5: FormLabs Form 2 3D printer settings

Material	Clear Resin
Layer thickness [mm]	0.05
Supports	Yes

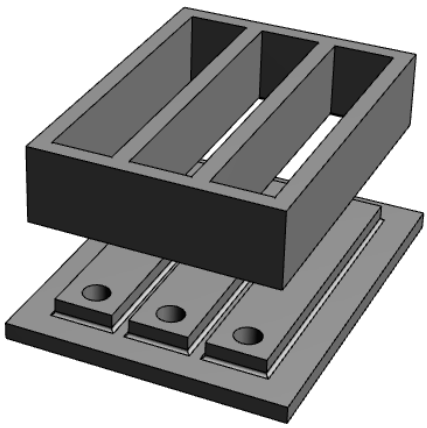

Figure 21: Schematic of rectangular bar mould

3.3.5 Casting and Polymerization

The slurry is cast into resin 3D printed moulds, after adding the initiator and catalyst to the slurry, while it still has a sufficient fluidity. Good fluidity of the slurry ensures that all the empty spaces in the mould are evenly filled by injecting the slurry with a 60 ml syringe. Radical polymerization takes place between 8 and 13 min after adding the initiator and catalyst to the slurry at room temperature.

After the slurry was cast into the mould, it was de-aired under vacuum to evacuate all air from the cast slurry. Trapped air in the cast slurry can lead to strength limiting defects in the gelled part, such as big pores that create stress concentration regions in the microstructure allowing for cracks to form. A Buehler Cast ‘n Vac 1000 castable vacuum system with a Neuberger vacuum pump, with a maximum pressure rating of 4 bar, was used for de-airing. After de-airing, the cast slurry was held at 60 ˚C for 2 hours in a Gallenkamp Hot Box Oven to ensure complete polymerization and the formation of the green body. It should be noted that at this point, there is still a significant amount of water contained in the gelled part.

3.3.6 Drying

After polymerization in the oven, the green body was demoulded and dried in a vacuum at room temperature for 12 hours. Drying is the first step of debinding, during which most of the solvent in the green body, still present after gelation, is removed. Though most of the solvent evaporates, the backbone polymers remain to provide strength to the green body and retain the shape during this initial debinding stage (German and Bose, 1997). The backbone polymers, MAM and MBAM, burn off during binder burnout.

3.3.7 Thermal Gravimetric Analysis

Thermal gravimetric analysis (TGA) was performed on the gel-cast green body to determine the temperature range where the binder burns off and to compare the results to published data, as presented in section 2.4.4. A TA Instruments TGA-5500 was used to determine the mass loss profile of the sample through a temperature range of 50-850 ˚C at a heating rate of 5 ˚C/min in a high purity argon atmosphere with a gas flow rate of 50 ml/min.

3.3.8 Binder Burnout and Presintering

Pyrolysis involves the thermal decomposition of materials at elevated temperatures in an inert atmosphere. The binder of the dried green body samples was removed by pyrolysis, during the binder burnout step before sintering. A binder burnout heating profile was designed based on the study by Janney et al. (1998), mentioned in section 2.4.4, and the TGA results obtained from the analysis described in section 3.3.7.

The dried green samples were heated in a quartz tube to 220 ˚C at a heating rate of 10 ˚C/min and then further heated at 1 ˚C/min to 400 ˚C, where they were kept for 2 hours to achieve complete burnout of the binder system. The sample was then heated to 650 ˚C at 5 ˚C/min and kept there for 30 min to pre-sinter the sample, allowing some degree of sinter bond neck growth between the particles by which the sample obtains handling strength. The samples were then cooled back to room temperature before removing them from the quartz tube. The entire heat treatment was conducted in an argon atmosphere with a gas flow rate of 200 ml/min. High purity argon gas, supplied by Afrox, was used for this purpose. Yttria stabilised zirconia substrates (YSZ) were chosen instead of alumina substrates to place the CPTi specimens on in the tube. Titanium reacts with oxygen from both the zirconia (ZrO_2) and the alumina (Al_2O_3) substrates to form a thin TiO layer. However, no interfacial reaction product occurs between YSZ and the formed TiO coating, since ZrO_2 can be partially reduced without decomposition at elevated temperatures, but not so for Al_2O_3 and fused silica substrates (Brust et al., 2016). Oxygen reacts with titanium at elevated temperatures to form titanium oxide and causes the microstructure to become brittle, thus is an unwanted effect.

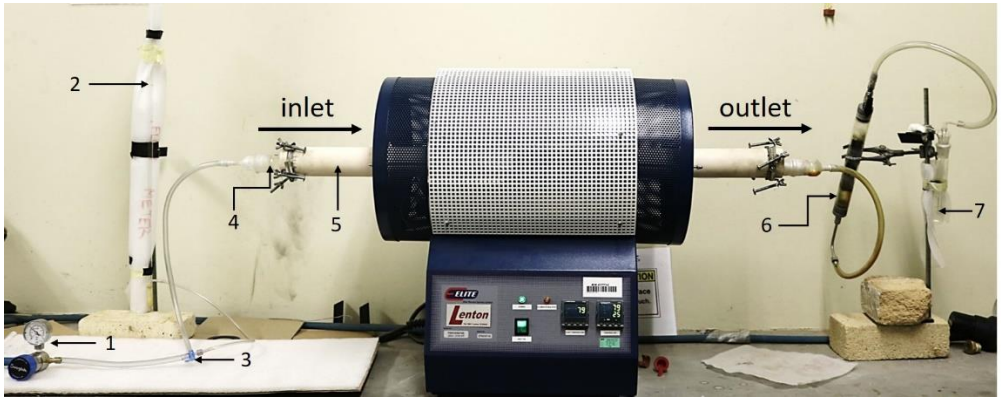

Figure 22: Binder burnout setup

An Elite™ TSH 15/25/180 horizontal tube furnace with an Eurotherm controller was used for the binder burnout process. Figure 22 presents an illustration of the furnace setup for the binder burnout process. A description of the numbered components in the figure is listed below:

1. Swagelok™ pressure-reducing regulator
2. Bubble flowmeter
3. T-valve
4. Quartz tube
5. Alumina tube
6. Activated carbon column
7. Water bubbler

A bubble flowmeter was used to measure the gas flow with a pressure-reducing regulator to control the flow. A glass column containing activated carbon (AC) was used at the outlet side of the tube to adsorb the nitrogen oxide (NOx) gasses produced during binder burnout. A water bubbler was used in-line after the AC column to further purify the emissions. The step-by-step experimental procedure for the binder burnout process, including experiment setup, running the furnace, removing the samples and cleaning the quartz tube and zirconia substrates, is given in Appendix B.1.

3.3.9 Sintering

After binder burnout and presintering of the samples, they were sintered in an Elite™ TSH 15/25/180 horizontal tube furnace with an Eurotherm controller to obtain near-full sintered density. This is the same furnace used for binder burnout, however the quartz tube was removed, and the furnace's alumina tube was used. It is important that all binder is burnt off before sintering, as any residual binder will damage the turbo pump used in the setup. The samples were sintered under high vacuum. Before sintering, a low vacuum of 10^{-2} mbar was pulled in the tube, using an Adixen 2015 SD Pascal rotary vane pump. The system was then flushed with high purity argon, supplied by Afrox, to further assist with removing oxygen from the system before a high vacuum of 10^{-6} mbar is pulled, using a Varian Turbo-V 81 M turbo pump. A MKS 970-DS Cold Cathode Transducer was used to monitor the pressure in the system. The vacuum system is shown in Figure 23b, and supplied by Vacutec (Pty) Ltd. The heating cycle was started after reaching a vacuum of at least 10^{-5} mbar to ensure that the titanium samples do not react with any oxygen. The samples were heated at a rate of 10 ˚C/min and sintered in yttria-stabilized zirconia crucibles at a temperature of 1200 ˚C for 2 hours. After the 2-hour dwell, the cooling cycle was started, allowing the furnace to cool under vacuum until it reaches 300 ˚C. Argon was then allowed to flow through the system to assist with further cooling of the samples and for cooling of the rotary pump. Special care must be taken to follow the sintering procedure, as given in Appendix B.2, to prevent damage of the vacuum system.

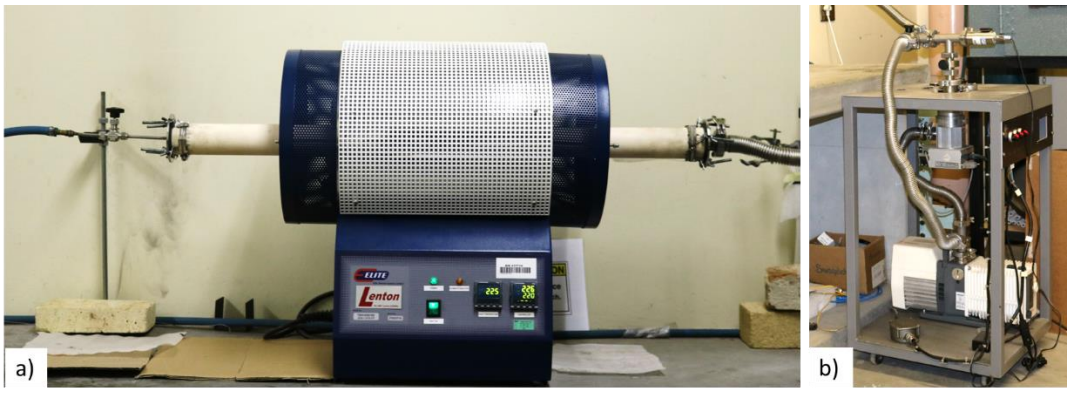

Figure 23: Sintering setup showing the (a) tube furnace and the (b) vacuum system

3.4 Characterization Techniques

In this section, the experimental procedures are given for determining the density of the gel-cast part throughout the gel-casting process, evaluating the mechanical properties of the final sintered part and analysing the microstructure.

3.4.1 Density

The green density of a gel-cast part was calculated as the density of the slurry mixture according to equation 3.3.5. The sintered density was determined according to the ASTM B962 standard, based on the Archimedes Principle. The test pieces are vacuum impregnated with oil to seal the surface-connected pores. The sintered density (D_s) is calculated as:

$$D_s = \frac{A\rho_w}{B-F}, \qquad (3.4.1)$$

where:

A = the mass of the test specimen in air, g,
B = the mass of the oil-impregnated test specimen, g,
F = the mass of the oil-impregnated test specimen in water with the mass of the specimen support tared, g, and
ρ_w = the density of the water, g/cm^3.

The test specimens were weighed using a Kern ABT 120-5DM analytical balance with a resolution of 0.1 mg. The dimensions of the gel-cast rectangular bars were measured after drying, binder burnout and sintering using a standard Vernier caliper with an accuracy of 0.01 mm. The difference between the dimensions of the mould cavity and the sintered part produced from the mould was calculated and expressed as a percent shrinkage according to the ASTM B610 standard, using equation 3.3.7.

3.4.2 Mechanical Behaviour

3.4.2.1 Tensile Testing

Round dog-bone-shape tensile specimens were prepared and used to test the mechanical behaviour according to the ASTM E8M standard. This standard requires a 5:1 ratio between the gauge length and the diameter of the gauge length. The mechanical properties that were obtained from the test include yield strength, elasticity, ultimate tensile strength (UTS) and elongation at fracture. An MTS Criterion Model 44 Universal Testing Machine (Figure 24) was used to perform the tensile tests, using TestWorks4 software to collect and process the load and crosshead displacement data. The crosshead speed was 0.5 mm/min.

The tensile specimens, showed in Figure 25, were 62 mm long with a gauge length of 28 mm and gauge length diameter of 5 mm. Each specimen ends in a 12 mm M12 thread that allows the specimen to be screwed into the grips. This means that, although the entire specimen is 62 mm long, it is only free to elongate over 38 mm

between the grips. Furthermore, the elongation of the R5 fillet radius from the M12 thread to the 5 mm gauge length is negligible in comparison to the elongation over the gauge length. Thus, strain (ε) was calculated as:

$$\varepsilon = \frac{\Delta l_{crosshead}}{l_{gauge}} \tag{3.4.2}$$

where $l_{crosshead}$ is the crosshead displacement and l_{gauge} is the gauge length of 28 mm. The stress was calculated, using the load data and the actual cross-sectional area of the specimen. The measured gauge length diameter for the specimens varied between 4.92 mm and 5 mm.

A CAD drawing for manufacturing of the tensile specimens is given in Appendix D.2. It should be noted that two specimens were incorrectly machined and were approximately 72 mm long with a 38 mm gauge length. In these cases, the gauge length in equation 3.4.2 was replaced with 38 mm.

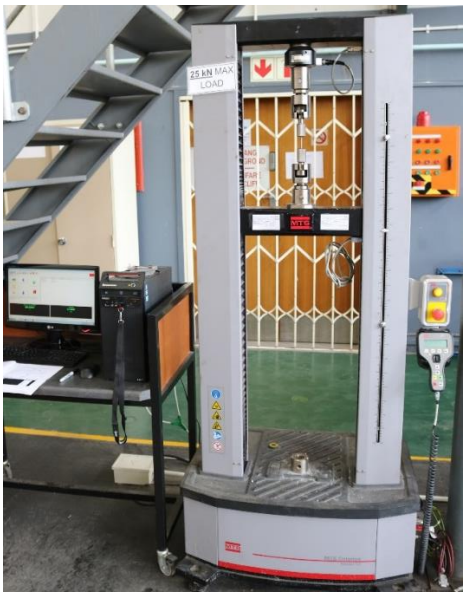

Figure 24: MTS Criterion Model 44 universal testing machine

Figure 25: Tensile specimens

3.4.2.2 Hardness Testing

Hardness testing was performed on the sintered specimens according to the ASTM E18 standard, using a Zwick/Roelle Rockwell Hardness Tester. A 1/16-inch carbide ball indenter was used with an applied force of 100 kgf to determine the hardness values on the Rockwell B scale. A calibration block with a hardness value of 82.22 HRBW was used to calibrate the machine.

3.4.3 Microstructural Analysis

3.4.3.1 Optical Microscopy

An Olympus GX51 microscope was used to study the characteristics of the microstructure and an Olympus SZX7 stereo microscope was used to study the surface defects. Both microscopes use an Olympus SC30 CMOS colour camera and Stream Essentials 1.9.4 software for analysis. Characteristics of the microstructure studied include porosity distribution, pore defects and the degree of sinter bonds formed. The porosity distribution gave an indication of whether the titanium particles were distributed evenly during casting or whether settling occurred. Sample preparation for microstructural analysis was adapted from the Struers® application notes, *Metallographic preparation of titanium* (Taylor and Weidmann, 2016), and the procedure followed is shown in Table 6. A Micracut 150 low speed precision cutter was used to cut the samples to size for hot mounting. A Buehler SimpliMet™ 3000 was used to mount the samples after cutting, and a Buehler Alpha™ & Vector Power Head was used for grinding and polishing of the samples.

Table 6: Grinding and Polishing Method (adapted from Taylor and Weidmann, n.d.)

	Grinding 1	**Grinding 2**	**Polish 1**	**Polish 2**
Surface	SiC-paper, 800 grit	SiC-paper, 1000 grit	MD Largo	MD Chem
Suspension	-	-	DiaDuo-2, 9 µm	OP-S NonDry, 0.4 µm
Lubricant	Water	Water	-	-
rpm	180	180	180	180
Force (N)	25	25	25	25
Time (min)	1.5	1.5	5	5

3.4.3.2 Scanning Electron Microscopy (SEM)

A Zeiss Merlin GeminiSEM field emission scanning electron microscope at the Central Analytical Facility (CAF) of Stellenbosch University was used for topographical and elemental analysis of the sintered specimens. The fractured surfaces of the tensile test specimens were also studied with SEM to determine whether microstructural defects, such as porosity or cracks, caused fracture. Energy dispersive spectroscopy (EDS) was used to determine the distribution of elements in the sintered microstructure and in order to determine whether carbon and oxygen contamination occurred in the sintered part. EDS maps and line-scans were used for elemental analysis.

4 Results and Discussion

This chapter presents the results of this study, with relevant data collected as described in Chapter 3. The chapter starts with the powder characterization results, reporting the apparent density and particle size distribution analysis. The slurry optimization results of the sedimentation tests and slurry quality are presented and discussed, as well as the manufacturing of the mould for titanium gel-casting. Critical aspects of the gel-casting process, over all the process steps from casting to sintering, are highlighted and discussed. The microstructure and mechanical properties of the sintered specimens are presented, followed by a discussion regarding the insights gathered from the analysis.

4.1 Powder Characterization

4.1.1 Apparent Density

The apparent density of the supplied CPTi powder was established according to the ISO 3923-1:2008 standard, using a Hall Flowmeter. The orifice diameter of the funnel is 2.5 mm and the volume of the cylindrical cup is 25 cm^3. The arithmetic mean of the apparent density from three tests was calculated as 2.51 g/cm^3 with a standard deviation of 0.01 g/cm^3. The calculated apparent density correlates well with the specified value of 2.60 g/cm^3 of the supplied CPTi powder. The apparent density of the powder is 56 % of the theoretical density (4.51 g/cm^3). Thus, the maximum solid loading of the slurry is 56 vol% as it is unlikely that closer packing than the tap density will be achieved in the binder. The test data is given in Appendix C.1.

4.1.2 Particle Size Distribution (PSD)

The titanium powder sample for PSD analysis was suspended in isopropanol with a refractive index (RI) of 1.376. The sample was sonicated for 60 s with an ultrasonic intensity of 60 %. The samples were tested at a flow rate of 12 l/min and circulation time of 60 s. The results correlate to the supplied data from AP&C®. The results are given in Table 7.

Table 7: PSD for CPTi powder, as measured by laser diffraction

Description	Specified	Measured
$\boldsymbol{D_{10}}$	17 µm	16.5 µm
$\boldsymbol{D_{50}}$	33 µm	30.9 µm
$\boldsymbol{D_{90}}$	45 µm	43.7 µm
$\boldsymbol{< 15\ \mu m}$	6 vol.%	7.3 vol.%
$\boldsymbol{> 45\ \mu m}$		7.7 vol.%

From Figure 26 it can be seen that the volume frequency percent graph has a long tail to the left. This indicates that the powder has a wide range of fine powder

particles below the mean particle size of 30.4 µm. It is recommended that these fines (powder particles in the size range of 5-30 µm) be removed in further studies. Finer powder particles have more surface area that require a higher concentration of dispersant to successfully disperse the particles in a binder. The mode of the data was found to be at a particle diameter of 35.7 µm, and it can be seen from Figure 26 that the highest volume frequency of particles is around this particle size.

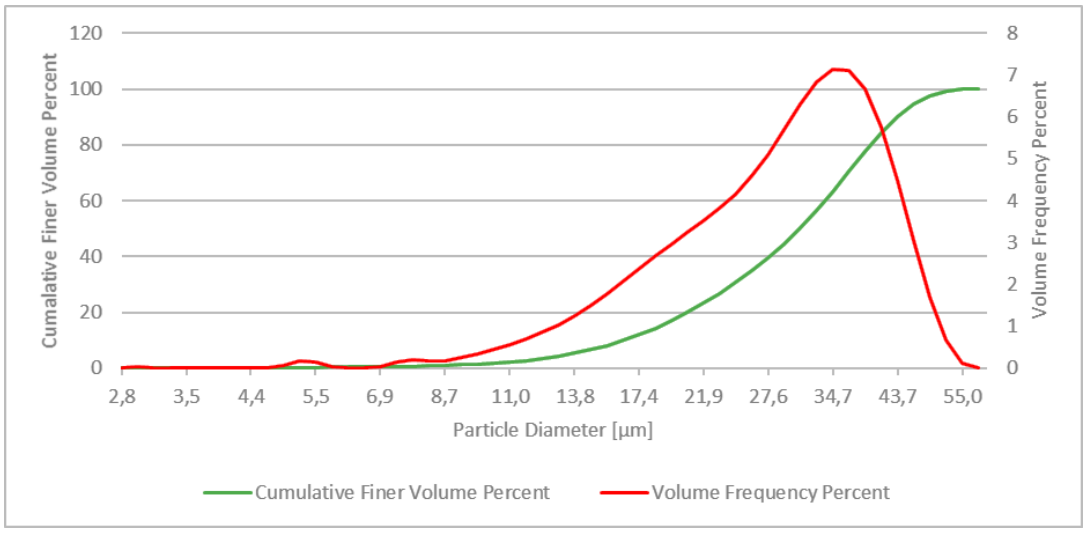

Figure 26: Volume Frequency vs. Diameter

The SEM micrographs, Figure 27, of the powder verifies the PSD results and presents the findings, as mentioned above, well. The SEM images show larger powder particles around 35 µm with a wide range of fine particles in between. The micrographs also affirm the sphericity of the powder.

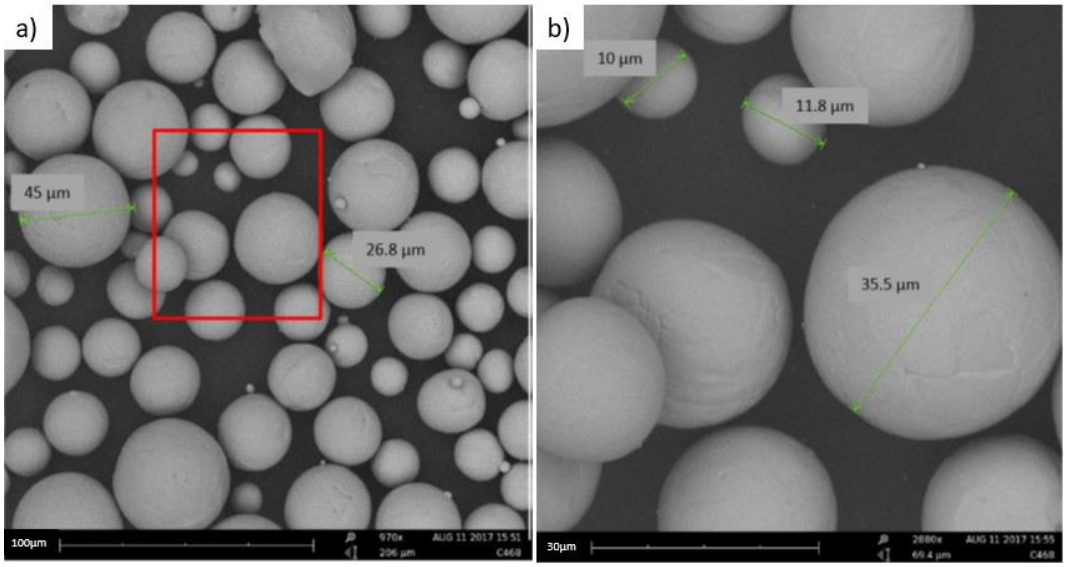

Figure 27: SEM micrographs or morphology and distribution of particle sizes

4.2 Optimization of Slurry

4.2.1 Sedimentation Tests

Figure 28 shows a series of photos of the measuring cylinders, illustrating the progress in sedimentation, with increasing settling time from left to right. The interface between the sediment and the liquid above is not so clear, because of finer powder particles that stay suspended for a longer time than the majority of the powder. Nevertheless, the boundary becomes clear after an initial period as the sediment moves downward due to the effect of gravity. The liquid above the sediment clarifies after a long time, as it contains a small fraction of fine particles. The arrows in Figure 28 indicate the boundary between the sediment and liquid above. It is the downward movement of this boundary that is measured as a function of time.

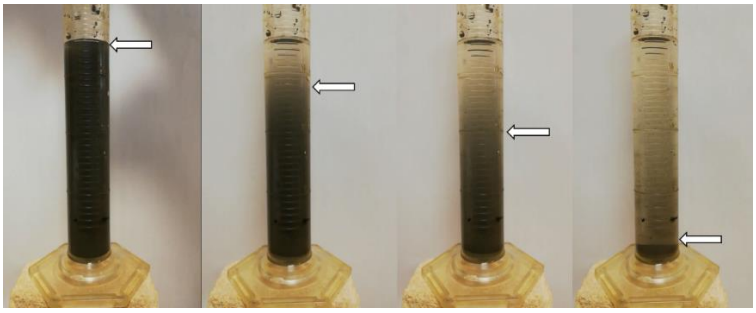

Figure 28: Progress of sedimentation, with arrows indicating the sediment boundary movement as sedimentation time increases from left to right

Figure 29 presents the sedimentation behaviour of 1 g CPTi powder in MAM/MBAM and Isobam® premix solutions. The Isobam® premix solution was prepared using Isobam® content of 0.3 wt%. The MAM/MBAM solutions was prepared with 20 wt% monomers content at a monomer:cross-linker ratio of 6:1 and with dispersant (NH_4OH) contents of 0, 0.4 and 0.8 wt%, respectively. The monomers would not dissolve in the premix solution for this system, increasing the monomer content to 30 wt% or the monomer:cross-linker ratio to 90:1. Figure 29 also illustrates that increasing the dispersant content from 0 to 0.8 wt%, increases the settling time of 1 g of CPTi powder and thus decreases sedimentation rate. The graph illustrates the time it takes for the sediment boundary to cross various volume marks on the measuring cylinder. The settling time increased by 105 % with dispersant content increasing from 0 to 0.4 wt%, but only with 7.3 % when increasing dispersant content from 0.4 to 0.8 wt%. A total increase in settling time of 120 % was observed, using 0.8 wt% of dispersant against using no dispersant at all.

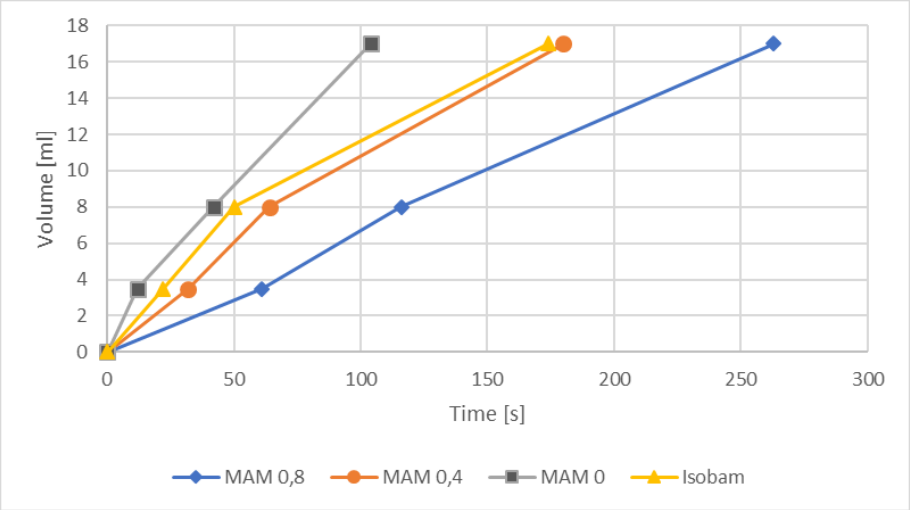

Figure 29: Sedimentation behaviour for 1 g CPTi powder in different premix solutions

It is clear that neither the MAM/MBAM nor the Isobam® binder system suspends the CPTi particles. This can be explained through reviewing the physics involved in the dispersion of particles in a liquid. Gel-casting was developed using ceramic particles, that typically have lower density and smaller particle size than metal particles. Thus, the surface charge of a particle in a ceramic powder slurry has a greater effect on the dispersion of the particles than the particle density. A novel approach of preparing a CPTi slurry was developed, as explained in section 3.3.3.1, taking the titanium particle weight into account and using Stokes Law to successfully suspend the powder particles in the slurry. This novel approach is discussed further in section 4.4.

4.2.2 Slurry Quality

The effect of different mixing times and solid loadings, as listed in Table 4, were investigated with a standard premix solution based on the results of the sedimentation tests. A 20 wt% MAM/MBAM premix solution with a monomer:cross-linker ratio of 6:1 and dispersant content of 0.8 wt% showed the best behaviour, and was used.

4.2.2.1 Mixing Time

The effect of the mixing time after adding the powder to the premix solution was investigated, keeping the mixing speed constant at 450 rpm. A solid loading of 55 vol% was used to prepare the slurry. A similar sedimentation test, as described in section 4.2.1, was done on the slurry after 4, 8 and 12 hours of mixing. The results are illustrated in Figure 30. It is seen from the graph that there is no significant difference in sedimentation behaviour of the slurry by varying the mixing time, using the overhead mixing system. Ceramic gel-casting slurries have been prepared using the traditional ball milling process for mixing, which allows effective mixing of powders in the slurry and allows aging time for hydroxylation of particle surfaces to achieve a stable slurry dispersion (Pollinger et al., 2016). It was observed that droplets form on the inside wall of the glass mixing vessel with the increase of mixing time due to evaporation of the solvent. This may effectively result in a higher solid loading slurry than initially intended.

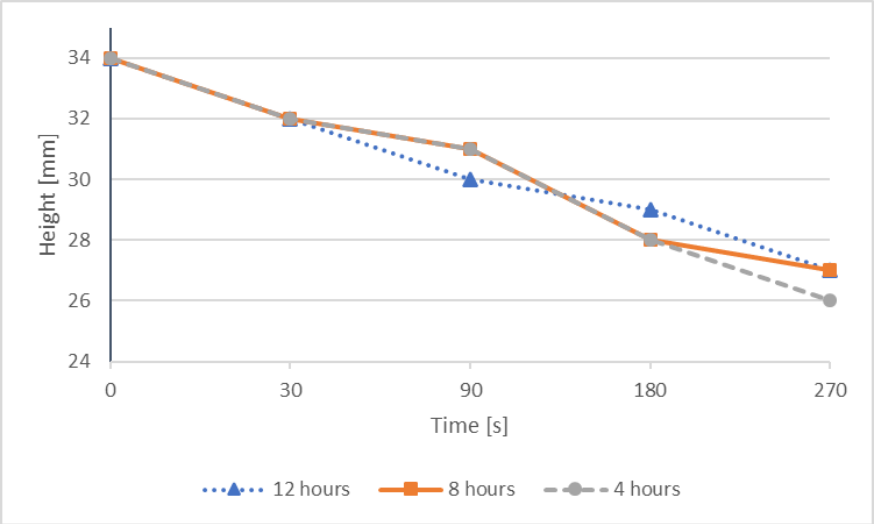

Figure 30: Sedimentation behaviour for different mixing times

4.2.2.2 Solids Loading

Figure 31 illustrates that both 45 vol% and 55 vol% solid loading slurries fail to suspend the CPTi powder particles after mixing for 4 hours. The monomer content was kept constant at 20 wt% with a monomer:cross-linker ratio of 6:1 and

dispersant content of 0.4 wt% for the 45 vol% φ slurry and 0.8 wt% for the 55 vol% φ slurry. The dispersive quality of the 55 vol% φ slurry did not improve by increasing the mixing time to 8 hours, as seen in Figure 31c. These results support the findings from section 4.2.1, that the particle weight of titanium powder has a more significant effect on the dispersion of a particle in the binder system than the surface charge of the particle, and a novel approach is needed to suspend the titanium particles in the slurry.

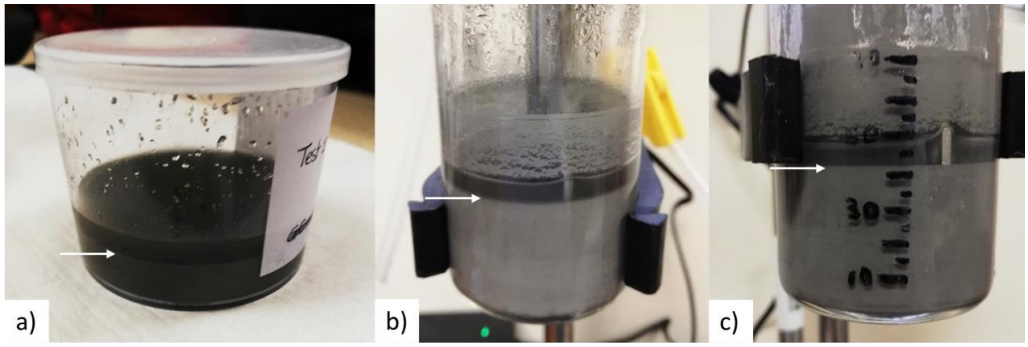

Figure 31: Powder settling of (a) a 45 vol% φ slurry mixed for 4 hours, (b) a 55 vol% φ slurry mixed for 4 hours and (c) a 55 vol% φ slurry mixed for 8 hours

4.3 SLA 3D Printed Rectangular Bar Mould

The rectangular bar mould manufactured with a SLA 3D printer, with two polymerized green parts still in the mould, is shown in Figure 32. The mould consists out of two parts: part 1 is the main body of the rectangular bar mould and part 2 is the removable bottom part of the mould with a 8 mm diameter hole for injecting the slurry from the bottom of the mould with a 60 ml syringe. Injecting the flowable slurry from the bottom ensures minimum air trapped in the cast part. Part 2 of the mould was designed to detach from the main mould to ease the demoulding of the green part by pushing the part out, as illustrated in section 3.3.4. The mould wall between rectangular bars were chosen to be 5 mm thick for the purpose of shape retention during the polymerization process, during which the mould is heated. The parts of the mould were produced with a layer thickness of 0.05 mm to ensure structural stability and a smooth surface finish, which can be seen from Figure 32. No mould release agent was necessary.

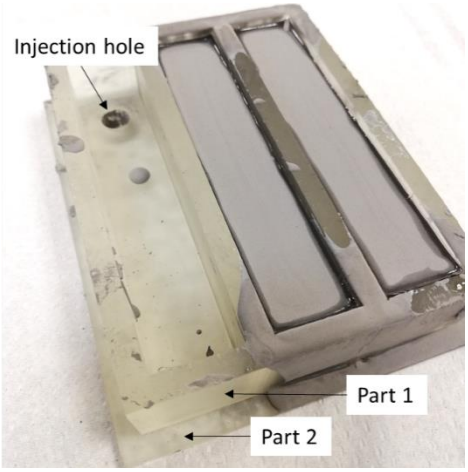

Figure 32: Resin 3D printed mould

4.4 Gel-casting Process

4.4.1 Casting, Gelation and Demoulding

Based on the findings of the slurry optimization tests, discussed in section 4.2, a novel approach was followed to form a stable metal powder slurry, as explained in section 3.3.3.1, with the slurry formulation as given in Figure 18. The reason for the improved quality of the slurry with the novel approach is that the stability of a metal powder slurry is affected more by the density of the particles than by electric charges on the surface of the metal powder particles (Ohkawa et al., 2004). The zeta potential of a slurry, relates to the surface charge of the particles, and gives an indication whether a slurry has sufficient electrostatic repulsion to remain dispersed (Particle Sciences, 2012). The zeta potential of metal slurries plays a lesser role in the dispersion of the particles than in ceramic slurries. The principle of Stokes Law was thus useful in obtaining a stable titanium slurry. The law explains the rate of sedimentation of a particle in a medium:

$$S = \frac{D^2(\rho_1 - \rho_2)g}{18\mu}, \qquad (4.4.1)$$

where S is the rate of sedimentation, D the diameter of a powder particle, ρ_1 and ρ_2 are the densities of the powder and medium respectively, μ is the viscosity of the medium and g is the gravitational constant.

Because of the size difference between ceramic and metal powder particles, metal powder particles being typically larger than ceramic powder particles are heavier. The mass of an average titanium particle (40 µm) compared to that of an alumina particle (5 µm) is 0.151 µg and 0.259 pg, respectively. Thus, the effect of gravitational forces is more significant on larger particles, increasing the sedimentation rate. In order to decrease the rate of sedimentation, one can either

decrease the particle diameter or increase the viscosity of the medium. It is a significant safety hazard to work with even finer titanium powder particles than specified in this study. Finer titanium powder can more easily form dust clouds that can explode. Therefore, the polymerization reaction was initiated, allowing the viscosity of the slurry to increase just enough to keep the powder particles suspended and still have a sufficient fluidity to cast the slurry. Figure 33a shows a successfully cast titanium slurry using this approach. In a previous study on titanium gel-casting a prominent liquid layer formed on top of the cast slurry indicating sedimentation of the powder particles (Piek, 2017). No prominent liquid layer formed on this cast slurry, indicating that the powder stayed dispersed in the slurry after casting. Even distribution of the powder particles is confirmed by optical micrographs of the microstructure of the sintered parts in section 4.4.4.

After casting the slurry, the slurry was de-aired using a Buehler Cast ‘n Vac 1000 vacuum system with a Neuberger vacuum pump. The vacuum pump has a maximum pressure rating of 4 bar. After de-airing, the mould was placed in an oven at 60 ˚C to allow complete polymerization of the part (Figure 33b) after which the green parts were demoulded with ease and without the use of a demoulding agent (Figure 33c). The demoulded parts showed a smooth surface finish.

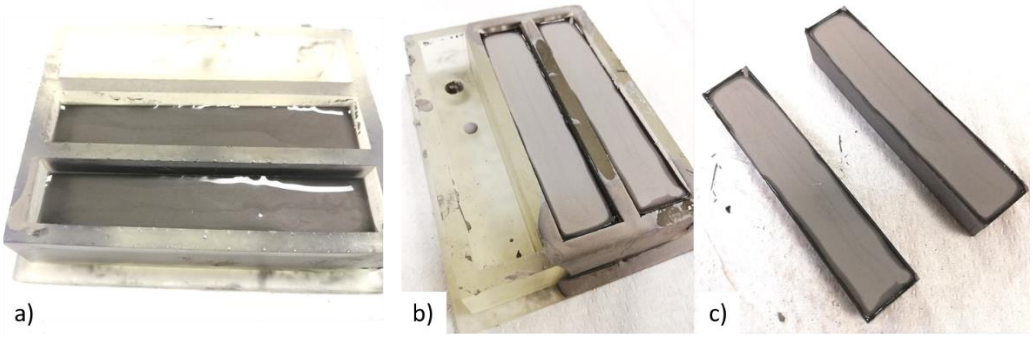

Figure 33: The novel approach of CPTi gel-casting illustrated showing the a) cast slurry, b) the slurry after gelation and c) the demoulded green parts.

4.4.2 Drying

After the green parts were demoulded, they were dried at room temperature and at atmospheric pressure for 12 hours. During drying up to 90% of the solvent, deionized water, is evaporated while the backbone polymers remain in the green part to hold the shape and provide strength to the green body during this initial debinding stage. According to German and Bose (1997), when most of the solvent is removed, the binder in the green body exists mostly in the pendular state (binder saturation below 0.2). This is when particles are held together by lens-shaped rings of liquid and there is mainly air between the particles, as illustrated by Figure 34. The capillary attractive forces from these pendular bonds provides considerable strength (German and Bose, 1997). The backbone polymers burn off during binder burnout.

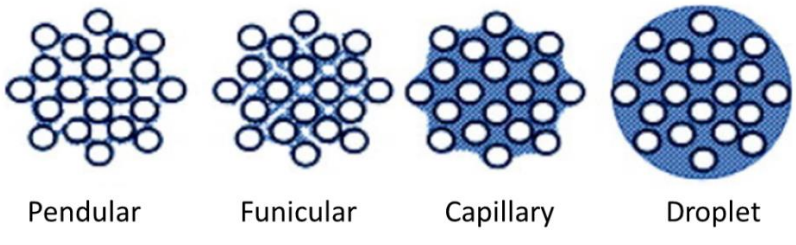

Figure 34: Phases of solid-binder interactions according to the degree of binder (adapted from Sakr et al., 2012)

Figure 35 illustrates the warping of a green body after drying as well as a crack that formed during drying, indicated by the arrow. Warping and cracking are a result of rapid drying of the green part. It is clear that drying is a critical step in the gel-casting process and needs to be controlled to achieve a near-net-shape part that is not distorted or cracked. The drying process can be controlled by drying the green bodies in a drying chamber with controlled atmosphere, controlling the temperature and humidity, which controls the rate of evaporation.

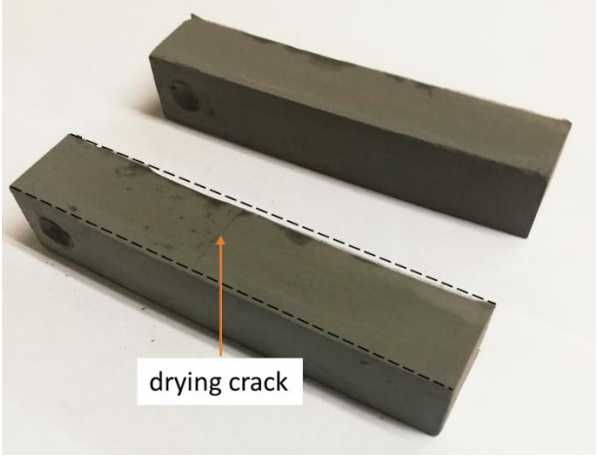

Figure 35: Warping of dried green bodies with the arrow indicating a drying crack

4.4.3 Thermal Gravimetric Analysis (TGA)

TGA in argon atmosphere was performed on two samples. The first sample was a gel-cast titanium part that has undergone binder burnout under argon atmosphere, heating to 380 ˚C at 5 ˚C/min, and holding for 30 min, before heating further to 650 ˚C at the same heating rate and holding for another 30 min. The purpose of TGA on this sample was to investigate whether complete burnout of the binder has taken place. The second sample that was sent for TGA was a dried gel-cast titanium part with a MAM/MBAM binder system. The purpose of this TGA test was to

determine the mass loss profile over temperature for the binder remaining in the part after drying.

A 2.18 % mass loss was observed for the first sample in the temperature range between 104 and 193 ˚C, as seen in Figure 36. This does not correlate to the decomposition temperature of any of the binder constituents and deserves further investigation. It is recommended that C, O and N analysis be performed on the debound samples for future studies. This was not investigated within the scope of this study, as the analysis equipment was not available. The mass gain after 500 ˚C occurred for both the thermally debound and dried samples. This could be due to the titanium reacting with the debound products at higher temperatures. EDS of the microstructures was conducted in order to check for evidence of C or O in the microstructures.

The TGA curve for the dried sample (Figure 37) correlates well with literature as given in Figure 10, section 2.4.4. Four events of mass loss are observed from this curve. A summary of each event is given in Table 8, presenting the onset- and end temperature, mass loss, mass loss as a percentage and the material that burns off.

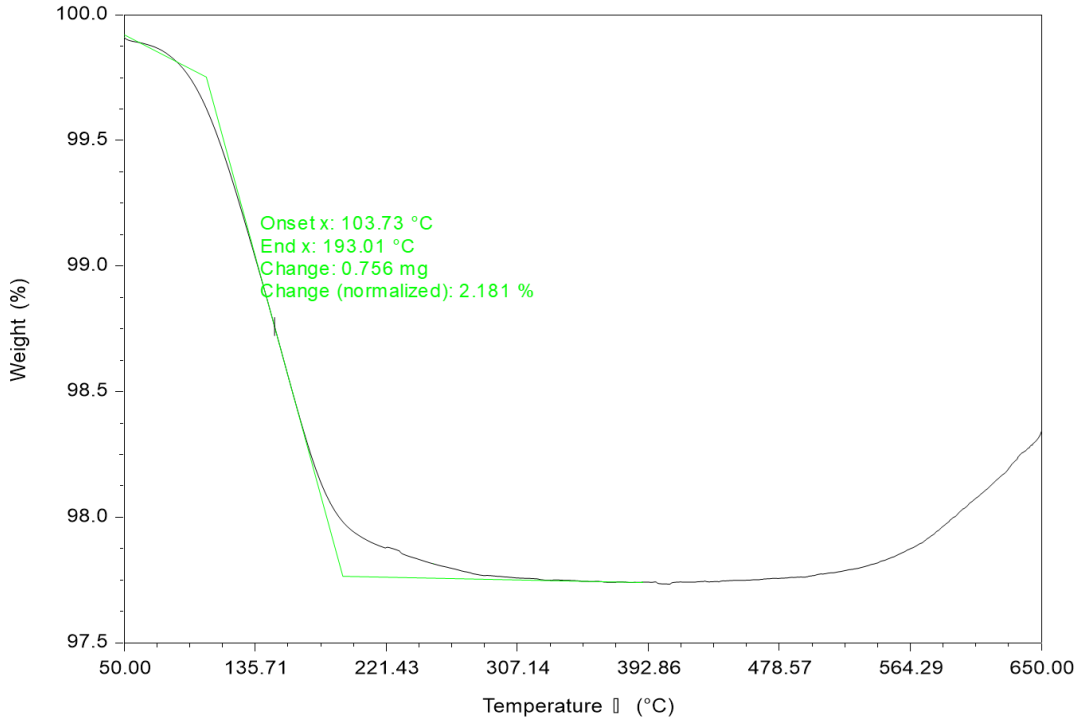

Figure 36: TGA profile of thermally debound CPTi gel-cast part in argon

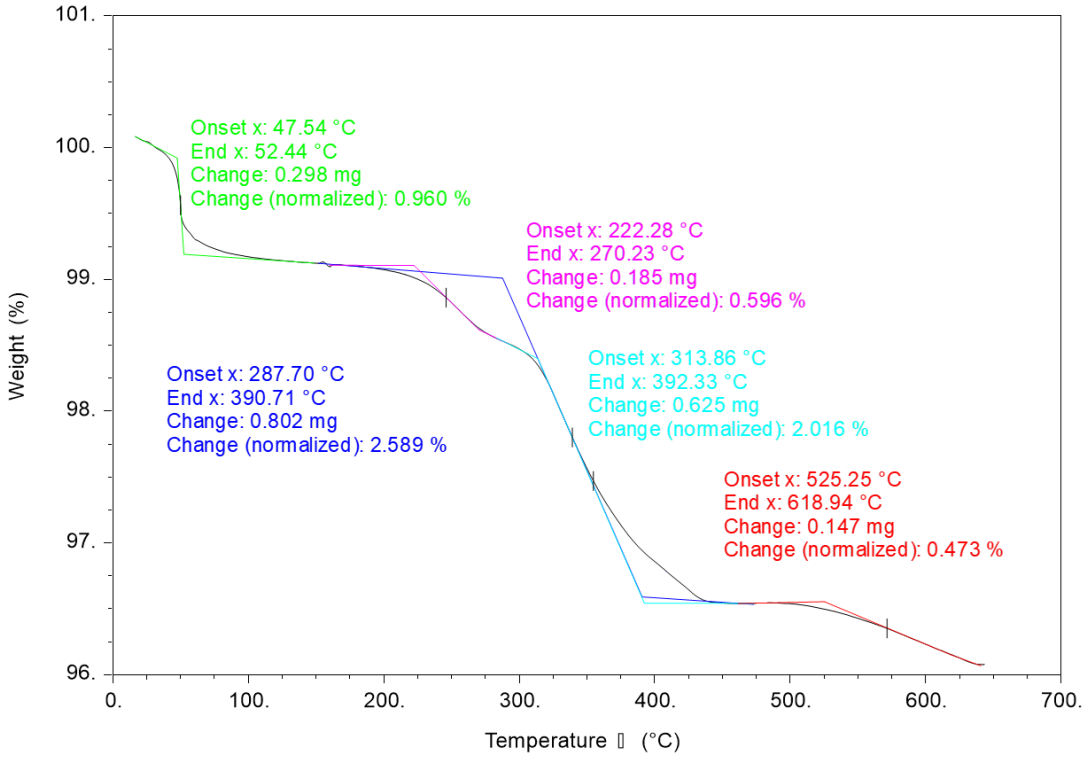

Figure 37: TGA profile of dried CPTi gel-cast part in argon

Table 8: TGA events of dried CPTi gel-cast specimen in argon

Event	Onset Temperature [˚C]	End Temperature [˚C]	Mass Loss		Material
			[mg]	[%]	
1	47.5	52.4	0.298	0.96	NH_4OH
2	222.3	270.2	0.185	0.596	MAM
3	313.9	392.3	0.625	2.016	MAM & MBAM
4	525.3	618.9	0.147	0.473	no correlation to binder formulation

It is observed from the data that most of the binder is burnt off when 400 ˚C is reached. Based on the TGA results, a temperature profile for the binder burnout and pre-sintering of the green parts were developed, as illustrated in Figure 38, highlighting the regions where products debind. The purpose of the TGA was to determine the temperatures where the binder burns off completely. Some of the results did not correlate to the binder formulation and presented areas for further research.

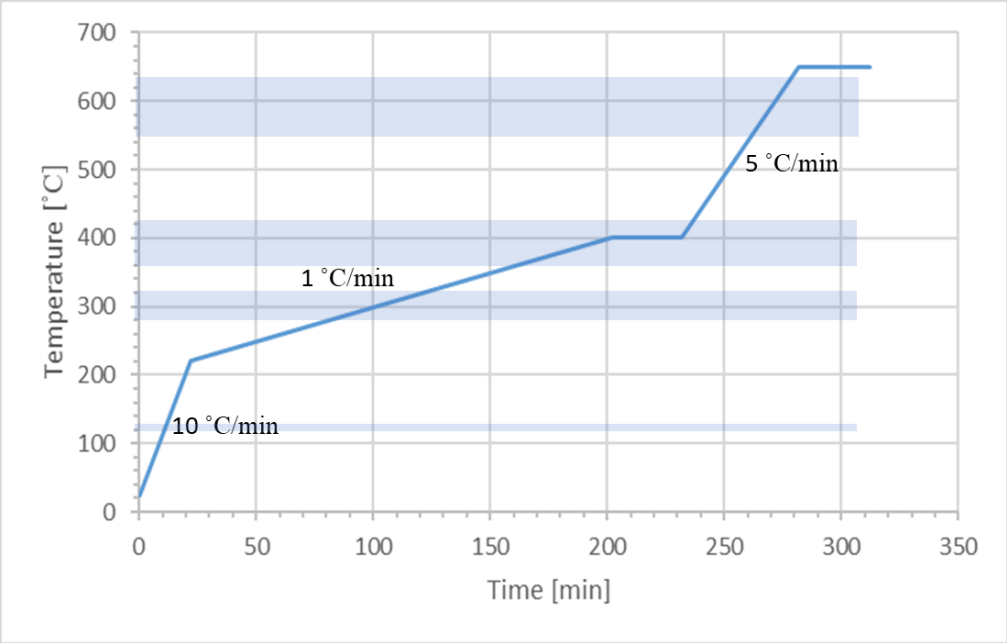

Figure 38: Binder burnout and pre-sintering profile

4.4.4 Binder Burnout and Pre-sintering

Figure 39 shows the samples in the quartz tube on zirconia boats before (left) and after (right) binder burnout. There was only space for two bars in the heating zone of 180 mm. It is also seen from Figure 39 that soot forms on the quartz tube as a result of incomplete burnout of the polymers in the argon atmosphere. A special gas mix of 95 % argon and 5 % hydrogen was tested as the burnout atmosphere. Hydrogen is often used to aid decomposition of polymers during thermal debinding (German, 2003). During this test, the ends of the quartz tube, where the glass connectors connect to the tube, heated to above 60 ˚C; this was not observed when using pure argon. This caused the vacuum tape that was used to seal the connection to melt, compromising the controlled atmosphere required for the process.

The reason for the tube heating up at the ends could be because of steam, which has a high heat capacity, that forms from the hydrogen of the gas that bonds with oxygen from the polymers. Another explanation, and maybe the most obvious one, is that the parts have not been sufficiently dried before binder burnout. The remaining solvent is then removed from the part as it is heated and forms steam in the tube, causing the tube to heat up and the vacuum tape to melt, introducing a leak. This explanation is supported by the fact that this event happened at a temperature just below 200 ˚C, below the temperature where any binder burns off. Clear liquid was found in the tube at this stage and the temperature of the tube at the ends dropped after removing the liquid. This also gives a viable explanation for why some of the samples cracked during binder burnout. Solvent removal by heating causes rapid

evaporation, leading to cracking of the gel-cast part. Figure 40 shows such a crack that formed during binder burnout.

Figure 39: Quartz tube before (left) and after (right) binder burnout

Nitrogen oxide (NOx) gasses were released as a product of MAM and MBAM during polymer burnout. These poisonous gasses were adsorbed by connecting a column with activated carbon (AC) at the outlet of the quartz tube (Figure 41). Glass wool was used to keep the AC in place in the column. The glass wool clogged as it adsorbed the gasses, hindering the argon flow through the system and leading to a build-up in pressure in the tube, which in turn caused the glass connectors of the quartz tube to eject. If pressure is starting to build up in the tube because of clogging, valves on both sides of the tube must be closed (to maintain the argon atmosphere and protect the samples from oxidation) and the glass wool needs to be replaced before opening the valves again.

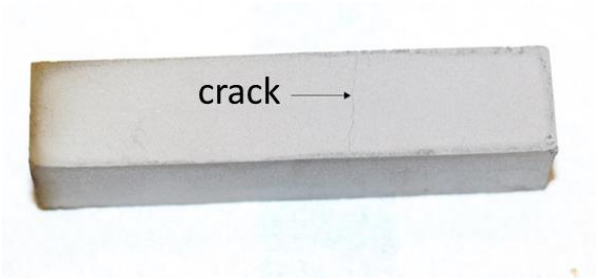

Figure 40: Cracking due to binder burnout stress

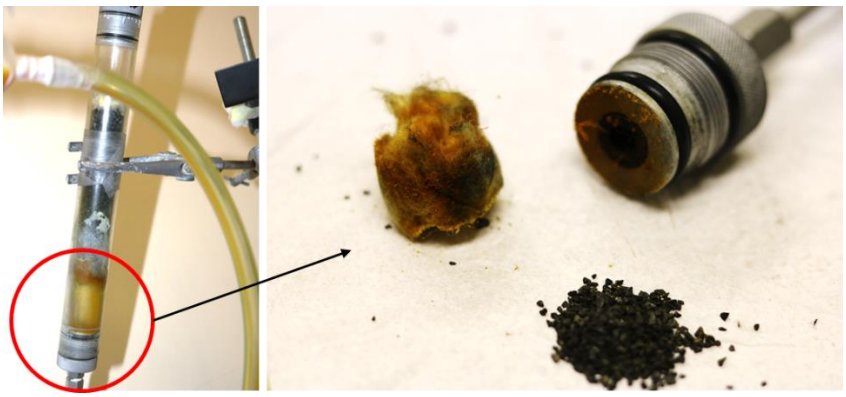

Figure 41: Activated carbon column for NO_x gas adsorption

4.4.5 Sintering

Six titanium gel-cast specimens with a solid loading of 55 vol%, prepared as described in section 3.3.3.1, and which has undergone binder burnout, as described in section 3.3.8, were sintered. The specimens were vacuum sintered at a pressure below 10^{-4} Pa after flushing the system with argon. The same furnace and vacuum system that were used for binder burnout were also used for sintering, but with a different setup, as described in section 3.3.9. The sintering cycle entailed heating to a temperature of 1200 ˚C at a heating rate of 10 ˚C/min. After holding for 2 hours at 1200 ˚C, the specimens were allowed to furnace cool back to room temperature. Argon was allowed to flow through the system once the furnace temperature reached 300 ˚C on the cooling cycle to help with faster cooling of the specimens, as well as cooling of the rotary pump. A maximum of four specimens could be sintered at a time in the alumina tube because of the hot zone of the tube furnace being 180 mm. With an inside tube diameter of 50 mm, two specimens could be fitted in the radial direction and two in the longitudinal direction, thus four specimens in total. The specimens were sintered on zirconia substrates in the tube.

The final sintered specimens (Figure 42a) had no major internal defects visible with the naked eye, indicating a successful casting process. Warping, caused by fast evaporation of solvent during the binder burnout process, was observed of the final sintered specimens (Figure 42b). The specimens showed a good surface finish without any surface pores, which is a significant improvement from a previous study of titanium gel-casting, where the sintered specimens had notable surface pores (Piek, 2017).

The colour observed from the oxide layer, Figure 43, is based on the thickness of the TiO_2 layer. A blue appearance relates to a very thin TiO_2 layer of approximately 40 nm (Pérez Del Pino et al., 2004).

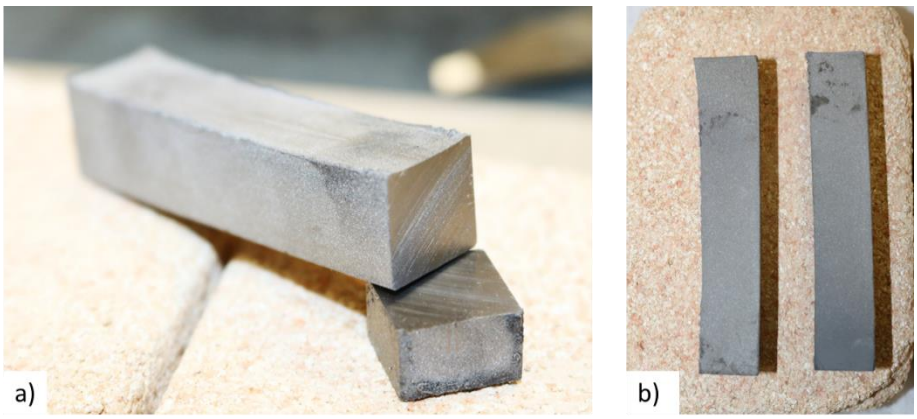

Figure 42: 55 vol% solid loading sintered specimens illustrating (a) cut surfaces and (b) warping

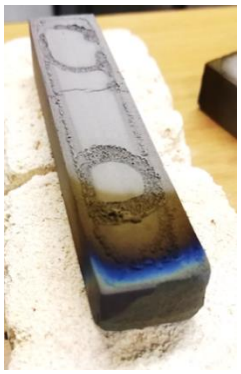

Figure 43: Sintered specimen showing a thin oxide layer

4.4.5.1 Microstructural Analysis

The metallographic preparation of all samples for microstructural analysis of the sintered specimens was conducted according to the method described in section 3.4.3. A uniform distribution of small spherical pores is observed for the 55 vol% solid loading sintered specimens throughout the sample, except for an area very close to the upper edge of the specimen, as seen in Figure 44a. Figure 44 shows the microstructure close to the upper (a) and bottom (b) edge of a sintered specimen. Particles close to the upper edge were not fully sintered due to an uneven distribution of particles. More binder moved towards the surface of the cast slurry as some particles settled towards the bottom, leaving more binder between the particles close to the upper edge during the casting and polymerization process. As a result, the microstructure is more porous at the upper edge after binder burnout and sintering. Figure 44b and Figure 45a show an evenly dense microstructure close to the bottom edge and of the middle section of the specimen, respectively. This illustrates an evenly dense microstructure with well sintered solid material.

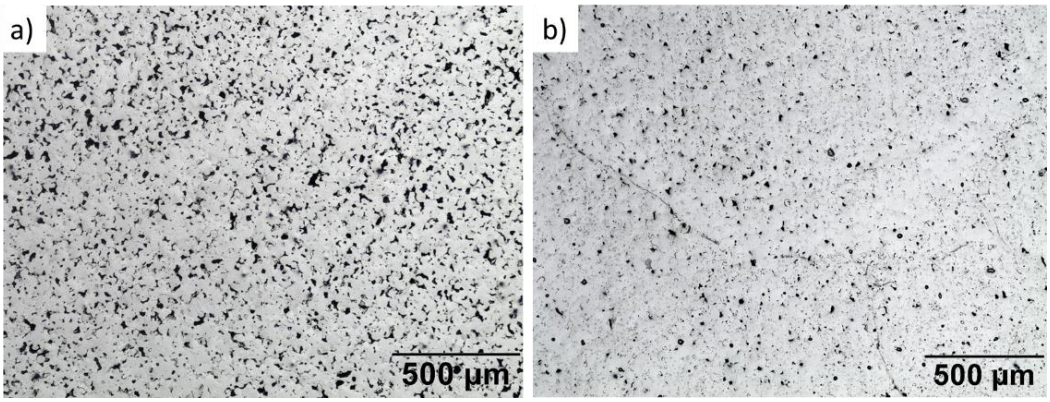

Figure 44: Optical light micrographs (5x) showing the microstructure at (a) the upper edge and (b) near the lower edge of the specimen.

Figure 45a shows a microstructure with an even density, but quite porous, with some internal defects. Figure 45b is a higher magnification micrograph of the middle section, highlighting the internal defects by circling and numbering them. Three of the six sintered specimens showed cracks, which were already present after binder burnout. The crack, indicated by defect 1 (brown), is due to high binder burnout stress. Defect 2 (red) illustrates porosity due to poor packing and defect 3 (blue) highlights porosity due to sintering, where small pores are found between grain boundaries of the particles. Figure 46 shows sinter bonds between particles. Typically, any cracks that are present in the green or debound sample get worse with any further sintering heat treatment. The material to each side of the crack densifies and pulls any poorly bound particles into the denser, sintered material, thus widening the crack (German, 2003). Darker spots were observed in the microstructure, as indicated in Figure 46, which were identified as having a different elemental composition (increased levels of C and O) by EDS analysis.

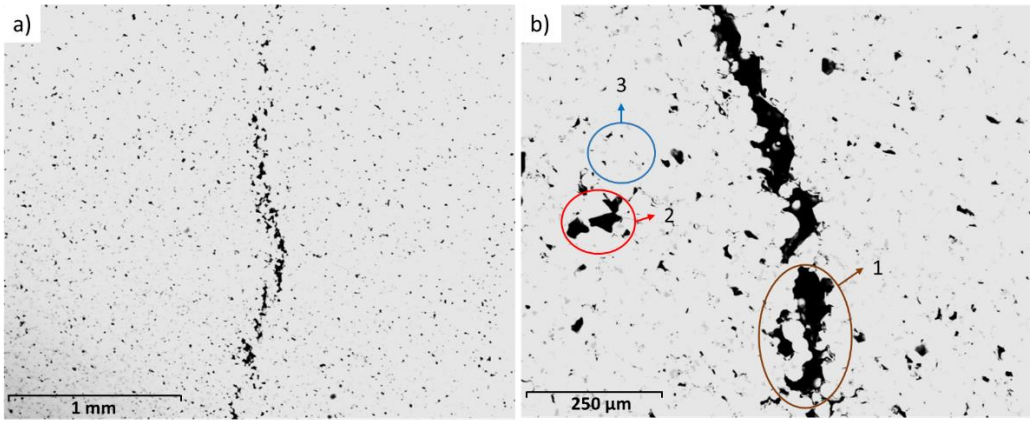

Figure 45: SEM micrographs of the middle section of a specimen showing (a) an evenly dense microstructure and (b) a crack.

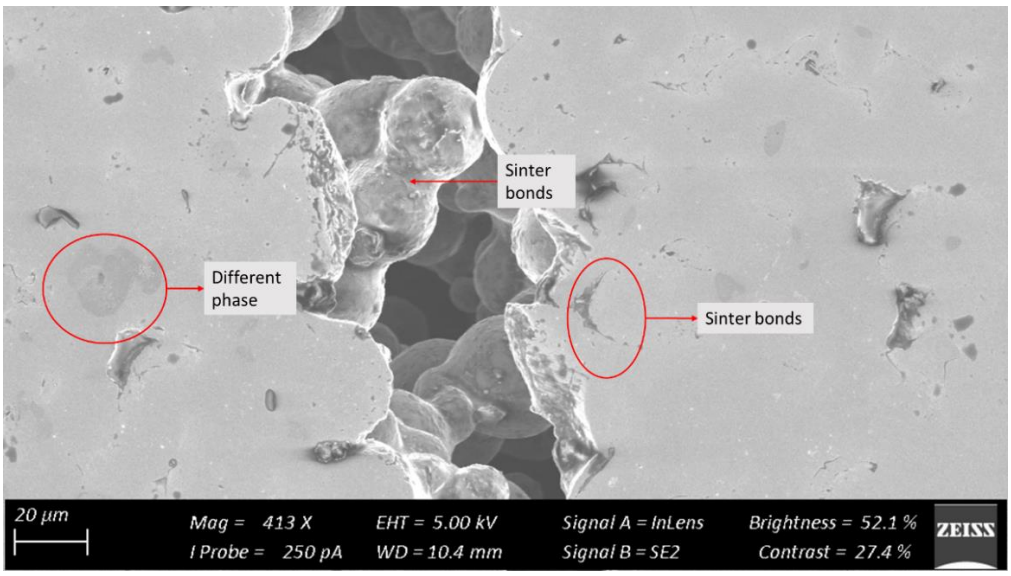

Figure 46: SEM micrograph of a crack showing sinter bonds and the presence of a different phase (increased C and O) than Ti.

4.4.5.2 Elemental Composition Analysis

EDS analysis was performed on a 55 vol% solid loading sintered specimen to determine all the different phases present in the microstructure of a sintered part. A Zeiss Merlin GeminiSEM field emission scanning electron microscope was used to do the analysis. An EDS map scan was done to see if there was any carbon contamination or oxides present in the microstructure. Figure 47 illustrates all the phases present in the sintered microstructure. It is seen that carbon contamination, as well as oxygen, is present in the microstructure. It is further noticed that most of the carbon and oxygen phase occur on the edges of the pores, especially around the crack. Carbon and oxygen react with titanium at elevated temperatures to form TiC and TiO_2, respectively. The presence of carbon and oxygen in the titanium microstructure lead to a brittle material, which is supported by the results of the tensile tests. It is also possible that the presence of carbon around the pores is due to the pores trapping polishing slurry particles.

Figure 48 and Figure 49 show EDS line scans of the sintered specimen close to the edge and in the middle of the specimen, respectively. These graphs confirm that a higher concentration of carbon and oxygen is found around and in the crack. The reason for this observation is that oxygen and carbon, as products from binder burnout, easily spread through the microstructure through surface connected pores. The contamination has most probably occurred in the binder burnout process already. It is also seen from these two figures that a slightly purer titanium microstructure is found in the middle of the specimen than closer to the edge. In the denser part of the microstructure, approximately 87 wt% Ti is seen closer to the edge and ~92 wt% Ti in the middle of the specimen.

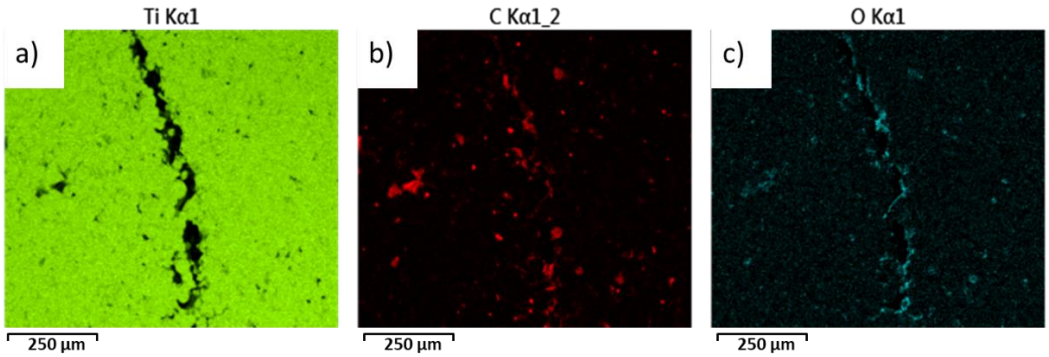

Figure 47: EDS map of SEM image shown in Figure 45(b), showing the elemental distribution of (b) titanium, (c) carbon and (d) oxygen

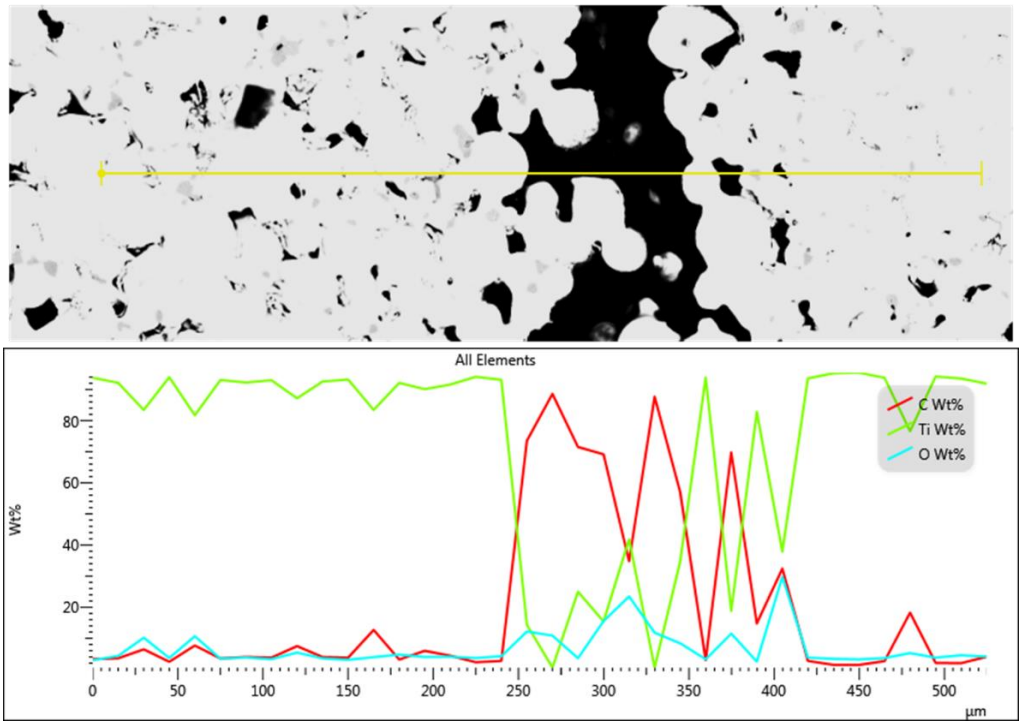

Figure 48: EDS line scan close to the edge of a 55 vol% φ sintered specimen

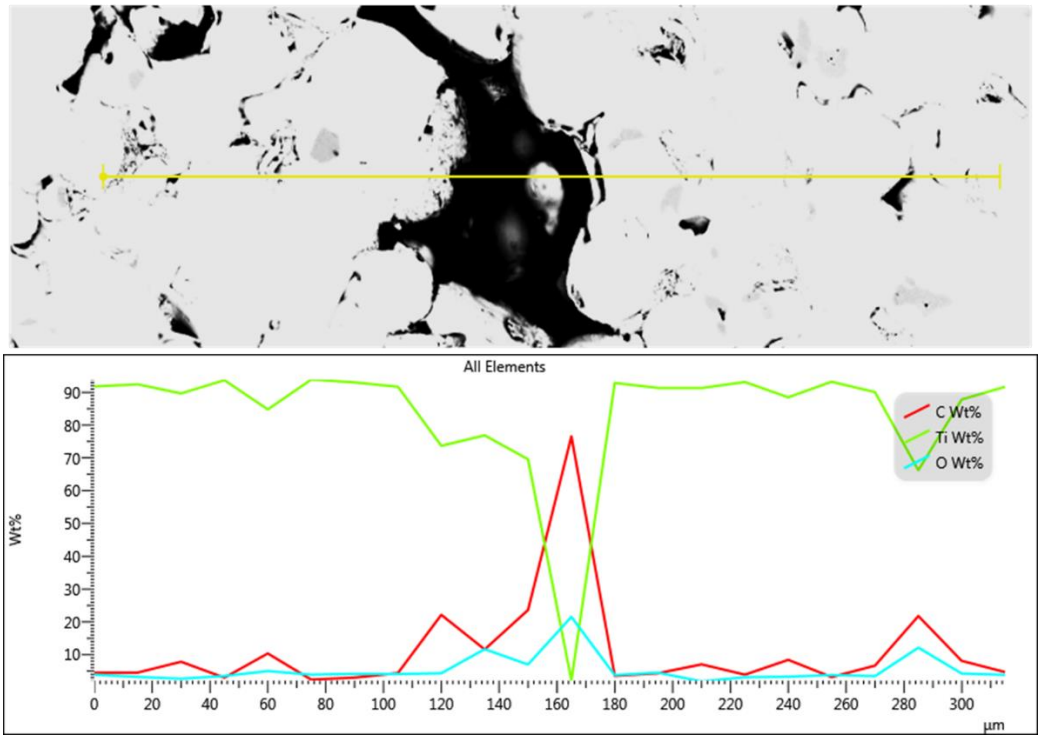

Figure 49: EDS line scan in the middle of a 55 vol% φ sintered specimen

4.5 Density

4.5.1 Green- to Sintered Density

The green density, sintered density, relative density and densification of the 55 vol% solid loading gel-cast parts are given in Table 9. The sintered density was calculated from Archimedes principle. The specimens were impregnated with oil to fill the open pores before calculating the sintered density. The test data for the sintered density is given in Appendix C.2. The density of the water was taken as 0.9986 g/cm^3, based on a table in the ASTM B962 standard, according to the measured temperature of the water, which was 18 ˚C. The reported value for sintered density is the arithmetic mean of the test data. The green density was estimated according to equation 3.3.5, taking the theoretical density of CPTi as 4.51 g/cm^3 and the binder density as 1 g/cm^3. The relative sintered density is taken as the sintered density relative to the theoretical density of CPTi. Densification, ψ, is a parameter that defines the change between the sintered- and green density due to sintering, divided by the change in density needed to obtain a pore-free solid. Densification, adapted from the *Handbook of Mathematical Relations in Particulate Materials Processing* (German, 2009), is calculated as:

$$\psi = \frac{\rho_s - \rho_g}{\rho_{th} - \rho_g}. \qquad (4.5.1)$$

Table 9: Density of 55 vol% φ sintered specimen

	[g/cm^3]	relative %
Green density, ρ_g	2.93	65.0 [2]
Sintered density, ρ_s	3.77	83.6
Densification parameter, ψ	0.53	

The change in porosity from green density to sintered density is 45 vol% to 16.4 vol%, assuming that all binder was burned out. This is an improvement on the relative sintered density from a previous study, where a maximum relative sintered density of 78 % was reached with a 40 vol% φ CPTi gel-cast part (Piek, 2017). A densification of 0.53 indicates that the sintered parts have only densified 53 % of its capacity from green density to full density, as illustrated in Figure 50.

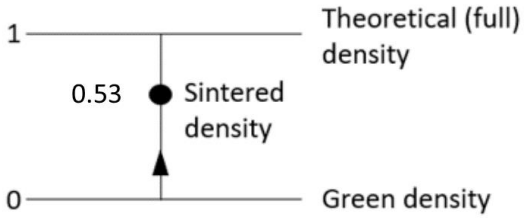

Figure 50: Schematic of densification of a 55 vol% φ part

4.5.2 Shrinkage

The dimensional change that occurred from the cast slurry to the final sintered part was determined by a method adapted from the ASTM B610 standard by taking the arithmetic difference between the dimensions of the mould cavity and the dimensions of the sintered specimen produced from the mould. The dimensional change is expressed as a percent growth of shrinkage. Dimensions were taken with a Vernier caliper with resolution of 0.01 mm. The percent absolute dimensional change (DC) for the specimens were calculated as:

$$DC, \% = \frac{x_s - x_m}{x_m} \times 100 \,, \qquad (4.5.2)$$

where x_s is the dimension of the sintered specimen, in mm, and x_m is the dimension of the mould cavity, also in mm. The dimensions for the mould cavity were 88.7 mm in length and 17.6 mm in width. The dimensional change of the length

[2] The green density includes the density of the binder that fills the pores in the green state and is thus higher than the solid loading value.

and width of the 55 vol% solid loading rectangular gel-cast bar after sintering were calculated and is presented in Table 10. The test data is given in Appendix C.3.

Table 10: Dimensional changes of 55 vol% φ sintered specimen

DC, length	-10.40 %
DC, width	-9.03 %
Y, 90	-15.10 %
Y, 83.6	-13.03 %

The mould was designed on the assumption of isotropic shrinkage (Y), as calculated from the density using equation 3.3.7, assuming a final relative sintered density of 90 %. The isotropic shrinkage, calculated from the relative sintered density reported in section 4.5.1, is 13.03 %. The real dimensional changes in the length and width of the rectangular bar were found to be a shrinkage of 10.40 % and 9.03 %, respectively. Thus, using the isotropic shrinkage relationship to account for shrinkage in mould design is a conservative initial guess, but not fully accurate. Some of the factors that influence the dimensional change is the grade of the powder, particle size distribution, green density, sintering time and temperature as well as heating- and cooling rate. All of these factors were kept constant.

4.6 Mechanical Behaviour

4.6.1 Tensile Properties

Three 55 vol% solid loading sintered titanium bars were machined into tensile specimens according to the drawing given in Appendix D.2. The first two specimens were not machined according to the drawing specifications, resulting in a 10 mm longer gauge length section.

Figure 51 shows the stress-strain curves for the three specimens tested. Considering the results for specimens 1 and 2, it appears that the extended gauge length of these specimens influences the measurement. However, a recent study on the effect of specimen geometry on tensile properties of titanium alloy metal sheet found that the change in gauge length or gauge area did not influence the yield strength and did not have a significant influence on the ultimate tensile strength (Masete et al., 2018). Both of these samples failed very close to yielding, indicating that a difference in the microstructure between the three specimens could explain the different curves. The only reliable result that should therefore be considered is that of specimen 3. The yield strength (offset = 0.2 %), ultimate tensile strength, modulus of elasticity and elongation at fracture of specimen 3 are given in Table 11. The strain was derived from the crosshead displacement and the original gauge length.

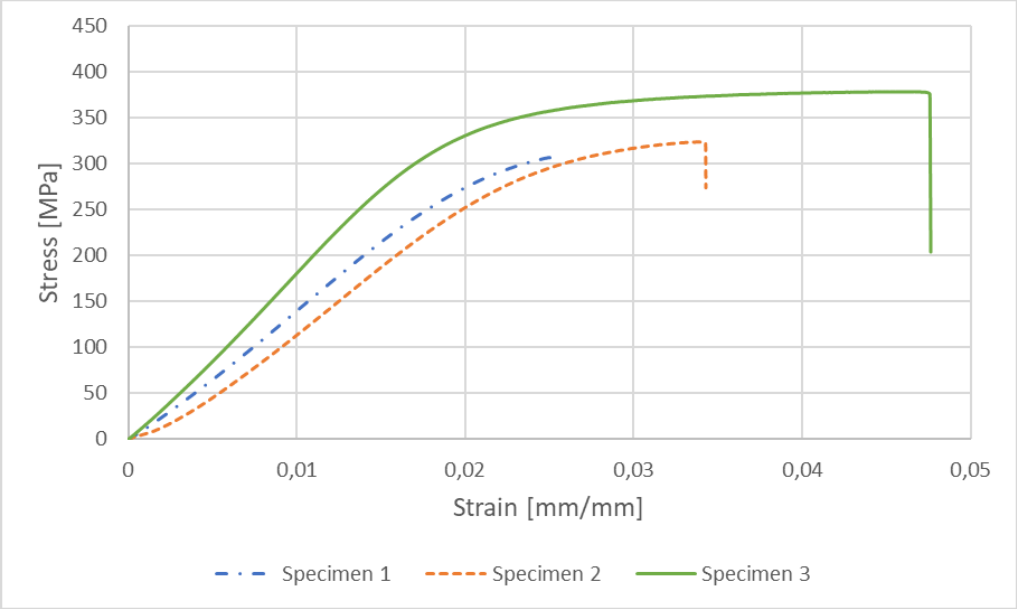

Figure 51: Stress-strain curves for the machined tensile test specimens

Table 11: Tensile properties of specimen 3

Tensile Property	Measured	ASTM B988, Grade 1 PM100
Yield Strength, YS	323 MPa	138 MPa
Ultimate Tensile Strength, UTS	378 MPa	240 MPa
Modulus of Elasticity, E	18.8 GPa	-
Elongation at fracture, ε_f	4.76 %	24 %

From Table 11 it is seen that the YS and UTS measured are higher than the values for PM products from the ASTM B988 standard. The reason for this observation is the presence of C and O in the microstructure. C and O contamination of the microstructure causes brittle fracture and thus explains the lower elongation at fracture measured, compared to the value specified in the standard.

A microscopic observation of the fractured surface is that the material has not formed a densified structure and that distinct particles are still visible, as seen in Figure 52a. The tensile properties tested is thus more related to the strength of the sinter bonds than the material properties. Only intermediate sintering has taken place. This is evidenced by the irregular shape of the pores and distinct particles seen in Figure 52b. Sintering occurs in three stages, as illustrated in Figure 11, beginning with initial sinter bonds where no shrinkage takes place, then densification start to take place when intermediate sinter bonds form, resulting in irregularly shaped pores. Final sintered bonds are characterized by spherical pores

between the grain boundaries as a result of densification. It is recommended that the sintering temperature and holding time be increased for future studies.

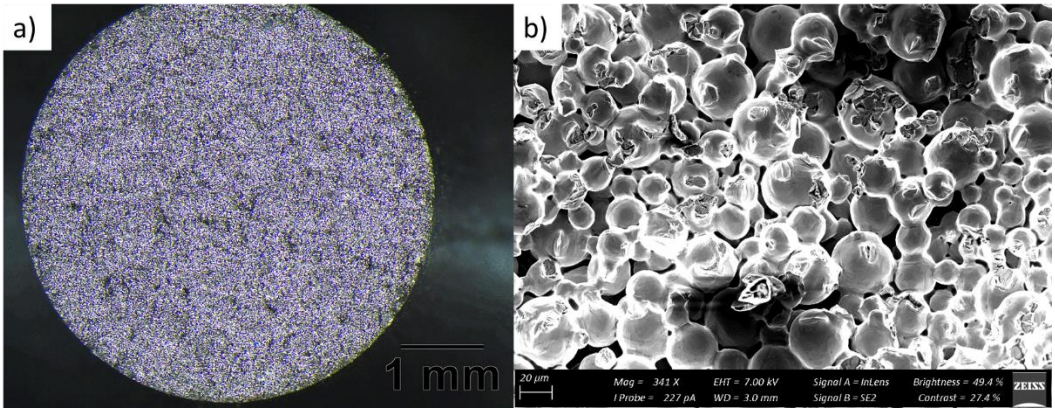

Figure 52: Optical (a) and SEM (b) micrographs of the fractured tensile specimen surface

4.6.2 Hardness

The results obtained from the Rockwell apparent hardness test is shown in Table 12. Three specimens were tested: two specimens with five indentations each on the xz-plane and one specimen with seven indentations on the xy-plane. The locations of the indentations are illustrated in Figure 53.

The machine was calibrated with a calibration block with hardness value of 82.22 HRBW. An average of 82.5 HRBW with a range of 0.5 was tested with three indentations on the calibration block and it was thus found that the machine is well within specification. The hardness of wrought grade 1 CPTi is 70 HRBW. An arithmetic mean hardness value of 60.1 HRBW was determined for the 55 vol% φ sintered specimens, which is a value 86 % of wrought. For specimens 1 and 2, indentations 1 and 2 were made at the upper edge of the specimens, indentations 3 and 4 at the bottom edge and indentation 5 in the middle of the specimen. It is observed that the hardness value does not vary significantly throughout the thickness of the specimens from the upper to the lower edge, indicating an evenly dense microstructure and that no significant settling of the powder has taken place after casting the slurry. For specimen 3, it is observed that the hardness values varied slightly with the y-direction.

Table 12:Rockwell Hardness Values

Specimen	HRBW Value								
	1	2	3	4	5	6	7	Average	
1	61.6	63.9	61.3	61.5	62.2			62.1	
2	61	59.2	60.7	61.2	59.6			60.3	60.1
3	56.2	60.6	59.3	56.4	57	57.3	57.2	57.7	

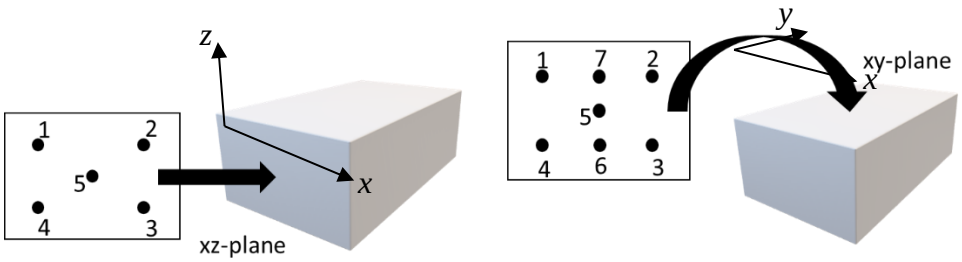

Figure 53: Locations of the indentations on the xz-plane (left) and the xy-plane (right)

5 Conclusions and Recommendations

The MAM/MBAM and Isobam® binder systems were evaluated by sedimentation tests, investigating the settling time of CPTi powder in various premix solutions. The monomer content, monomer:crosslinker ratios, dispersant content, slurry mixing time and solid loading were varied. It was clear that neither the MAM/MBAM nor the Isobam® binder system suspends the CPTi powder particles.

A commercially pure titanium slurry, using the MAM/MBAM binder system, was successfully developed, using a novel approach to the conventional ceramic gel-casting process. It was found that for CPTi powder, the weight of the powder particles plays a more significant role than the surface charge of the particles in the dispersion of the particles in the suspension. Stokes Law was used to control the rate of sedimentation of the particles, leading to a slurry with a solid loading of 55 vol% that was successfully cast and polymerized, without settling of the powder particles during the process.

A rectangular bar-shape mould was successfully resin printed, using stereolithography. The mould rendered parts with a smooth surface finish that easily demoulded. The mould cavity was designed, assuming isotropic shrinkage of 15.1 % (from green density to a relative sintered density of 90 %). The shrinkage measured was 10.4 % and 9.03 % in the length and width of the sintered rectangular bars, respectively. A dimensional accuracy of 0.3 mm from mould to final net-shape part was thus not reached and would require further study on the characterization of shrinkage together with an iterative approach of mould design. Casting simulation software, such as Altair Inspire Cast, is recommended for use in further studies. The objective of gel-casting a complex shape was not achieved and is also recommended for further study, using the simulation software recommended.

Some of the green bodies warped and cracked due to rapid evaporation of the solvent during drying and the beginning of the binder burnout cycle. It is recommended that a controlled atmosphere is used for solvent removal for further studies. As a result of insufficient drying, a clear liquid was removed from the quartz tube during debinding that caused the ends of the tube to heat up as steam formed, melting the vacuum tape that sealed the connections and compromising the system. TGA was done to determine the temperatures at which the binder constituents debind. The binder was debound at 400 ˚C and the parts were presintered at 650 ˚C to obtain handling strength. The debound and presintered parts were vacuum sintered at 1200 ˚C for 2 hours. A relative sintered density of 83.6 % was achieved.

Optical micrographs of the sectioned sintered specimens showed an even distribution of pores, indicating a well-dispersed slurry during the casting and polymerization process. SEM images of the fractured surface of a tensile test specimen showed distinct particles indicating that only intermediate sintering has

taken place. A yield strength and ultimate tensile strength of 323 MPa and 378 MPa, respectively, was measured. This is much higher than the standard for PM100 CPTi grade 1. The elongation at fracture measured was also much lower than the standard. The tensile properties were explained by C and O detected in the microstructure by EDS analysis. Hardness values 86 % of wrought was measured.

References

ASM Material Data Sheet [WWW Document], n.d. URL http://asm.matweb.com/search/SpecificMaterial.asp?bassnum=mtu010 (accessed 10.4.19).

ASTM International, 2010. Standard Test Method for Particle Size Distribution of Refractory Metal Powders and Related Compounds by Light Scattering, ASTM B822, West Conshohocken, PA.

Barreiros, F.M., Martins, G., Matos, M., Mascarenhas, J., Vieira, M.-T., 2008. Preparing MIM Feedstocks for Bio-Applications Using an Agar-Based Binder. Mater. Sci. Forum - MATER SCI FORUM 587–588, 385–389.

Black, J., Kohser, R.A., 2008. DeGarmo's Materials Processes Manufacturing 10th, 10th ed. John Wiley & Sons, Inc, Hoboken, NJ.

Boeing Company - Boeing Forecasts $8.7 Trillion Aerospace and Defense Market through 2028 [WWW Document], n.d. URL https://investors.boeing.com/investors/investor-news/press-release-details/2019/Boeing-Forecasts-87-Trillion-Aerospace-and-Defense-Market-through-2028/default.aspx (accessed 10.15.19).

Bottino, M.C., Coelho, P.G., Henriques, V.A.R., Higa, O.Z., Bressiani, A.H.A., Bressiani, J.C., 2009. Processing, characterization, and in vitro/in vivo evaluations of powder metallurgy processed Ti-13Nb-13Zr alloys. J. Biomed. Mater. Res. - Part A 88, 689–696.

Brandon, D.G., Kaplan, W.D., 2008. Microstructural characterization of materials. John Wiley.

Brust, S., Röttger, A., Theisen, W., 2016. High-temperature stability and interfacial reactions of Ti and TiN thin films on Al2O3 and ZrO2. Surf. Coatings Technol. 307, 47–55.

Cai, K., Frant, M., Bossert, J., Hildebrand, G., Liefeith, K., Jandt, K.D., 2006. Surface functionalized titanium thin films: Zeta-potential, protein adsorption and cell proliferation. Colloids Surfaces B Biointerfaces 50, 1–8.

Chang, I., Zhao, Y., 2013. Advances in powder metallurgy : properties, processing and applications. Woodhead Publishing.

Chopra, K., Mummery, P.M., Derby, B., Gough, J.E., 2012. Gel-cast glass-ceramic tissue scaffolds of controlled architecture produced via stereolithography of moulds. Biofabrication 4.

Cui, C., Hu, B.M., Zhao, L., Liu, S., 2011. Titanium alloy production technology, market prospects and industry development. Mater. Des. 32, 1684–1691.

Delft, T., n.d. Particle Size Distribution (PSD) [WWW Document]. URL https://www.tudelft.nl/citg/over-faculteit/afdelingen/watermanagement/research/waterlab/equipment/particle-size-distribution-psd/

Duan, B.-H., Hong, H.-X., Wang, D.-Z., Liu, H.-J., Dong, X.-J., Liang, D.-D., 2014. Porous nickel-titanium alloy prepared by gel-casting. Rare Met. 33, 394–399.

Ebel, T., 2019. PMTi2019: International conference on the PM and AM of titanium highlights a bright future for sinter-based technologies. Powder Inject. Mould. Int. 13, 61–74.

Erasmus, W., 2018. Slurry vibration of gel-cast titanium. University of Stellenbosch.

Fahlman, B.D., 2010. MATERIALS CHEMISTRY. SPRINGER.

Froes, F.H., 2012. Titanium Powder Technology: A Review - Part 2. Adv. Mater. Process. 170.

Froes, F.H., 2013. Titanium PM: Developments and opportunities in a sector poised for growth. Powder Metall. Rev. 2, 29–43.

Froes, F.H., Mashl, S.J., Moxson, V.S., Hebeisen, J.C., Duz, V.A., 2004. The technologies of titanium powder metallurgy. JOM 56, 46–48.

GE Additive Powders | GE Additive [WWW Document], n.d. URL https://www.ge.com/additive/additive-manufacturing/powders (accessed 11.20.19).

German, R., 2009. Handbook of Mathematical Relations in Particulate Materials Processing. John Wiley & Sons, Inc, Hoboken, NJ.

German, R.M., 1996. Sintering Theory and Practice. John Wiley & Sons, Inc, New York.

German, R.M., 2003. Powder Injection Molding - Design and Application. Innovative Material Solutions, Inc., Pennsylvania.

German, R.M., 2005. Powder metallurgy and particulate materials processing : the processes, materials, products, properties and applications.

German, R.M., Bose, A., 1997. Injection molding of metals and ceramics. Metal Powder Industries Federation.

Goso, X., Kale, A., 2010. PRODUCTION OF TITANIUM METAL POWDER BY THE HDH PROCESS. In: Light Metals Conference. Pyrometallurgy division, Mintek, Johannesburg, pp. 292–305.

Groover, M.P., 2013. Principles of Modern Manufacturing, Fifth. ed. John Wiley & Sons, Ltd, Singapore.

Guo, D., Cai, K., Li, L., Nan, C., Gui, Z., n.d. Gelcasting of PZT.

Harrysson, O.L.A., Cansizoglu, O., Marcellin-Little, D.J., Cormier, D.R., West, H.A., 2008. Direct metal fabrication of titanium implants with tailored materials and mechanical properties using electron beam melting technology. Mater. Sci. Eng. C 28, 366–373.

Inagaki, M., Kang, F., 2016. Materials science and engineering of carbon : characterization. Butterworth-Heinemann : Academic Press.

Ivanov, E., Del-Rio, E., Kapchenko, I., Nyström, M., Kotila, J., 2018. Development of bio-compatible beta ti alloy powders for additive manufacturing for application in patient-specific orthopedic implants. In: Key Engineering Materials. Trans Tech Publications Ltd, pp. 9–17.

Janney, M.A., Omatete, O.O., Walls, C.A., Nunn, S.D., Ogle, R.J., Westmoreland, G., 1998. Development of Low-Toxicity Gelcasting Systems. J. Am. Ceram. Soc. 81, 581–591.

Jee, C.S.Y., Guo, Z.X., Stoliarov, S.I., Nyden, M.R., 2006. Experimental and molecular dynamics studies of the thermal decomposition of a polyisobutylene binder.

Kennedy, A.R., Lin, X., 2011. Preparation and characterisation of metal powder slurries for use as precursors for metal foams made by gel casting. Powder Metall. 54, 376–381.

Kurtz, S., Ong, K., Lau, E., Mowat, F., Halpern, M., 2007. Projections of primary and revision hip and knee arthroplasty in the United States from 2005 to 2030. J. Bone Jt. Surg. - Ser. A 89, 780–785.

Labropoulos, K.C., Niesz, D.E., Danforth, S.C., Kevrekidis, P.G., 2002. Dynamic rheology of agar gels: Theory and experiments. Part II: Gelation behavior of agar sols and fitting of a theoretical rheological model. Carbohydr. Polym. 50, 407–415.

Li, Y., Guo, Z.M., Hao, J.J., Ren, S.B., 2008. Gelcasting of porous titanium implants. Powder Metall. 51, 231–236.

Liu, K., Zhang, K., Bourell, D.L., Chen, F., Sun, H., Shi, Y., Wang, J., He, M., Chen, J., 2018. Gelcasting of zirconia-based all-ceramic teeth combined with

stereolithography. Ceram. Int. 44, 21556–21563.

Long, M., Rack, H.J., 1998. Titanium alloys in total joint replacement - A materials science perspective. Biomaterials.

Lu, Z.L., Cao, J.W., Bai, S.Z., Wang, M.Y., Li, D.C., 2015. Microstructure and mechanical properties of TiAl-based composites prepared by Stereolithography and gelcasting technologies. J. Alloys Compd. 633, 280–287.

Machio, C.N., Machaka, R., Motsai, T.M., Chikosha, S., Rossouw, P., n.d. PRODUCTION OF SPHERICAL TITANIUM BASED POWDERS FROM POWDER METALLURGY BARS.

Masete, M.S., Muchavi, N.S., Chikosha, S., Za, S.C., 2018. The effect of specimen geometry on tensile properties of titanium alloy metal sheet. Mater. Sci. Eng. 430.

Mendes, M.W.D., Ágreda, C.G., Bressiani, A.H.A., Bressiani, J.C., 2016. A new titanium based alloy Ti-27Nb-13Zr produced by powder metallurgy with biomimetic coating for use as a biomaterial. Mater. Sci. Eng. C 63, 671–677.

Mutombo, K., 2018. Research and Development of Ti and Ti alloys: Past, present and future 430, 12007.

Neikov, O.D., Naboychenko, S.S., Murashova, I. V, Gopienko, V.G., Frishberg, I. V, Lotsko, D. V, 2009. Handbook of Non-Ferrous Metal Powders - Technologies and Applications. Elsevier.

Nelson, R.D., 1988. Dispersing powders in liquids, Handbook of powder technology ; volume 7. Elsevier, Amsterdam.

Norsk Titanium | Media [WWW Document], n.d. URL https://www.norsktitanium.com/media#featuredArticles (accessed 10.22.19).

Ohkawa, S., Ishii, K., Uo, M., Sugawara, T., Watari, F., 2004. Slip Casting of Titanium Powder for Dental Prosthetic Appliances 45, 1132–1139.

Omatete, O.O., Janney, M.A., Nunn, S.D., 1997. Gelcasting: From Laboratory Development Toward Industrial Production, Europrun Cwtmtic SocRf~. Elsevier Science Limited.

Particle Sciences, 2012. An Overview of the Zeta Potential. Part. Sci. 2, 1–4.

Pérez Del Pino, A., Fernández-Pradas, J.M., Serra, P., Morenza, J.L., 2004. Coloring of titanium through laser oxidation: comparative study with anodizing. Surf. Coat. Technol. 187, 106–112.

Piek, J., 2017. Mechanical Behaviour of Gel-cast Titanium. BEng Mechanical Project Report. University of Stellenbosch.

Piemme, J., 2018. Metal Injection Molding for Implantable Device Applications. Int. J. Powder Metall. 54, 21–24.

Pollinger, J.P., Khalfalla, Y.E., Benyounis, K.Y., 2016. Gel Casting. Ref. Modul. Mater. Sci. Mater. Eng.

Praxis Technology Inc [WWW Document], n.d. URL https://praxisti.com/about-us/ (accessed 10.17.19).

Qian, M., Sam Froes, F.H., 2015. Titanium powder metallurgy: Science, technology and applications, Titanium Powder Metallurgy: Science, Technology and Applications. Elsevier Inc.

Riekert, A., 2019. Gel-casting of Powder Metals. University of Stellenbosch.

Rogovina, L.., Vasil'ev, V.., Braudo, E.., 2008. Definition of the Concept of Polymer Gel. Polym. Sci. 50, 85–92.

Sakr, W.F., Ibrahim, M.A., Alanazi, F.K., Sakr, A.A., 2012. Upgrading wet granulation monitoring from hand squeeze test to mixing torque rheometry. Saudi Pharm. J.

Semlitsch, M.F., Weber, H., Streicher, R.M., Schön, R., 1992. Joint replacement components made of hot-forged and surface-treated Ti-6Al-7Nb alloy. Biomaterials 13, 781–788.

Sidambe, A.T., Figueroa, I.A., Hamilton, H.G.C., Todd, I., 2012. Metal injection moulding of CP-Ti components for biomedical applications. J. Mater. Process. Tech. 212, 1591–1597.

Smithells, C.J. (Colin J., Gale, W.F. (William F., Totemeier, T.C. (Terry C.., 2004. Smithells metals reference book. Elsevier Butterworth-Heinemann.

Synertech - Powder metal parts manufacturer [WWW Document], n.d. URL https://www.synertechpm.com/ (accessed 10.17.19).

Tallon, C., Franks, G. V., 2011. Recent trends in shape forming from colloidal processing: A review. J. Ceram. Soc. Japan 119, 147–160.

Taniguchi, N., Fujibayashi, S., Takemoto, M., Sasaki, K., Otsuki, B., Nakamura, T., Matsushita, T., Kokubo, T., Matsuda, S., 2016. Effect of pore size on bone ingrowth into porous titanium implants fabricated by additive manufacturing: An in vivo experiment. Mater. Sci. Eng. C 59, 690–701.

Taylor, B., Weidmann, E., 2016. Metallographic preparation of titanium [WWW

Document]. Struerrs. URL https://www.struers.com/en/Search?q=metallography+preparation+of+titanium+niobium+ (accessed 11.12.19).

Titanium Powder Produced with the NexGen™ Plasma Atomization System; Significant CAPEX and OPEX Reductions TSX Venture Exchange:PYR [WWW Document], n.d. URL https://www.globenewswire.com/news-release/2019/04/11/1802741/0/en/Titanium-Powder-Produced-with-the-NexGen-Plasma-Atomization-System-Significant-CAPEX-and-OPEX-Reductions.html (accessed 10.22.19).

Titanium Powders | CP Ti and Ti 6A/4V | Reading Alloys [WWW Document], n.d. URL https://www.readingalloys.com/products/titanium-powders?utm_source=https://www.google.com/&utm_medium=undefined (accessed 11.20.19).

Titanium USA 2018, 2018. . In: 34th ITA Annual Conference Proceedings.

Traini, T., Mangano, C., Sammons, R.L., Mangano, F., Macchi, A., Piattelli, A., 2008. Direct laser metal sintering as a new approach to fabrication of an isoelastic functionally graded material for manufacture of porous titanium dental implants. Dent. Mater. 24, 1525–1533.

Wang, F., Jiang, K., Xu, X., 2009. Gel Casting of 316L Stainless Steel Powder Through Mold DIS Process. Tsinghua Sci. Technol. 14, 216–222.

Yang, D., Shao, H., Guo, Z., Lin, T., Fan, L., 2011. Preparation and properties of biomedical porous titanium alloys by gelcasting. Biomed. Mater. 6, 045010.

Yang, Y., Shimai, S., Wang, S., 2013. Room-temperature gelcasting of alumina with a water-soluble copolymer. J. Mater. Res. 28, 1512–1516.

Zhao, D., Chang, K., Ebel, T., Qian, M., Willumeit, R., Yan, M., Pyczak, F., 2013. Microstructure and mechanical behavior of metal injection molded Ti-Nb binary alloys as biomedical material. J. Mech. Behav. Biomed. Mater. 28, 171–182.

Appendix A : Technical Data Sheets

A.1 Commercially Pure Titanium

AP&C
A GE Additive Company

3765 La Vérendrye, suite 110, Boisbriand, Quebec, Canada, J7H 1R8
Tel. (+1) 450.434-1004; Fax: (+1) 450-434-1200
www.advancedpowders.com

F-062 Rev.1

MATERIAL CERTIFICATE No: MC-19-0337

Customer:	Stellebosch University. Meganiese en Bedryfsingenieurs, Banhoecweg, Stellenbosch 7600, South Africa		
Purchase Order:	65925	**Internal Order:**	GEA4274 Rev.3
Material Description:	CPTi powder	**Powder lot #:**	191-C0007
Size:	15-45 µm	**Laboratory No:**	19-0082; 19-0082-A; 19-0831
Specification:	ASTM B348 grade 1	**Quantity:**	5 kg

CHEMICAL COMPOSITION (weight percent)

Element	ASTM B348 gr 1	Measured	Testing method	Status
Carbon, max.	0.08	0.01	ASTM E1941	Conforming
Oxygen, max.	0.18	0.08	ASTM E1409	Conforming
Nitrogen, max.	0.03	0.01	ASTM E1409	Conforming
Hydrogen, max.	0.015	0.002	ASTM E1447	Conforming
Iron, max.	0.20	0.03	ASTM E2371	Conforming
Other each, max.	0.1	< 0.1	ASTM E2371	Conforming
Other total, max.	0.4	< 0.4	ASTM E2371	Conforming
Titanium	Balance	Balance		

Chemical analysis laboratory: Luvak Inc. (722 Main Street, P.O. Box 597, Boylston MA, 01505). Report 0-67214

POWDER CHARACTERIZATION

Description	Required	Measured	Status / Comments
Particle size distribution per ASTM B214			
Particle Size (µm)	**% By Mass**	**% By Mass**	
> 45	Report	1.7	NA
≤ 45	Report	98.3	NA
Particle size distribution per ASTM B822 (Coulter® LS Particle Size Analyzer)			
D_{10}	Report	17 µm	NA
D_{50}	Report	33 µm	NA
D_{90}	Report	45 µm	NA
< 15 µm	Report	6 % by volume	NA
Flow Rate per ASTM B213			
Flow Rate (sec. for 50 g)	Report	29	NA
Apparent Density per ASTM B212			
Apparent Density (g/cm³)	Report	2.60	NA

Analyses were done by AP&C at their location and reported results are rounded following ASTM E29.

We hereby certify that the above values conform to the requirements of Purchase Order 5925.

2019-04-03
Date

Catherine Lavoie
Digitally signed by Catherine Lavoie
Date: 2019-04-03 10:55-04:00
Quality department

Figure A.1: Commercially pure titanium material certificate

Appendix B : Step-by-Step Experimental Procedures

B.1 Binder Burnout and Presintering

The residual binder in the CPTi gel-cast green bodies, after drying, were decomposed by a heat treatment cycle under inert atmosphere that was designed from TGA results. Table B.1 lists the apparatus, laboratory supplies and chemicals that were used.

Table B.1: Apparatus, laboratory supplies and chemicals for binder burnout

Apparatus	Laboratory Supplies	Chemicals
• Quartz tube • Zirconia substrates • Tube furnace • Glass fittings • Bubble flowmeter • Glass column • Water bubbler	• Plastic tubing • Parafilm vacuum tape • Vacuum grease	• Activated carbon • Argon, high purity, 99.998 % • Acetone, 99 %

The following step-by-step procedure for binder burnout was performed:

Step 1: Experiment setup

- The samples were placed in the quartz tube on zirconia boats in the heating zone of the tube furnace.
- The quartz tube was placed in the tube furnace with the samples in the heating zone range.
- The plastic tubing was connected to the glass fittings and sealed with parafilm vacuum tape.
- The glass fittings were connected to the quartz tube and sealed with vacuum grease and parafilm.
- A bubble flowmeter was connected to the system on the inlet side of the quartz tube.
- The quartz tube on the outlet side was connected to a water bubbler and the bubbler to a glass column containing activated carbon.

Step 2: Running the furnace

- The tube furnace was heated to 220 ˚C at a heating rate of 10 ˚C/min, then further heated to 400 ˚C at a heating rate of 1 ˚C/min, dwelling for 30 min at the set temperature.

- The argon cylinder was opened, setting the line pressure to 50 kPa
- When the furnace reached 220 ˚C, the argon flow rate was set to 200 ml/min using the volumetric (bubble) flow meter to read the flow rate and the regulating valve at the inlet of the tube to regulate flow. The flow meter was parallel in the system on the gas inlet side. The quartz tube was bypassed when setting the argon flow rate.
- After setting the argon flow rate, the flowmeter was bypassed, allowing argon gas to flow through the tube.
- After dwelling at 400 ˚C, heating was continued to 650 ˚C at a rate of 5 ˚C/min, dwelling for 30 min at the set temperature.
- The furnace element was switched off to start the cooling cycle.
- When the furnace reached a temperature below 300 ˚C, the argon cylinder valve was closed.

Step 3: Removing the samples

- The furnace was allowed to cool to below 70 ˚C before removing the glass fittings.
- The quartz tube was removed from the furnace.
- The samples and the substrates were removed from the tube.

Step 4: Cleaning the quartz tube and zirconia boats

- Most residue on the quartz tube was cleaned with acetone.
- The quartz tube was placed in the tube furnace with the zirconia substrates in the tube in the heating zone.
- The furnace was heated to 800 ˚C at a rate of 10 ˚C/min and held for 2 hours.
- The furnace element was switched off.
- The furnace was allowed to cool to below 70 ˚C before removing the quartz tube from the furnace and the substrates from the tube.

B.2 Sintering

Sintering was performed on the debound parts to densify them. The following apparatus was used in the sintering procedure:

A. Elite TSH 15/25/180 furnace with Eurotherm controller, coupled to
B. Vacuum system:
    a. (low vacuum: LV) Adixen Pascal 2012 SD rotary vane pump,
    b. (high vacuum: HV) Varian Turbo-V 81-M turbo pump, and
    c. Adixen ACS 2000 vacuum controller with ACC 2009 Pirani/Penning combination vacuum gauge.

C. UHP argon supply (Afrox High Purity, 99.998 %)

The step-by-step procedure that was used for sintering is given in ### below:

Table B.2: Step-by-step sintering procedure

Phase	System in use		Instructions	Dura-tion
Start-up & Argon Flushing			Open doors and windows to ensure air ventilation	10 min
	A	Furnace	Place sample inside furnace tube, making sure it is positioned in the middle of the heating zone. Tighten end seals.	
	A	Furnace	Plug in and switch on furnace, make sure the heat is switched off.	
	B	Vacuum (LV)	Plug in vacuum system and switch on vacuum controller/gauges. Do NOT switch vacuum pumps on yet.	
	C	Argon	Close argon inlet valve	
	B	Vacuum (LV)	Switch on rotary pump	
	C	Argon	Open argon **cylinder** valve (NOT the inlet valve).	
	C	Argon	Set argon line pressure to 50 kPa at the regulator (attached to cylinder), then slowly open argon inlet valve allowing argon gas to flow through the system.	
	C	Argon	The flow of argon will change the system pressure, so adjust the line pressure to 50 kPa at regulator.	
	C	Argon	Close argon inlet valve but leave the cylinder valve open.	
	B	Vacuum (HV)	Make sure turbo pump is switched off.	30 min
	B	Vacuum (LV)	Switch the rotary pump on and let it run until the vacuum gauge reads $<10^{-1}$Torr	
	C	Argon	Slowly open argon inlet valve, at the same time monitoring the system pressure on the vacuum gauge. Stop when the vacuum gauge reads $4.7x10^{+0}$ mbar.	30 min
	C	Argon	Make sure the argon pressure regulator reads <50kPa.	
	C	Argon	After half an hour close the argon inlet valve.	

Phase	System in use		Instructions	Dura-tion
Sintering Cycle	B	Vacuum (LV)	Wait while the rotary pump evacuates the argon from furnace and draws sufficient vacuum for turbo pump (<$5x10^{-2}$ mbar).	10 min
	B	Vacuum (HV)	Once the vacuum gauge reading is <$5x10^{-2}$ mbar, open valve to turbo, close valve to rotary pump (vacuum is now pulling through the turbo out of the rotary pump). Now switch on the turbo pump. The vacuum gauge controller automatically switches between the Pirani (LV) and Penning (HV) gauges around 10^{-4} mbar.	
	A	Furnace	Program the furnace heating cycle on the Eurotherm controller while waiting for full vacuum to be drawn	10 min
	A	Furnace (Ramp)	Set temperature to ramp at 10°C/min. Heat ramp from ambient temperature to 1200°C.	
	A	Furnace (Dwell)	Isothermal temperature hold for 2 hours	
	A	Furnace (Stop)	Set furnace to switch off at end of cycle.	
	B	Vacuum (HV)	Once the vacuum gauge reads <10^{-4} mbar, the heating cycle can be initiated.	
	A	Furnace	Switch on heat switch on furnace and press the run button to start sintering cycle.	3-4 hr
	A	Furnace	When furnace has reached 300°C during the cooling cycle (after sintering), the sinter cycle is complete, and the furnace heat can be switched off.	90 min
Backfill & System Shutdown	B	Vacuum (HV)	Switch off turbo pump **only**, wait till it stops rotating.	30 min
	C	Argon	Slowly open argon inlet valve to backfill system (argon line pressure must not exceed 50 kPa) with the rotary pump still working (vacuum gauge must not read more than $4.7x10^{+0}$ mbar).	30 min
	B	Vacuum (LV)	The turbo pump needs to cool down, so let the rotary pump run, pulling the argon through the turbo, for half an hour.	
	B	Vacuum (LV)	Switch off rotary pump and then switch off vacuum controller/gauge.	10 min
	C	Argon	Close argon inlet valve at furnace	
	C	Argon	Close argon valve on argon cylinder.	
	A	Furnace	Unplug electrical socket at the wall	
	B	Vacuum	Unplug electrical socket at the wall	
	A	Furnace	Remove sintered sample using heat resistant gloves and tongs. Leave furnace open to let in air	
			Close windows and doors	
			Estimate: Total time	7 hr

Appendix C : Test Data

C.1 Apparent Density

Table C.1: Hall Flowmeter Specifications

Cylinder weight [g]	269.05
Cylinder volume [cm3]	25

Table C.2: Weight of the Powder and Cylinder

Test	Total weight [g]
1	331.65
2	331.94
3	332.05

Table C.3: Apparent density of the CPTi Powder

Test	Apparent Density [g/cm3]
1	2.504
2	2.516
3	2.520
Average ($\bar{\chi}$)	2.513
Standard deviation (STD)	0.008

C.2 Archimedes Sintered Density

Table C.4: Archimedes sintered density of 55 vol% φ samples

Sample	Mass A, [g]	Mass B, [g]	Mass F, [g]	Sintered Density, [g/cm^3]	Average sintered density, [g/cm^3]
1	12,686	12,695	9,309	3,741	3,771
2	7,412	7,425	5,465	3,777	
3	8,242	8,251	6,089	3,807	
4	13,671	13,696	10,064	3,759	

C.3 Shrinkage

Table C.5: Dimensional change of 55 vol% φ sintered rectangular bar specimens

Specimen	L_{mould}	W_{mould}	$L_{sintered}$	$W_{sintered}$	DC_{length}	DC_{width}
1	88,7	17,6	79,36	16,03	-0,105	-0,089
2	88,7	17,6	79,88	16,07	-0,099	-0,087
3	88,7	17,6	80,04	16,11	-0,098	-0,085
4	88,7	17,6	79,04	16	-0,109	-0,091
5	88,7	17,6	79,04	15,84	-0,109	-0,100
Average [%]					-10,404	-9,034

Appendix D : CAD Drawings

D.1 Mould Design

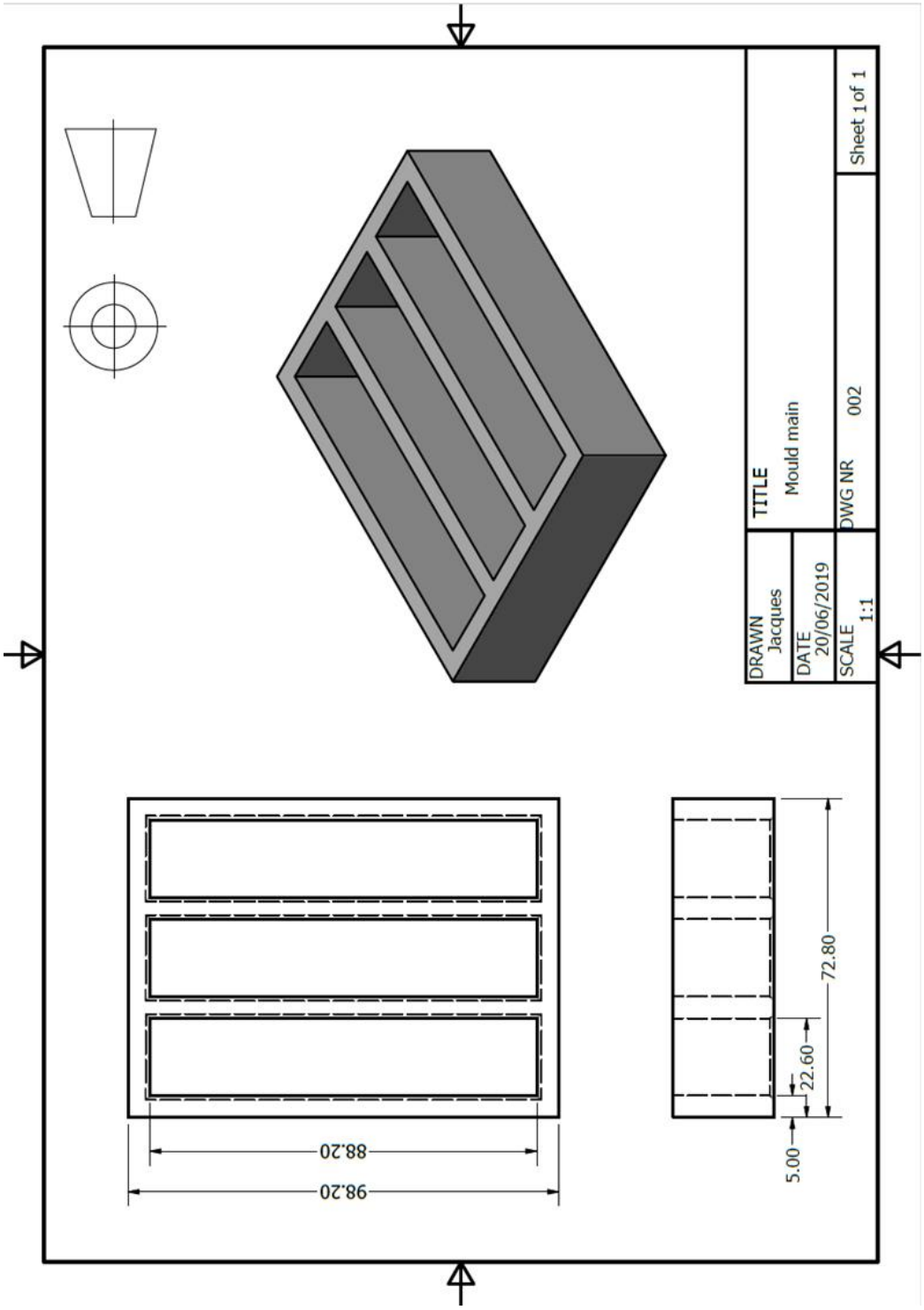

Figure D.1: CAD drawing of the bar cavity resin mould for 3D printing

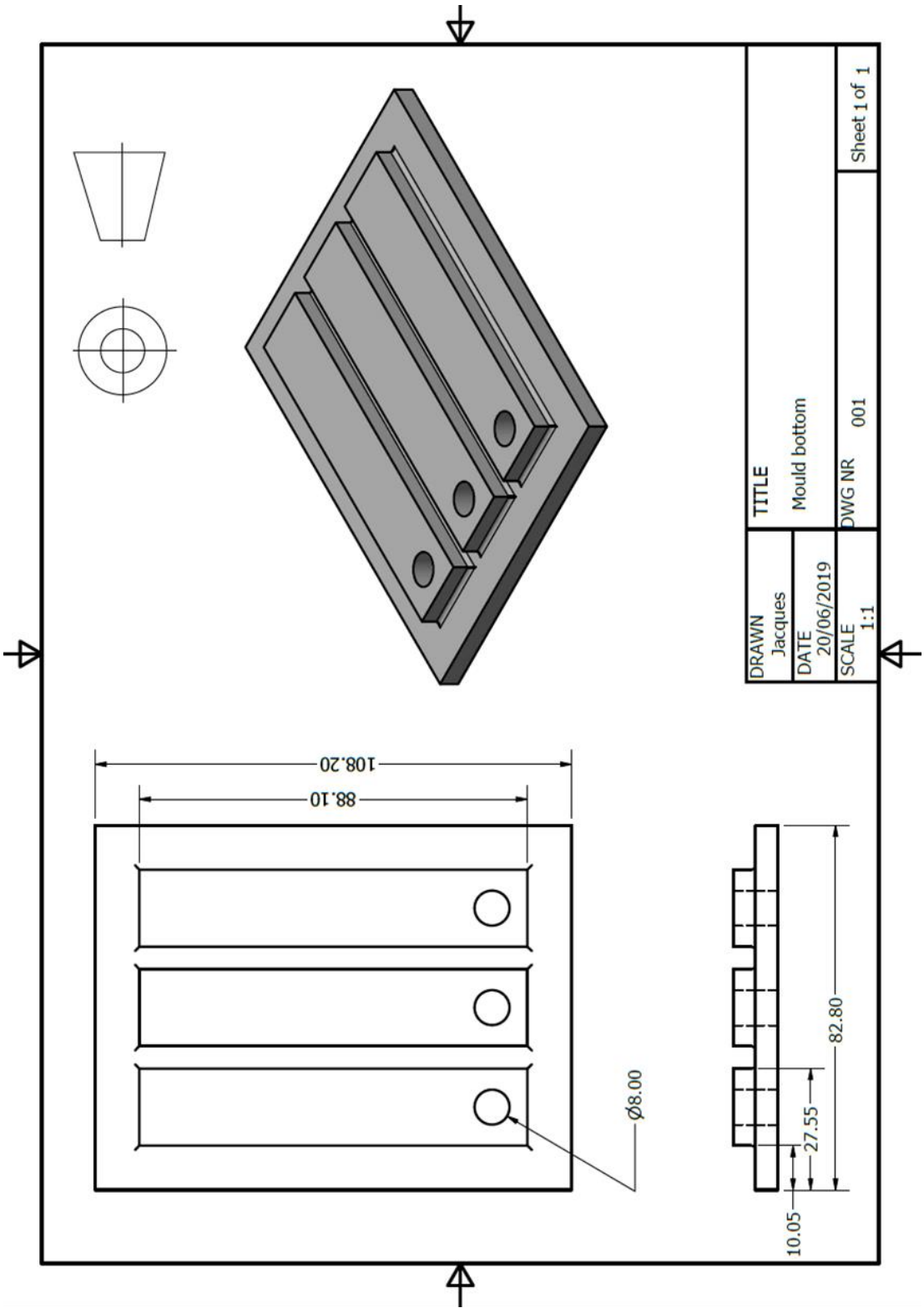

Figure D.2: CAD drawing of the bottom part of the resin mould for 3D printing

D.2 Tensile Test Specimen

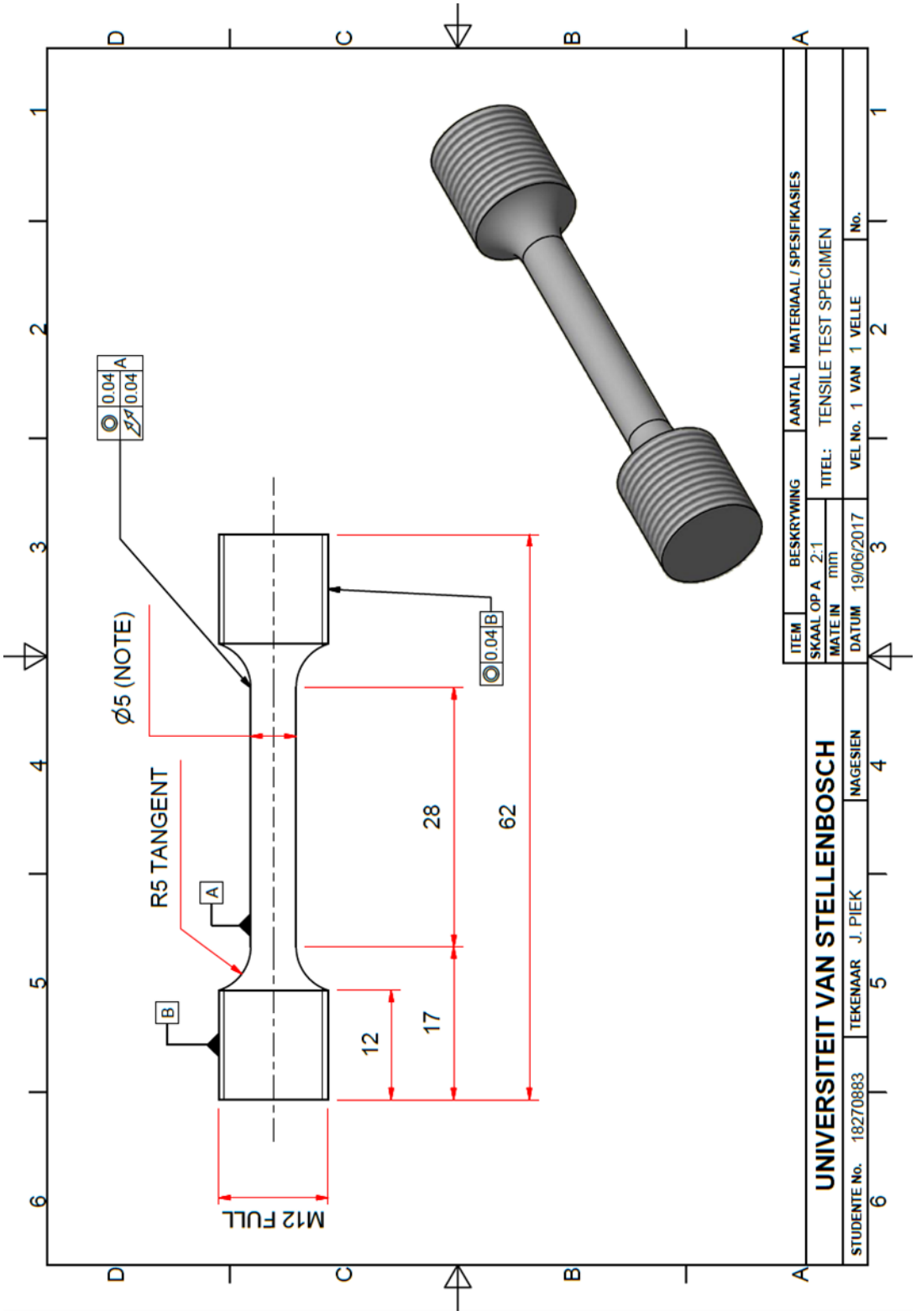

Figure D.3: CAD drawing of tensile test specimen